2016

Theory and experiments on flows containing surfactant-laden drops using experimentally determined surfactant transport parameters

Andrew Ryan White
Iowa State University

Theory and experiments on flows containing surfactant-laden drops using experimentally determined surfactant transport parameters

by

Andrew Ryan White

A dissertation submitted to the graduate faculty

in partial fulfillment of the requirements for the degree of

DOCTOR OF PHILOSOPHY

Major: Engineering Mechanics

Program of Study Committee:

Thomas Ward, Major Professor

Hui Hu

James Michael

Jonathan Regele

Richard Wlezien

Iowa State University

Ames, Iowa

2016

TABLE OF CONTENTS

LIST OF TABLES

LIST OF FIGURES

ABSTRACT

When two fluids come into contact an interface is formed between them. The surface tension of this interface plays an important role in determining the shape of the surface and can be lowered by the presence of surfactants. In dynamic interfacial fluid problems surface tension gradients due to surface convection of the surfactant can develop. These gradients result in Marangoni stress on the surface which affects surface velocities and thus bulk fluid velocities. These flows are relevant in enhanced oil recovery; dip and spin coating technologies; condensate formation on heat exchangers; emulsions in polymerization, biofuels, pharmaceuticals and food processing; and any number of microfluidics technologies, to name a few examples. The vast applications make the understanding of surface tension effects on interfacial flows important. A theoretical understanding exists for how surface tension gradients and Marangoni stress affect interfacial fluid flows, but direct comparisons between experiments and theory is less common in the literature. In this thesis two fluid dynamics problems involving drops are studied. In the first an aqueous drop containing surfactant is placed in a horizontal rotating cylindrical tank half-filled with oil. A film of oil forms between the drop and wall, and the addition of surfactant affects the film thickness, drop shape, and onset of drop breakup. The second problem involves an aqueous drop containing surfactant settling in oil under gravity where surface tension gradients affect the terminal velocity or drag of the drop. Using in-house surface tension measurements, surfactant adsorption and desorption models are developed. These models are then used in analytical and numerical analyses of the aforementioned fluid dynamics problems and compared to experiments. The results demonstrate the potential to use experimentally determined surfactant transport parameters to explain and in some cases predict experimental observations.

CHAPTER 1. INTRODUCTION

1.1 Motivation

Interfacial fluid dynamics problems are very common and important in a number of engineering applications. Here an interfacial fluid flow involves a flow where two typically immiscible fluids are in contact and form an interface between them. These flows can contain drops or bubbles moving in another bulk fluid, liquid films flowing or spreading on a substrate, and foams, to name some examples. Phenomena that occur at these interfaces can have a significant impact on the bulk flows and thus the engineering applications themselves. A particularly important characteristic of an interface between two fluids is its interfacial tension γ (or, synonymously, surface tension).

Surface tension is commonly expressed in dimensions of force per length and describes a resistance to change in curvature on a surface in the presence of another force such as gravity. Alternatively surface tension is sometimes expressed in dimensions of energy per area where it is considered the energy required to increase the local surface area of the surface. For example consider the two pendant drops suspended from a syringe needle in Fig. 1.1. Both drops are aqueous and are surrounded by canola vegetable oil. However in Fig. 1.1(a) the surface tension is an order of magnitude larger than in Fig. 1.1(b). The smaller surface tension in Fig. 1.1(b) allows the drop to noticeably deform (or increase its surface area) relative to a sphere due to gravity in comparison to the drop in Fig. 1.1(a).

Some example engineering applications involving interfacial flows where surface tension is important are: enhanced oil recovery methods where liquids or gases are used to displace

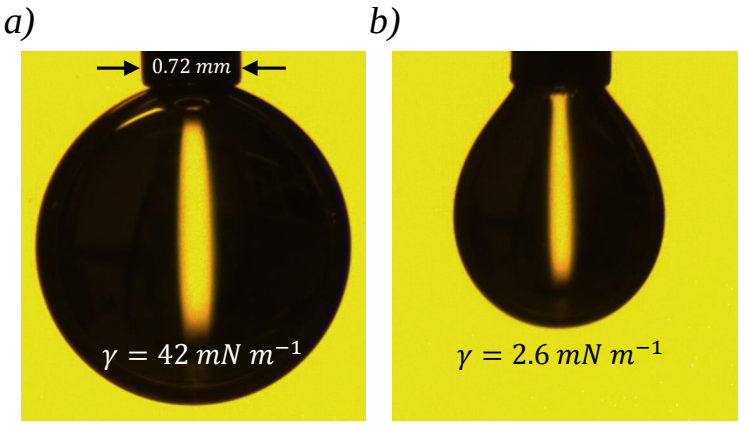

Figure 1.1 *Two aqueous pendant drops are shown suspended from a syringe needle and surrounded by canola oil. In (a) the drop contains 0.005 mM sodium oleate and has a volume of 6.2 μl. In (b) the drop contains 1.0 mM sodium oleate and has a volume of 2.1 μl. Their respective surface tension values are shown.*

crude oil in porous media (1); remediation of contaminated soil (2); coating flows such as dip and spin coating where the goal is to create thin uniform films (3); condensate forming on heat fins in air conditioners and other heat exchangers (4); emulsions in polymerization reactions (5), biofuels (6), pharmaceuticals (7) and food products (8); contact lenses where a thin tear film forms between the eye and the lens (4); microfluidic devices where small drops or bubbles can be formed and manipulated to serve any number or purposes (9). The ubiquity of interfacial fluid dynamics in industrial applications makes its study very relevant and important.

The surface tension of an interface can be lowered by the presence of surface-acting agents i.e. surfactants as demonstrated in Fig. 1.1. In many of the above engineering applications the presence of surfactants can facilitate interfacial phenomena such as drop deformation, break up and spreading (10; 11; 12; 13). Surfactants are often amphiphilic

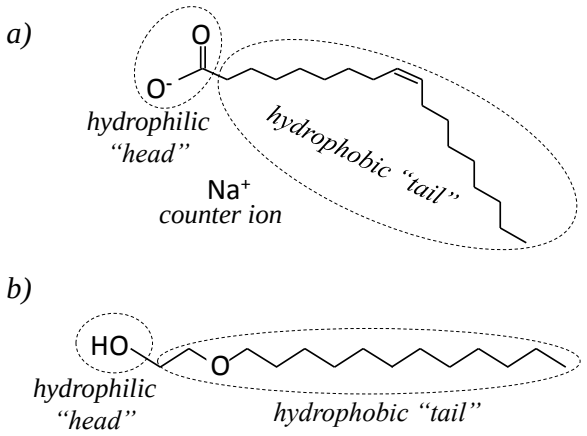

Figure 1.2 *Structural formulae for the surfactants a) sodium oleate and b) ethylene glycol monododecyl ether are shown. The hydrophilic and hydrophobic portions of each surfactant are labeled.*

molecules i.e. they contain both *hydrophobic* (water-fearing) and *hydrophilic* (water-loving) properties. They can be non-ionic molecules, or they can be anionic or cationic. These surfactants can exist as liquids or powders, and they can be chosen based on biocompatibility, environmental concerns and other factors. Figure 1.2 gives example structural formulae for the anionic sodium oleate and the non-ionic ethylene glycol monododecyl ether. Both of these surfactants have a long hydrocarbon chain or "tail" that is hydrophobic, and a "head" that is hydrophilic. The counter ions of ionic surfactants distribute in order to balance the net charge when dissociated in water. In the presence of an air-water or oil-water interface, the surfactant has the potential to *adsorb* to the surface. This is not to be confused with *absorption* which describes material entering the volume of another. If it does adsorb, it will be oriented such that its hydrophobic tail is primarily in the non-aqueous phase and the hydrophilic head mostly remains in the aqueous phase. The presence of the surfactant at the interface will generally lower the surface tension.

The surface tension over an interface containing surfactants does not need to be a constant value, and in fact it rarely is when considering dynamic flow problems. Because the fluid-

fluid surface is itself mobile, it is possible for surface convection to distribute any adsorbed surfactant non-uniformly, resulting in surface tension gradients. The presence of surface tension gradients can introduce a stress called the *Marangoni stress* (14) which can have a significant impact on these engineering applications. In order to effectively design engineering systems involving interfacial fluid dynamics, understanding the effects of surfactants and surface tension gradients is necessary.

The key to interfacial fluid dynamics problems is the interfacial stress equation. Consider two immiscible fluids denoted (1) and (2) with a density difference $\Delta\rho$. At the surface formed between the two fluids there is a jump in stress defined by (15)

$$\boldsymbol{n}\cdot\boldsymbol{\sigma}_1 - \boldsymbol{n}\cdot\boldsymbol{\sigma}_2 = -\boldsymbol{\nabla}_s\gamma + \gamma\boldsymbol{n}\left(\boldsymbol{\nabla}_s\cdot\boldsymbol{n}\right) \tag{1.1}$$

where $\boldsymbol{\sigma}_k = -p_k\boldsymbol{I} + \boldsymbol{\tau}_k$ is the stress tensor, γ is surface tension, and $\boldsymbol{\nabla}_s = (\boldsymbol{I} - \boldsymbol{nn})\cdot\boldsymbol{\nabla}$ is the surface gradient operator. Additionally $\boldsymbol{n}$ is the surface normal vector and $\boldsymbol{I}$ is the identity matrix. In the definition of the stress tensor $p_k = P_k - \rho_k g h$ is the modified pressure and $\boldsymbol{\tau}_k = \mu_k[\boldsymbol{\nabla}\boldsymbol{u}_k + (\boldsymbol{\nabla}\boldsymbol{u}_k)^T]$ is the viscous stress tensor caused by the fluid velocity $\boldsymbol{u}_k$. The left-hand side of eq. 1.1 is the jump in stress across the surface in the plane tangent to the surface. On the right-hand side the the second term is often called the capillary pressure due to surface tension and the curvature of the surface, and the first term defines the Marangoni stress.

In the pendant drop examples in Fig. 1.1, there is no fluid motion and thus the viscous stress tensor goes away on the left-hand side of eq. 1.1. Since surface tension gradients cannot develop without fluid motion only the capillary pressure remains on the right, and so eq. 1.1 reduces to the Young-Laplace equation $p_1 - p_2 = \gamma\boldsymbol{n}\left(\boldsymbol{\nabla}_s\cdot\boldsymbol{n}\right)$. This equation is the basis for the pendant drop method of measuring surface tension (16; 17) which will be used later in this thesis. When the fluids are not at rest, both the viscous stress component of $\boldsymbol{\sigma}$ and the Marangoni stress due to gradients in γ can become important. The Marangoni

stress acts tangentially in the direction of increasing surface tension, allowing it to impact the drag over the surface. This means, for a dynamic flow, gradients in surface tension can have significant impacts on surface velocities which will in turn impact the velocities in fluids (1) and (2). Understanding this term is key in predicting the fluid dynamics of interfacial flow problems involving surface tension gradients.

For a system with uniform temperature, the surface tension is typically only affected by the presence of surfactants. How the presence of surfactants affects surface tension is then described by an equation of state $\gamma = f(\Gamma)$ where Γ is the local amount of surfactant on the surface per area. In analyzing an interfacial flow it is convenient to consider gradients in Γ rather than gradients in γ. Then the Marangoni stress term in eq. 1.1 is rewritten like $\frac{d\gamma}{d\Gamma}\boldsymbol{\nabla}_s\Gamma$ where now the derivative of the equation of state is explicitly present. Thus the form of the equation of state is extremely important and provides the coupling between the fluid dynamics and the presence of surfactants.

Furthermore the manner in which surfactants get to the surface will dictate whether gradients in Γ over the surface will develop and to what extent. Surfactants residing in the bulk of either or both fluid (1) and/or (2) can adsorb as well as desorb to and from the surface over time. They can also travel along the surface by surface diffusion and/or surface convection. Additional complications in the mass transfer process include surfactant diffusion and convection in the bulk of either phase, as well as partial depletion of bulk surfactant concentrations if the amount of adsorbed surfactant on the surface is relatively significant. On top of choosing an appropriate equation of state $\gamma = f(\Gamma)$ for determining the form of the Marangoni stress term, appropriately modeling this mass transfer process is necessary when attempting to model interfacial flow problems.

While much theoretical work has been done with interfacial fluid dynamics problems involving films, drops and bubbles, direct comparisons between experimental and theoretical results when significant interfacial tension gradients develop are less common. Doing this requires determining surfactant adsorption and desorption rates which dictate how surfactant

accumulates on the surface. The overall goal of this thesis is to use experimentally determined surfactant transport parameters in theoretical analyses of a couple interfacial flow problems to explain certain phenomena and in some cases make qualitative comparisons. The hope is to advance the ability to use theoretical models as engineering tools by demonstrating their ability to describe real systems.

Before the the fluid dynamics problems can be handled, surface tension and surfactant transport models need to be developed. This begins in chapter 2 where methods for measuring surface tension with the pendant drop method and for predicting *equilibrium* surface tension values are presented. In chapter 3 this analysis is expanded to include situations where enough surfactant leaves the bulk volume for the drop surface that the bulk concentration becomes significantly lower at equilibrium. The parameters that govern equilibrium surface tension values are then used in chapter 4 where *transient* surface tension values are used to estimate surfactant adsorption and desorption rates. The analyses from chapters 2, 3 and 4 then result in surfactant sorption kinetics models that can be used in fluid dynamics problems.

In this thesis two flow problems involving drops will be studied. The first in chapter 5 will involve a single aqueous drop in a horizontal rotating cylinder half-filled with an oil. In this problem shear caused by the inner wall of the cylinder results in a thin film of oil residing between the drop and the cylinder wall. Depending on the surfactant and surfactant concentration present in the drop, surface tension gradients cause changes in the film thickness and drop shapes as well as induce tail streaming in the drops in some cases. Using the experimentally determined surfactant transport parameters the film thicknesses and drop shapes are predicted numerically with the thin film equations and compared with experiments with some agreement. The resulting surface velocity and surface surfactant concentration profiles from the numerical results are used to further explain phenomena observed in experiments.

In chapter 6 the second fluid dynamics problem is a buoyancy-driven surfactant-laden aqueous drop falling in a more viscous liquid. Like in the horizontal cylinder problem above, surface tension gradients develop on the drop surface when the drop contains surfactant. However the fluid velocities in some cases can be several orders of magnitude smaller than those in the horizontal cylinder problem, potentially making additional mass transport processes such as surface diffusion important. Again experimentally determined sorption kinetics are used in analytical and numerical analyses of the flow problem. Decent agreement is found between experimental and predicted drop terminal velocities using a single set of surfactant transport parameters for certain cases.

In the next section a literature review of relevant work on flows containing drops and thin films will be presented, showing both the great interest and volume of work on the topic over the past century as well as how work contained in this thesis fits into the body of knowledge.

1.2 Literature review

Nearly a century ago an important set of experiments were performed by W.N. Bond and D.A. Newton (18). The researchers observed the terminal velocities of air bubbles rising in water and syrup, water drops falling in castor oil, and mercury drops falling in syrup. If their experiments were ideal they would have observed drop and bubble velocities following the Hadamard-Rybczynski drag law, $F_{d,HR} = 2\pi\mu_o bU\left(\frac{2+3\xi}{1+\xi}\right)$, where U is the velocity, μ_o is the dynamic viscosity of the surrounding fluid, b is the drop or bubble radius, and $\xi = \mu_i/\mu_o$ is the ratio of the drop viscosity to the surrounding fluid viscosity (19; 20). This law describes the drag experienced by a fluid sphere translating in another fluid at low Reynolds number $Re^* = 2\rho_o bU/\mu_o$ where ρ_o is the density of the surrounding fluid. The superscript '*' denotes dimensionless quantities throughout this thesis. For large drops and bubbles Bond and Newton did see agreement between the Hadamard-Rybczynski drag law and experiments. However for small drops and bubbles their experiments followed the Stokes

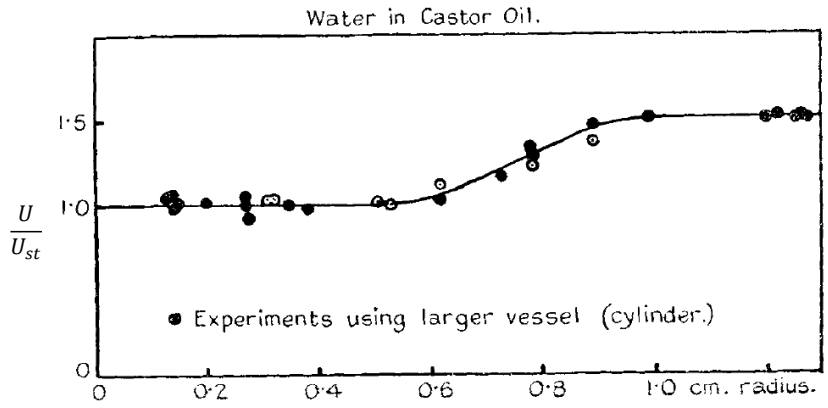

Figure 1.3 *An example figure from W.N. Bond and D.A. Newton (18). The vertical axis is the drop velocity normalized by the Stokes velocity U_{st} for a solid sphere with equivalent size and density, and the horizontal axis is the drop radius.*

drag law, $F_{d,St} = 6\pi\mu_o bU$ (21), as seen in Fig. 1.3 for example. This drag law describes how *solid* spheres translate in another fluid at low Re^*, and is identical to $F_{d,HR}$ when $\xi \to \infty$.

This behavior was consistent for each fluid-fluid system they studied, and for each data set there was a transition region where velocities fell between the Stokes and Hadamard-Rybczynski predictions. Using some dimensional analysis the authors suspected the transition coincided with critical values of what is now commonly called the Bond number, $Bo^* = \frac{\Delta\rho g b^2}{\gamma}$, (also sometimes called the Eötvös number Eo^*) where $\Delta\rho$ is the density difference between the sphere and the surrounding fluid and g is the gravitational acceleration. They speculated that the transition from fluid to solid sphere behavior may be due to contamination (surfactants) in their experiments, or the observation that surface tension measurements changed with time (an indication of the presence of surfactants). They also considered the transition may have to do with changes in viscosity.

Later in 1947 V.G. Levich provided some analysis for how surfactants and surface tension can impose a tangential stress on the surface (22). Levich explained that as a drop translates in another continuous fluid containing surfactants, those surfactants in the continuous phase will adsorb to the drop surface. Due to the drop's mobile surface, convection will then sweep some surfactant towards the trailing end of the drop, forming a greater concentration in the rear than the front. The result is a surface tension gradient, creating a tangential stress (Marangoni stress) which acts opposite the direction of the surface velocity. The surface velocity slows down, creating more drag and slowing the drop's terminal velocity. Levich simplified his analysis by assuming the surfactant concentration over the interface was nearly uniform so that surface convection could be neglected. In this limit he proposed several solutions depending on if the limiting mass transfer mechanism was diffusion of surfactant in the bulk, adsorption of surfactant from the bulk, or surface diffusion of surfactant.

Around the same time in 1942 L. Landau and B. Levich (not to be confused with V.G. Levich) considered another interfacial problem also effected by surface tension (23). They considered the film of liquid that remains on a plate as it is withdrawn from a bath of liquid. They found relationships between the film thickness, withdrawal speed, the density and viscosity of the liquid, and surface tension. More specifically they found a relationship between the film thickness and the capillary number $Ca^* = \mu_o U/\gamma$ where U here is the speed at which the plate is withdrawn. Later D.A. White and J.A. Tallmadge improved the solution of Landau and Levich by including gravity corrections (24). In an analogous problem, F.P. Bretherton considered the film of liquid that forms between a bubble moving in a tube and the tube wall in 1961 (25). This problem has significance to engineering applications such as microfluidic devices as shown in Fig. 1.4 from ref. (26). Bretherton found similar relationships for film thickness. In the current literature these two problems are commonly referred to as the Landau-Levich and Bretherton problems, respectively. While they are similar, their dissimilar domains lead to crucial differences in their flow. Specifically a single stagnation point develops on the surface in the Landau-Levich problem while two

Figure 1.4 *Experimental image of air bubbles driven by constant pressure through a microfluidic channel containing water with 0.015 wt% polyacrylamide and 0.10 wt% sodium lauryl sulfate (26).*

develop in the Bretherton problem (27). This has a significant impact on how surfactants can influence either problem.

Similar to how researchers found disagreements between experiments and theory early on in the buoyancy-driven drop and bubble problem, discrepancies between theory and experiments were found in the thin film problems. Specifically at low Ca^* experimental film thicknesses were found to be many times larger than predicted by the original theory of Landau and Levich and Bretherton (24; 25; 28). It would be shown later that this discrepancy is due to the presence of surfactants and, in the case of the Bretherton problem, the accumulation of surfactant at the rear of the bubbles and resulting surface tension gradients.

Since the middle of the 20^{th} century, the impact of surfactants on interfacial fluid dynamics problems like the buoyancy-driven drop or bubble, Landau-Levich and Bretherton problems introduced above have been investigated extensively. For the buoyancy-driven drop and bubbles problems, advancements in camera technologies allowed for new experiments that could visualize the internal circulation in drops. Many cite P. Savic in 1953 as being the first to experimentally observe what is known as a *stagnant cap* region in a drop surface

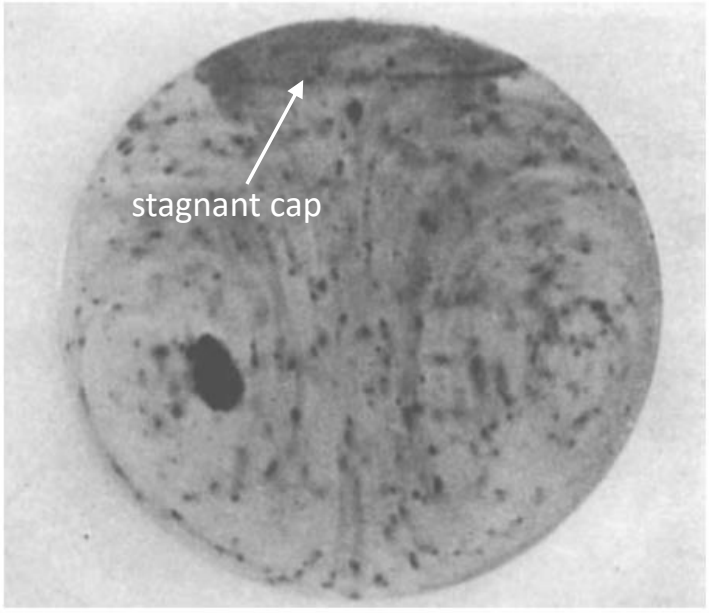

Figure 1.5 *Experimental image of a drop of carbon tetrachloride with a 6 mm diameter moving through a sugar solution (translating down in the image). The streamlines are visualized using dye. Note the accumulation of die at the rear where the stagnant cap resides.*

with surface contamination (29). In his analysis Savic considered surface convection to be the dominant mass transfer mechanism, leading to such an extreme build-up of surfactant at the rear that the resulting large surface tension gradients caused the surface velocity to approach zero there, hence the stagnant cap name. Additional experimental evidence for a stagnant cap was observed by R.H. Magarvey and J. Kalejs (30) (Fig. 1.5) as well as T.J. Horton *et al* (31) in the 1960s. Of particular note is the observation by Horton *et al* that very small amounts of surface contamination can cause the internal circulation to noticeably deviate from the Hadamard-Rybczynski circulation.

The stagnant cap theory was expanded in 1966 by R.F. Davis and A. Acrivos where they tried to predict the size of the stagnant cap region based on the difference in surface tension from the front to the rear of the drop (32). A similar analysis was preformed by He *et al* in 1991 but using a more accurate non-linear equation of state as opposed to the linear

relationship used by Davis and Acrivos (33). The choice of equation of state is extremely important as briefly mentioned earlier in the introduction. In 1983 J.A. Holbrook and M.D. LeVan performed an analysis that did not assume the existence of a stagnant cap nor a nearly uniform surface concentration of surfactant (34; 35). However they implemented a linear framework to describe relationships between surface tension, bulk surfactant concentration and surface surfactant concentration. In 1995 J. Chen and K.J. Stebe performed a similar analysis but with non-linear equations of state, non-linear adsorption models (36). Their result is one of the more complete analytical solutions in the current literature and it will be used with some modifications later in this thesis. They considered the coupling of the jump in shear stress across the drop surface to a surface mass balance which included surface convection (but no surface diffusion) and a non-linear adsorption-desorption source term. Additionally they allowed for non-ideal interactions between surfactant molecules.

The discrepancy in film thicknesses in the Bretherton problem was first analyzed in 1989 and 1990 by G.M. Ginley & C.J. Radke (37) and J. Ratulowski & H.-C. Chang (38) where Marangoni stress was introduced. However in the analysis of Ginley and Radke even *thinner* films were predicted. Indeed F. Wassmuth *et al* in 1993 used finite difference approximations of the thin film equations to show that it is possible to observe films that are smaller or larger than a case without surfactant (39). Similar findings have been found in numerical studies by S.N. Ghadiali & D.P. Gaver III (40) and H. Fujioka & J.B. Grotberg (41), lending more credibility to the possibility that both film thinning and film thickening relative to a no-surfactant case is possible. Unfortunately there have not been many experimental studies to compare to these analyses.

In the surfactant-laden drop and bubble problem A.H.P Skelland *et al* measured the velocities of chlorobenzene falling in water containing anionic, cationic and non-ionic surfactants in 1987 (42). They found some agreement with available empirical relationships when using the surface tension of corresponding static drops. Measuring the velocities of bubbles rising in aqueous surfactant solutions, K. Malysa *et al* made observations as to how much

surfactant was necessary to impact velocities (43). They estimated the surface coverage on the bubbles surface as it detached from a nozzle. Defining the surface coverage as $\theta = \Gamma/\Gamma_\infty$ where Γ_∞ is the maximum possible surface concentration for a monolayer, they found that only about $\theta > 0.1$ was necessary to maximize the effect of Marangoni stress.

There have been more recent experimental studies of surfactant-laden drops and bubbles, although there are not many due to the difficulty in analyzing the problem. N. Paul *et al* in 2015 tried to use settling drop velocities as a method for estimating the adsorption on drop surfaces (44). To do this they observed 1-octanol drops rising in aqueous solutions of sodium dodecyl sulphate (SDS) or Triton-X 100. Then using previously determined relationships between bulk surfactant concentration and surface coverage, they determined a relationship between surface coverage and terminal velocity. This analysis has several drawbacks, however. First the Langmuir isotherm was used to determine a relationship between bulk concentration and surface coverage when it has been shown that better models are available for SDS and Triton-X 100 (45; 46). Second they assume a uniform surface coverage is sufficient to characterize the distribution on a translating drop which may not acceptable. Third only one drop size was investigated which is clearly an important parameter in the surfactant-laden drop and bubble problem (18; 47).

In one of the more complete experimental analyses, R. Palaparthi *et al* observed air bubbles rising in glycerol-water mixtures containing hexaethylene glycol monododecyl ether ($C_{12}E_6$), a non-ionic surfactant (48). They used non-linear adsorption kinetics similar to Chen and Stebe (36). In the first half of their work they provide theoretical and numerical results for the stagnant cap problem with mixed diffusion and sorption kinetics. In the second half some agreement between experiments and numerical results using experimentally determined sorption kinetics was found. Unfortunately their viscous water-glycerol mixtures made diffusion the rate limiting step in the mass transfer process, making measurements of the sorption rate constants difficult. For a couple experimental cases, they compared the numerical results using several guesses for sorption rate constants and found a range of rates

that fit. As a result the authors concluded that settling bubble experiments could be used to estimate sorption kinetics.

While it is clear that much work has been done, direct comparisons between experiments and theory involving interfacial flows with significant surface tension gradients is less common in the literature. Comparing ideal theoretical models to real experimental results is a difficult task, and in the following chapters we will attempt to further the ability to make these comparisons.

CHAPTER 2. PATTERN SEARCH METHODS FOR PENDANT DROPS: ALGORITHMS FOR RAPID DETERMINATION OF SURFACE TENSION AND SURFACTANT TRANSPORT PARAMETERS

Modified from a paper published in *Colloids Surf. A*[1]

Andrew R. White[2], Thomas Ward[3]

Department of Aerospace Engineering, Iowa State University, Ames, IA 50011

2.1 Introduction

In this chapter we outline a process to apply pattern search methods to estimate equilibrium surface tension and surfactant transport parameters from pendant drops. The technique may be extended to other systems where robust minimization or search methods are required to estimate multiple unknown parameters. There are unique advantages with utilizing this technique to estimate properties of surfactant systems where minimization occurs between a known (experimental drop shapes or surface tension data) and unknown (Young-Laplace solution or isotherms) set of data, of which pendant drop analysis is an example. The main advantage stems from the fact that estimates for the unknown properties are produced by minimizing the common ℓ^2-norm between the known and unknown data sets which can be used to formulate an objective function used for minimization. To validate the technique

[1]A.R. White, T. Ward. *Colloids Surf. A* **485** (2015) pp. 1-10.

[2]Primary researcher and author

[3]Corresponding author. E-mail: thomasw@iastate.edu

for measuring surface tension we consider pendant drops of aqueous sodium oleate (SO) and aqueous sodium dodecyl sulfate (SDS) in mineral oil, along with several other classical data sets from the literature. This will be followed by implementation of the pattern search method to fit the equilibrium surface tension data to the Frumkin isotherm which requires the simultaneous minimization of 3 unknown parameters used to quantify surfactant transport.

The analysis begins with estimates of surface tension data. To generate surface tension data an axisymmetric drop shape analysis (ADSA) for pendant drops will be considered. This generally consists of fitting drop shapes prescribed by the Young-Laplace equation to experimentally measured drop shapes. There are two unknown parameters in the ADSA process: the surface tension and the curvature. Constructing the objective function is the most robust method for determining the best fit using ADSA. But it is also the most costly since the numerically generated solution to the Young-Laplace equation requires solving differential equations in multiple dimensions. Furthermore, the range of surface tension and curvature values must be bounded in order to determine the region where the minimum exists along with choosing an appropriate size for incrementing the independent variables.

Within the past few decades gradient-based solvers have been developed to perform the ADSA minimization process. The most common example of such a method is through implementation of the well known Newton-Raphson scheme (16). To perform the analysis the objective function is expanded in a Taylor series about the unknown parameters. Unfortunately gradient-based solvers too are computationally intensive, requiring the additional calculation of gradients to update the unknown in the iterative process. Additionally gradient-based solvers are not guaranteed to converge and tend to diverge if the initial guess is not sufficiently close to the best fit.

Instead we apply a pattern search method for determining best fits of the Young-Laplace equation. The pattern search method is an example of a direct search method which is more commonly used for performing modern error minimization. Direct search methods are

less computational expensive than gradient based methods because they typically do not require any additional mathematical manipulation of an objective function. Drawbacks in utilizing these methods exist because they are not necessarily robust in terms of convergence to a local minimum. An example of a direct method is the Nelder-Mead simplex method (49; 50), generally recognized as the first non-gradient based search method. With this method, minimization is achieved by reaching the local minimum in a region usually defined by some $p+1$ points where p is the number of unknowns, or dimensions. Points are updated by determining minima at points reflected through the line formed at the other p points. This method has been used in (51) where the MATLAB function *fminsearch* was used to perform the implementation with good results. Although the Nelder-Mead simplex method is capable of producing good results there are no guarantees that it converges to a local minimum.

On the other hand the pattern search method has been shown through robust mathematical analysis to consistently converge to a local minimum the details of which were described in (52; 53). A brief analysis of why the pattern search method converges is as follows: an objective function based on the ℓ^2-norm in multiple dimensions can possess a local minimum because the distance measured between the computational and experimental data d_i is squared. For example, in one dimension let the distance between a point generated numerically by the Young-Laplace equation and one measured experimentally be a function of only the surface tension and be denoted $d_i(\gamma_n)$. Now bound $d_i(\gamma_n)$ above and below by adding and subtracting some small-equidistant amount δ, respectively, from the unknown quantity γ_n. Then the error at step n is bounded by $\gamma_n \pm \delta$ i.e. $\sqrt{d_i(\gamma_n)^2} < \sqrt{d_i(\gamma_n \pm \delta)^2}$. This condition forms the basis for the pattern search algorithm. We will explore how to implement this method, and discuss situations where the condition may break down in regards to determining equilibrium surface tension and surfactant transport parameters, in the following sections.

2.2 Pattern search algorithm

2.2.1 *General pattern search algorithm*

We begin a discussion of the general pattern search algorithm that may be used to generate simultaneous estimates for multiple unknown parameters. The pattern search technique relies on the existence of a local minimum in an objective function for a set of unknown quantities. We will show that objective function estimates using an ℓ^2-norm are sufficient to satisfy this criteria for determining equilibrium surface tension and surfactant transport parameters under certain conditions. The ℓ^2-norm has been a standard for automated calculation of surface tension (16) and errors estimated using the ℓ^2-norm can be generalized to any type of curve fitting method. The ℓ^2-norm is simply defined by the Euclidean distance

$$\psi(c_{1,n}, c_{2,n}, \ldots, c_{p,n}) = \sqrt{\sum_{i=1}^{I} d_i(c_{1,n}, c_{2,n}, \ldots, c_{p,n})^2}, \tag{2.1}$$

where $\psi(c_{1,n}, c_{2,n}, \ldots, c_{p,n})$ is the objective function of p unknowns $c_{1,n}, c_{2,n}, \ldots, c_{p,n}$ which also serve to denote coordinates $(c_{1,n}, c_{2,n}, \ldots, c_{p,n})$. The variable d_i is used to denote the distance measured between I points of some numerically generated and experimentally generated data sets at specific positions i along an axis of the independent variable at minimization step n.

The general algorithm goes as follows: Starting with initial guesses for the coordinates $(c_{1,0}, c_{2,0}, \ldots, c_{p,0})$, we update these points to find a trajectory that leads to the local error minimum. For the pattern search algorithm this is achieved without the use of calculating gradients by determining the minimum in the set,

$$
\begin{aligned}
A = \quad & \{\psi(c_{1,n} + L_1\Delta c_{1,n}, c_{2,n} + L_1\Delta c_{2,n}, \ldots, c_{p,n} + L_1\Delta c_{p,n}), \\
& \psi(c_{1,n} + L_2\Delta c_{1,n}, c_{2,n} + L_1\Delta c_{2,n}, \ldots, c_{p,n} + L_1\Delta c_{p,n}), \\
& \ldots \\
& \psi(c_{1,n} + L_3\Delta c_{1,n}, c_{2,n} + L_3\Delta c_{2,n}, \ldots, c_{p,n} + L_3\Delta c_{p,n})\}
\end{aligned} \tag{2.2}
$$

where $[L_1, L_2, L_3] = [-1, 0, 1]$. There are 3^p elements in set A if one includes the initial coordinates at each minimization step $(c_{1,n}, c_{2,n}, \ldots, c_{p,n})$. Let $\beta_1, \beta_2, \ldots, \beta_p = 1, 2$ or 3 be used to denote the indices $L_{\beta_1}, L_{\beta_2}, \ldots, L_{\beta_p}$ corresponding to the objective function minimum at step n in set A located at coordinates $(c_{1,n} + L_{\beta_1}\Delta c_{1,n}, c_{2,n} + L_{\beta_2}\Delta c_{2,n}, \ldots, c_{p,n} + L_{\beta_p}\Delta c_{p,n})$. If the elements of the vector $\mathbf{M} = (M_1, M_2, \ldots, M_p) = (L_{\beta_1}, L_{\beta_2}, \ldots, L_{\beta_p})$ contain these values then new guesses at step $n+1$ for the unknowns can be written as

$$
\begin{bmatrix} c_{1,n+1} \\ c_{2,n+1} \\ \cdots \\ c_{p,n+1} \end{bmatrix} = \begin{bmatrix} c_{1,n} \\ c_{2,n} \\ \cdots \\ c_{p,n} \end{bmatrix} + \begin{bmatrix} M_1\Delta c_{1,n+1} \\ M_2\Delta c_{2,n+1} \\ \cdots \\ M_p\Delta c_{p,n+1} \end{bmatrix}. \tag{2.3}
$$

The step sizes $\Delta c_{1,n+1}, \Delta c_{2,n+1}, \ldots \Delta c_{p,n+1}$ remain constant until the minimum of set A produces the zero vector i.e. $\beta_1 = \beta_2 = \cdots = \beta_p = 2$ such that $\mathbf{M} = \mathbf{0}$. If this occurs then the step size is uniformly reduced by ϕ i.e. $\Delta c_{1,n+1}, \Delta c_{2,n+1}, \ldots \Delta c_{p,n+1} = \phi\Delta c_{1,n+1}, \phi\Delta c_{2,n+1}, \ldots \phi\Delta c_{p,n+1}$ with $0 < \phi < 1$ and the procedure continues. The iterative process is completed when one or several of the unknowns meet a user defined minimum error requirement between two consecutive steps $|c_{1,n+1} - c_{1,n}|$ or $|c_{2,n+1} - c_{2,n}|$ or ... or $|c_{p,n+1} - c_{p,n}| \ll 1$.

2.2.2 *Log scaling*

In situations where one or more of the p unknowns contains values that can span multiple orders of magnitude it is possible to use a log scale. For any unknowns to be treated in this manner its coordinates for ψ in A would be written as,

$$\begin{aligned} A = \quad & \{\psi(c_{1,n}10^{L_1\Delta c_{1,n}}, c_{2,n}10^{L_1\Delta c_{p,n}}, \ldots, , c_{p,n}10^{L_1\Delta c_{p,n}}), \\ & \psi(c_{1,n}10^{L_2\Delta c_{1,n}}, c_{2,n}10^{L_1\Delta c_{p,n}}, \ldots, , c_{p,n}10^{L_1\Delta c_{p,n}}), \\ & \ldots \\ & \psi(c_{1,n}10^{L_3\Delta c_{1,n}}, c_{2,n}10^{L_3\Delta c_{p,n}}, \ldots, c_{p,n}10^{L_3\Delta c_{p,n}})\}. \end{aligned}$$

A base of 10 is used for this example but any value can be used with the algorithm. The rest of the algorithm is the same with the exception being the new guesses are written:

$$\begin{bmatrix} c_{1,n+1} \\ c_{2,n+1} \\ \ldots \\ c_{p,n+1} \end{bmatrix} = \begin{bmatrix} c_{1,n}10^{M_1\Delta c_{1,n+1}} \\ c_{2,n}10^{M_2\Delta c_{2,n+1}} \\ \ldots \\ c_{p,n}10^{M_p\Delta c_{p,n+1}} \end{bmatrix}.$$

The iterative process is complete when the error is minimized based on user defined values.

2.2.3 *Implementation*

Implementation requires determining the set of values at each set of coordinates that are included in A. Any looping algorithm will produce the desired set of values. What is important is how the coordinates are addressed. For this step in the algorithm it is convenient to think of the coordinates as forming a *stencil* with a central point being the initial coordinate for the current minimization step $(c_{1,n}, c_{2,n}, \ldots, c_{p,n})$. Using the central point as the initial point in coordinate addressing is not recommended since it will be inefficient when

programming. Instead the $(c_{1,n} + L_1\Delta c_{1,n}, c_{2,n} + L_1\Delta c_{2,n}, \ldots, c_{p,n} + L_1\Delta c_{p,n})$ $(L_1 = -1)$ coordinate should be addressed as the $1st$ point. Then the central point will be the $5th$ point if numbering from left to right followed by top to bottom in two dimensions (two unknowns) for example.

Central to building an efficient algorithm is developing a process for determining the vector $\mathbf{M}$. In practice the vector $\mathbf{M}$ does not need to be determined explicitly. Instead the new points may be updated using the addressing described above. Then by pre-assigning L_1, L_2 and L_3 values to the addresses in the stencil it is possible to build a fast algorithm without the need to explicitly determine the vector $\mathbf{M}$. Referring back to the two dimensional example if the address one is the minimum for the current step then this would correspond to $L_{\beta_1} = L_{\beta_2} = -1$ or the upper left corner of the stencil.

The details above provide a formal mathematical statement for implementing the pattern search algorithm. In practice the implementation is rather straightforward and intuitive as we discuss in the following sections using pendant drop analysis and estimates for surfactant transport parameters as examples.

2.3 Pendant drops

2.3.1 *Image analysis and fitting procedure*

The first step in ADSA is accurately defining the experimental drop surface. This step alone has warranted a detailed analysis from other researchers (54). For this manuscript we use a pixel threshold analysis (55) to define pixels occupied by the continuous or drop phases. Then, beginning with the top left edge of the drop where it meets the needle, the drop surface is traced using the following algorithm. Consider the schematic of the drop surface shown in Fig. 2.1(a) following the application of the pixel threshold where dark squares are pixels occupied by the drop, gray squares are occupied by the continuous phase and squares outlined in white represent the drop surface. The pixel 'X' is known to be on the surface. Its

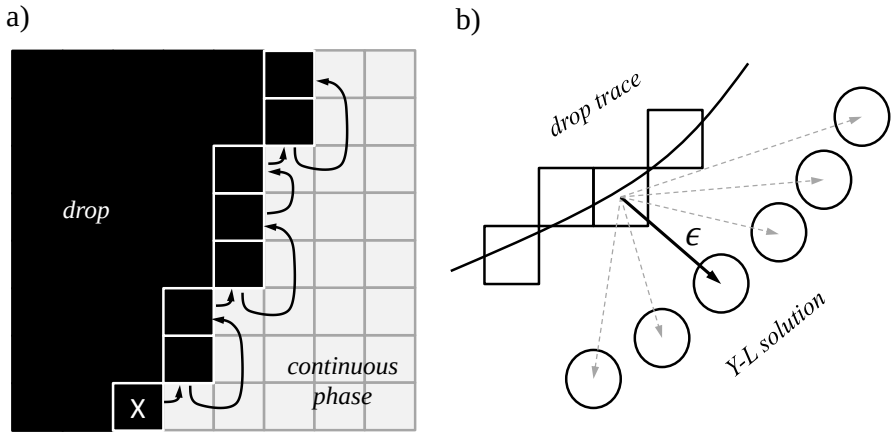

Figure 2.1 *in (a) a visual representation of the tracing algorithm is shown. In this schematic the algorithm begins at 'X' and continues in the path indicated by the arrows. In (b) a visual representation of the method used to determine ϵ and subsequently $\psi(b, \gamma)$ is shown where squares represent coordinates of $I = (x_i, z_i)$ and circles represent coordinates of $YL = (x_j, z_j)$.*

eight neighboring pixels are considered in counterclockwise order beginning with the pixel to the right. Once a dark (drop-containing) pixel is found that pixel is saved as another point on the surface. Next at the newly discovered surface point, its eight neighboring pixels are now checked in counterclockwise order. A crucial rule in this algorithm is the first pixel that is checked of the eight neighboring pixels is the last non-surface pixel checked from the previous set of eight. The arrows in Fig. 2.1 show which pixels are checked and in what order as the surface is defined. This algorithm continues until the right edge of the needle tip is reached.

The tracing step results in a set of interface coordinates, denoted $I = (x_i, z_i)$. Next the experimental drop shape is compared to a drop shape prescribed by the Young-Laplace equation, $\gamma_n \kappa = \Delta\rho g z - \frac{2\gamma}{b_n}$, where κ is the surface curvature, γ_n is the unknown surface tension

and b_n is the unknown radius at the drop apex. Rearranging and non-dimensionalizing the Young-Laplace equation using the unknown b_n as the length scale yields $\kappa^* = Bo^* z^* - 2$ where $Bo^* = \Delta\rho g b_n^2/\gamma_n$ is the Bond number. The superscript '*' indicates dimensionless quantities. In order to determine a drop's shape from this equation it is parameterized with respect to arc length s, yielding

$$\frac{d\theta}{ds^*} = 2 - Bo^* z^* - \frac{\sin\theta}{x^*} \tag{2.4}$$

$$\frac{dx^*}{ds^*} = \cos\theta \tag{2.5}$$

$$\frac{dz^*}{ds^*} = \sin\theta \tag{2.6}$$

where θ is the angle between the surface tangent and the axis of symmetry. For a derivation of this set of differential equations readers should refer to (16; 17; 56). An adaptive $4th$-order explicit Runge-Kutta-Merson scheme is used to numerically integrate these equations for a given Bo^* with appropriate initial conditions. The solution is initialized at $\theta \to 0$ where $z^{'} \to 0$ (primes indicate derivatives with respect to s) and the Young-Laplace equation can be approximated by the ordinary differential equation $z^{''} + z^{'}/x + Bo^* z^* - 2 = 0$. This has the analytical solution

$$z^* = \frac{2}{Bo^*}\left[1 - J_0\left(x^*\sqrt{Bo^*}\right)\right] \tag{2.7}$$

where J_0 is the zeroth order Bessel function of the first kind (17; 45). The drop shape given by eqs. 2.4-2.6 is denoted $YL = (x_j, z_j)$.

Solutions of the Young-Laplace equation presented above are symmetric about the apex, so I is split into two halves about the vertical axis of symmetry. The horizontal location of the axis of symmetry x_s is measured to be the average of the leftmost and rightmost horizontal

coordinates of I. The resulting left and right halves are $I_L = (x_\ell, z_\ell)$ and $I_R = (x_r, z_r)$ which contain L and R coordinate points, respectively. The maximum horizontal distance between the axis of symmetry and the drop surface is denoted b_x and is the initial guess for the radius of curvature at the drop apex, b_0.

For every point on the interface the minimum Euclidian distance between the experimental and Young-Laplace drop shapes is needed. This is defined by the minimum of $d_i = \sqrt{(x_i - x_j)^2 + (z_i - z_j)^2}$ where (x_j, z_j) are coordinates of YL and (x_i, z_i) are coordinates of I_R or I_L. This distance is denoted ϵ and is shown schematically in Fig. 2.1(b). The sum of all ϵ normalized by L or R for I_L or I_R, respectively, gives the objective functions $\psi_L(b_n, \gamma_n)$ or $\psi_R(b_n, \gamma_n)$ for a particular guess of γ_n and b_n. There are $p = 2$ unknown parameters, $(c_{1,n}, c_{2,n}) = (b_n, \gamma_n)$, for the pattern search method applied to pendant drops. Therefore, the set A from eq. 2.2 will contain 3^p points producing a nine-point stencil of values.

As stated above the initial guess for b_n is b_x. To determine an initial γ_n an initial guess of $Bo^* \approx 0.2$ is made such that $\gamma_0 = 5\Delta\rho g b_x^2$. Depending on the surfactant system, γ_n can take values from approximately $O(10)$ to $O(0.0001)$ mN m^{-1}. For this reason a log scale is used for the stencil in the γ-direction in the form $\gamma_n 10^{L\Delta\gamma^*}$ with $\Delta\gamma_n^* = 0.05$ initially and $L = [-1, 0, 1]$. For the b_n-direction the stencil is scaled linearly like $b_n + L\Delta b_n$ with Δb_n being 10 μm initially, and ϕ is fixed to $\phi = 0.1$. The pattern search algorithm continues until $(\gamma_n 10^{\Delta\gamma_n^*} - \gamma_n)/\gamma_n < 10^{-4}$ and $\Delta b_n/b_n < 10^{-4}$. To prevent settling on a false minimum, the algorithm is restarted using the previously converged b_n and γ_n as the initial guess. If the b_n and γ_n from successive runs of the pattern search algorithm are sufficiently close then those b_n and γ_n are taken as the solution.

This process is carried out to fit YL to both I_L and I_R, giving two estimates for surface tension, γ_L and γ_R, for the drop. The average of the values for the two halves then gives γ for the drop at that instant in time. Typically pendant drop algorithms include the tilt of the drop α due to a potentially unlevel camera as an unknown, but this has been neglected

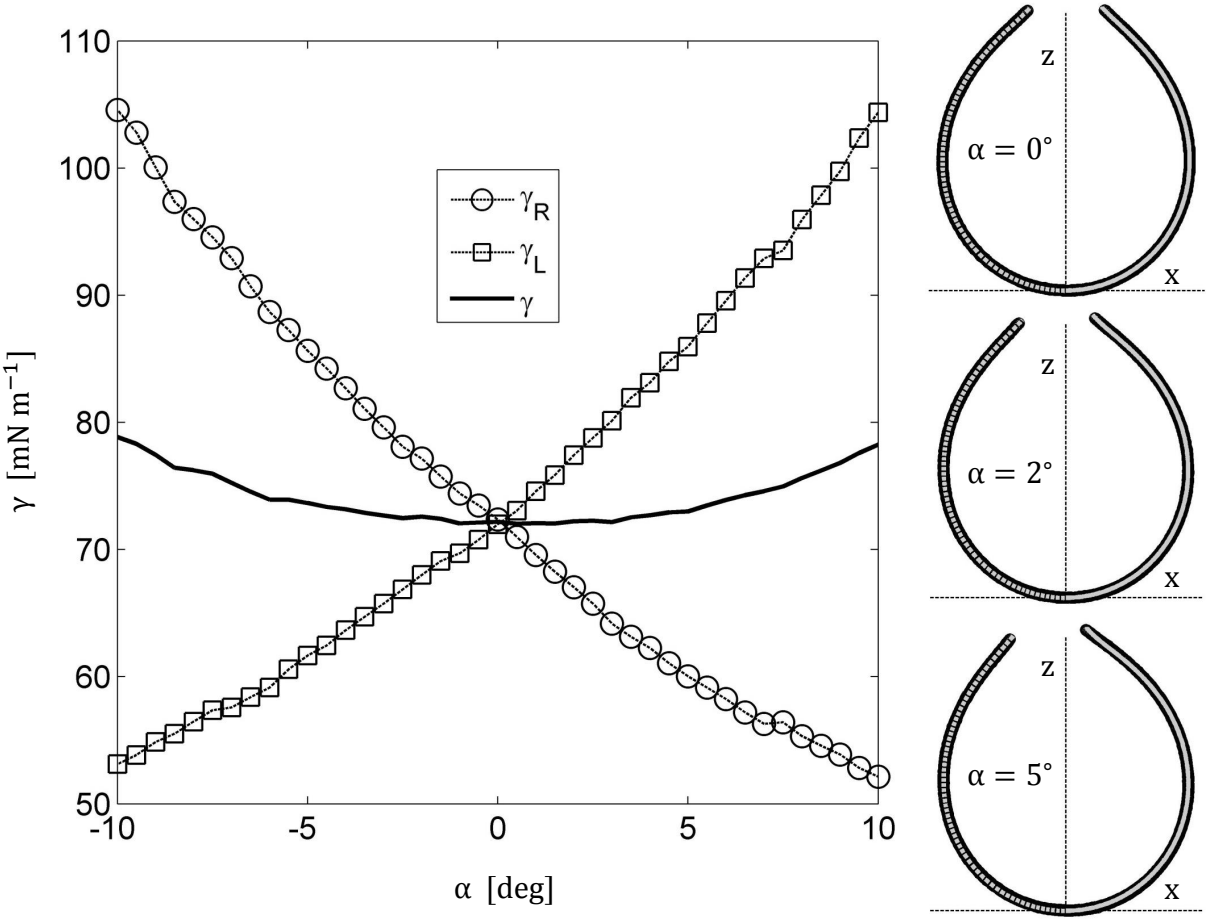

Figure 2.2 *the effect of drop tilt on γ is shown for the experimental trace I of a 7.75 μl drop of water suspended in air. The trace is rotated $\pm$ 10°. Three examples of I (black) with the best fits YL_R (solid gray) and YL_L (dotted gray) are shown for 0°, 2° and 5°.*

here. Consider Fig. 2.2 where the experimental trace I of the pendant drop in Fig. 2.4(a) has been rotated $\alpha = \pm 10°$. Values for γ_R and γ_L deviate significantly as $|\alpha| > 0°$, but the mean γ over $-2° \leq \alpha \leq 2°$ is 72.13 mN m^{-1} with a standard deviation of 0.09 mN m^{-1} or 0.12% of the mean. Over $-1° \leq \alpha \leq 1°$ the mean γ becomes 72.12 mN m^{-1} with a standard deviation of 0.06 mN m^{-1} or 0.08% of the mean. Beyond $|\alpha| > 2°$ errors in γ become significant. However tilts between 1 and 2° and larger are noticeable with the naked eye as demonstrated in the example fits on the right side of Fig. 2.2. Tilts this large were therefore corrected prior to image capture, leaving α small enough that any potential errors due to neglecting image tilt would be around 0.1% or less. Finally, in the case of fitting successive images the initial guesses b_0 and γ_0 for the next image are taken as the solution of the previously fit image.

2.3.2 *Experiments*

An in-house setup was created to image pendant drops and bubbles for analysis similar to many common tensiometers. A vertically oriented syringe pump (New Era Pump Systems) drove the plunger of a 100 μl Hamilton Gastight syringe. The syringe needle was a 22 gauge stainless steel type 3 needle (Hamilton) for pendant drops and either a 22 or 16 gauge hooked "J-needle" (Ramé-Hart) for pendant bubbles. A clear 25×25×50 mm acrylic box was used to contain the continuous phase. A CCD camera (PixeLINK) captured images of the drop or bubble with a resolution of 1200×1600 pixels. The aspect ratio of the images was calibrated by orienting a standard 22 gauge syringe needle both vertically and horizontally, checking for differences in observed needle thickness of which none was found. A 15 W vertical fluorescent lamp was situated on the side of the drop or bubble opposite the camera. This provided excellent contrast between the drop or bubble phase and the continuous phase.

The surfactants used in pendant drop experiments were either > 99% sodium dodecyl sulfate (SDS) (Fisher Scientific) or > 97% sodium oleate (SO) (TCI). Both surfactants were used as received. SDS concentrations ranged between 0.1 to 5.0 mM and SO concentrations

ranged between 0.04 to 2.0 mM. The continuous phases were either air, light mineral oil (Fisher Scientific, $\rho_d = 830$ kg m^{-3}) or reverse osmosis water at 23 °C. Drop volumes ranged from 1 to 30 μl so that the drops were both not too spherical and remained attached to the needle. Pendant drops were formed at a rate of 80 μl min^{-1}. Experiments with surfactant typically lasted between 5 and 30 minutes. Images were taken of the drops over time at intervals of 2 to 30 s per frame and were processed in MATLAB as described in the previous section.

2.3.3 *Results: pendant drops*

Figure 2.3 shows example contour plots of $\psi_R(b, \gamma)$ and the subsequent path generated by minimizing the objective function using the pattern search algorithm for the drop's right halves (I_R). Four pendant drop/bubble systems are considered: two drops of water with different volumes suspended in air, an air bubble in water, and a water drop with 5.6 mM SO suspended in corn oil (Crisco) for 10 minutes. The contour plots of the objective functions were generated by solving eqs. 2.4-2.6 for the range of b and γ shown. In each subplot the $'*'$ indicates the initial guess using $\gamma_0 = 5\Delta\rho g b_x^2$ with the black circles being the successive guesses by the pattern search algorithm. The $'X'$ indicates another run of the algorithm with an initial guess of 10 mN m^{-1} and the black triangles are its successive guesses. The red $'+'$ indicates the best fit. With the exception of Fig. 2.3(d) the axes of each figure are scaled identically. In the top left of each plot in Fig. 2.3 the best fit surface tension is shown along with the number of points R in I_R. The computation time taken by the pattern search algorithm with the initial guess of $\gamma_0 = 5\Delta\rho g b_x^2$ using a computer with a 3.60 GHz Intel CPU is also shown.

Figure 2.4 shows raw experimental images with best fits of eqs. 2.4-2.6 in white corresponding to the contour plots in Fig. 2.3. The volume and Bo^* for each drop is shown. The values for γ_R and γ_L for the drop in Fig. 2.3(a) are 72.39 and 72.01 mN m^{-1}, respectively, resulting in $\gamma = 72.20$ mN m^{-1} which agrees well with values in the literature (57).

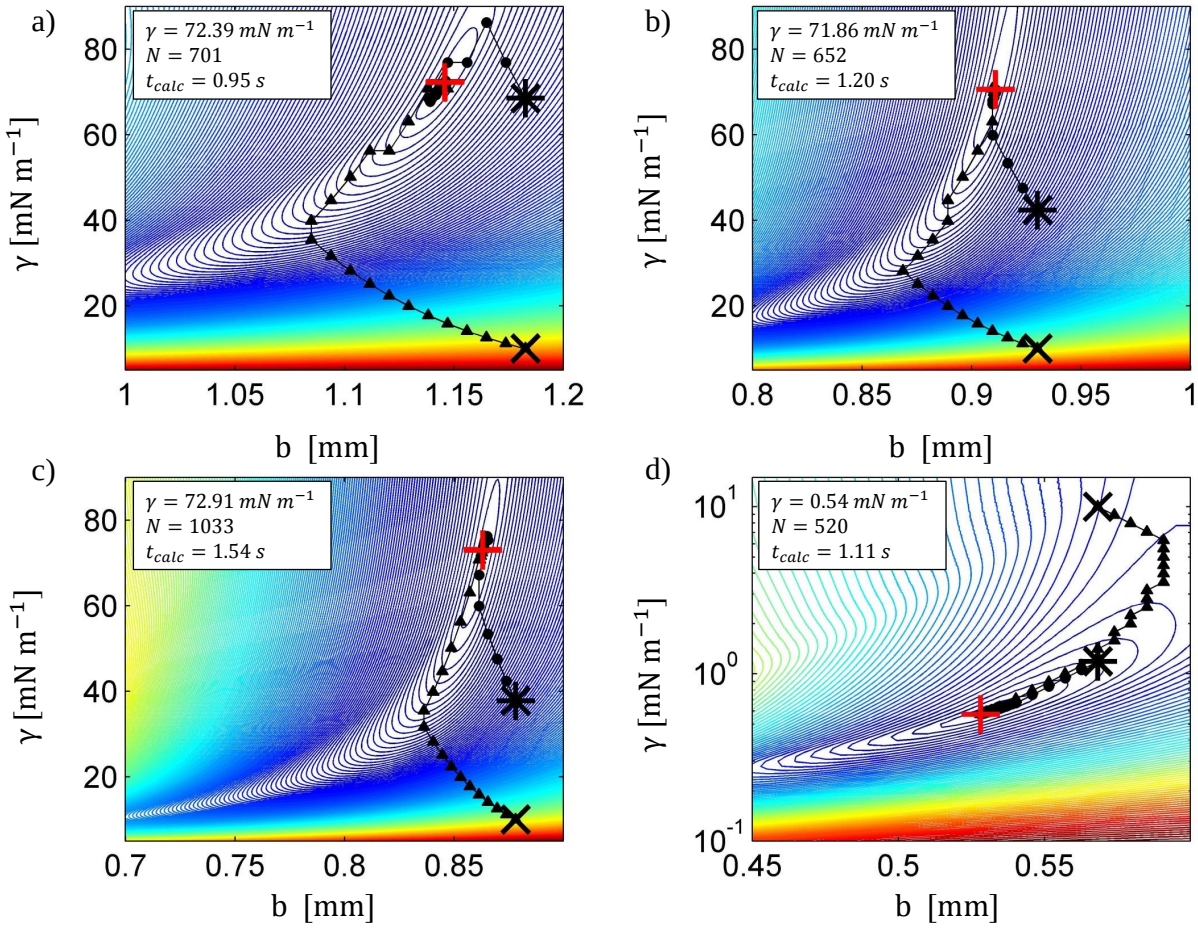

Figure 2.3 *example contour plots of $\psi(b, \gamma)$ are shown for (a) a 7.75 μl water drop in air, (b) a 3.5 μl water drop in air, (c) a 3 μl air bubble in water, and (d) a 0.9 μl 5.6 mM SO drop in corn oil after 10 minutes. The '*' indicates the initial guess using $\gamma = 5\Delta\rho g b_x^2$ and the 'X' indicates another run of the algorithm starting at γ =10 mN m^{-1}. The red '+' indicates the best fit while the black circles and triangles indicate successive guesses made by the pattern search algorithm. The resulting surface tension values are annotated in the top left of each plot.*

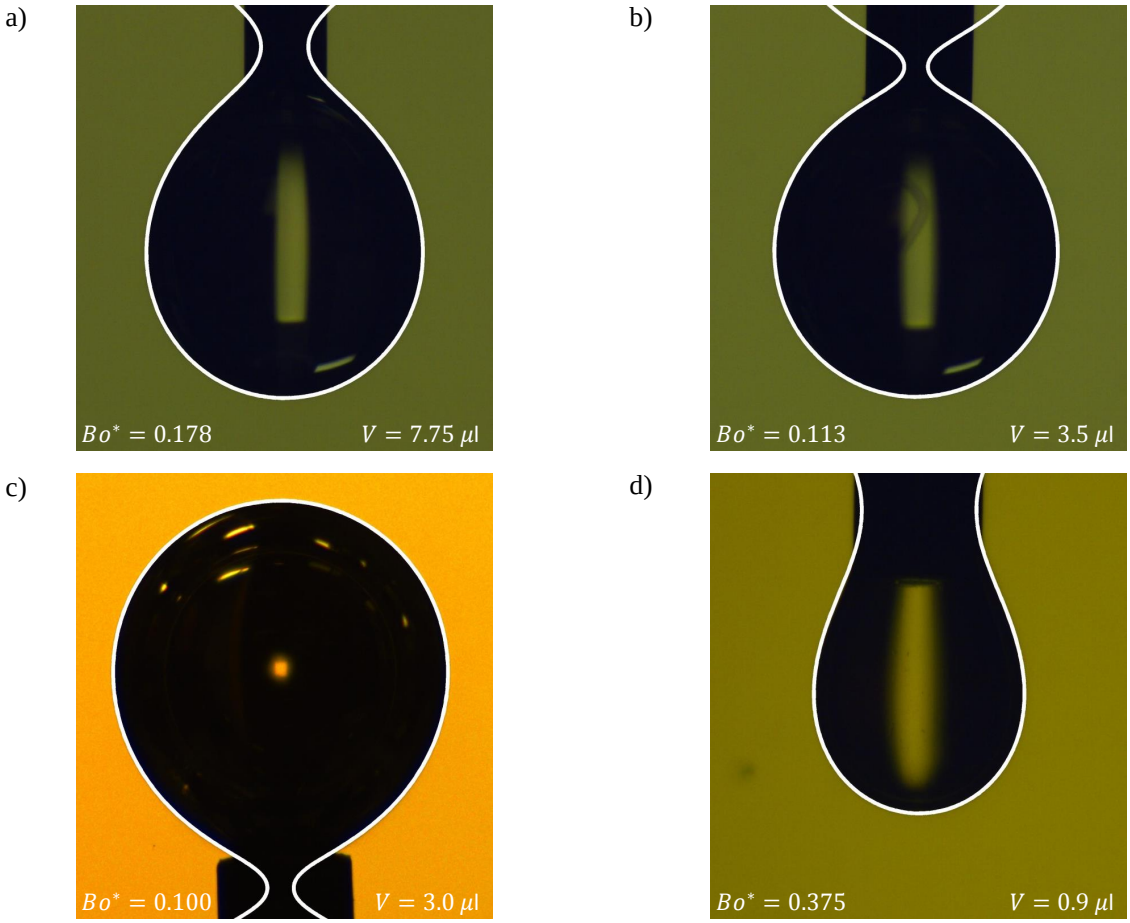

Figure 2.4 *pendant drops or bubbles corresponding to the contour plots of $\psi(b, \gamma)$ in Fig. 2.3 are shown for (a) a 7.75 μl water drop in air, (b) a 3.5 μl water drop in air, (c) a 3 μl air bubble in water, and (d) a 0.9 μl 5.6 mM SO drop in corn oil after 10 minutes. The white line is the best fit of eqs. 2.4-2.6. The Bond numbers are annotated for each drop or bubble.*

2.4 Surfactant transport parameters

2.4.1 *Isotherm and equation of state analysis*

After determining equilibrium values for the surface tension γ_{eq} it is common to further manipulate that data to estimate surfactant transport parameters for the surfactant-fluid systems (58; 59). Expressions governing surfactant sorption along and interface are typically written in terms of the local surface coverage of surfactant Γ_{eq} (mol m^{-2}) as a function of the subsurface concentration C_s (mol m^{-3}). Units for each of the quantities discussed in this section are provided to help avoid confusion with other studies that utilize similar notation. The Frumkin isotherm is one of the most commonly used expressions for measuring or estimating surfactant transport parameters (60). It relates transport properties such as the bulk surfactant distribution K_{eq} (m^3 mol^{-1}), maximum surface coverage Γ_∞ (mol m^{-2}) at or above the critical micellar concentration C_∞, and a molecular interaction parameter, Λ:

$$\frac{\Gamma_{eq}}{\Gamma_\infty} = \frac{K_{eq}C_s}{e^{-\Lambda\Gamma_{eq}/\Gamma_\infty} + K_{eq}C_s}. \tag{2.8}$$

We note that use of the Gibbs adsorption equation, $d\gamma_{eq} = -RT\Gamma_{eq}d\ln C$, with the Frumkin isotherm yield the familiar equation of state,

$$\gamma_{eq} = \gamma_0 + mRT\Gamma_\infty \left[\ln\left(1 - \frac{\Gamma_{eq}}{\Gamma_\infty}\right) + \frac{1}{2}\Lambda\left(\frac{\Gamma_{eq}}{\Gamma_\infty}\right)^2\right]. \tag{2.9}$$

Here γ_0 is the surface tension for $\Gamma_{eq} = 0$, R (J mol^{-1} K^{-1}) is the universal gas constant and T (K) the temperature. The constant m changes value depending on the surfactant where non-ionic surfactants have a value of $m = 1$ while 1:1 ionic surfactants require a value of $m = 2$ to account for the species generated by dissociation (61; 62; 63; 64). Using these two equations it is possible to predict how γ_{eq} varies with C_s for given K_{eq}, Γ_∞ and Λ. Thus K,

Γ_∞ and Λ can be chosen such that the norm between the resulting γ_{eq} versus C curve and the curve generated from experiments is minimized using a pattern search algorithm.

For $\Lambda = 0$ the system reduces to the Langmuir isotherm where convergence is guaranteed. The Frumkin isotherm with $\Lambda \neq 0$ can present several challenges for convergence when using the pattern search algorithm. First, consider that the isotherm and equation of state are difficult to manipulate because the system of equations actually has four unknowns, Γ_{eq}, Γ_∞, K_{eq} and Λ, with only two equations used to determine them. Here we have generalized the system of equations by considering Γ_{eq} as an unknown since its value depends on Γ_∞ and Λ according to the equation of state. Furthermore, the value of Λ is bounded above by 4 as discussed in (65). Values $\Lambda > 4$ yield isotherms in the $\Gamma_{eq} - C_s$ plane that possess multiple Γ_{eq} values at a given concentration.

Convergence is also directly influenced by the molecular interaction parameter for $\Lambda \leq 4$. To introduce a convergence criteria for the pattern search method we determine a mathematical relationship between the maximum surface coverage Γ_∞ and Λ using the Frumkin isotherm. The criteria is developed by expanding the exponential term in the denominator of eq. 2.8 for small $\Lambda\Gamma_{eq}/\Gamma_\infty$ yielding the linearized Frumkin isotherm equation $\Gamma_{eq}/\Gamma_\infty = K_{eq}C_s/[1-\Lambda\Gamma_{eq}/\Gamma_\infty + K_{eq}C_s]$ where we have dropped the $\mathrm{O}(\Lambda\Gamma_{eq}/\Gamma_\infty)^2 \ldots$ terms from the expansion. The maximum surface coverage occurs at or above the critical micellar concentration so we set $C_s = C_\infty$ in the resulting expression. Collecting terms involving Γ_∞ we derive the quadratic equation:

$$\frac{\Gamma_\infty}{\Gamma_{eq}} = \frac{1 + K_{eq}C_\infty}{2K_{eq}C_\infty} \pm \sqrt{\left[\frac{1 + K_{eq}C_\infty}{4K_{eq}C_\infty}\right]^2 - \frac{\Lambda}{K_{eq}C_\infty}} \tag{2.10}$$

for the limit of small $\Lambda\Gamma_{eq}/\Gamma_\infty$. For $\Lambda = 0$ there is a unique non-trivial solution to this equation, meaning that the Langmuir isotherm will absolutely converge to the correct Γ_∞ and K_{eq}. In terms of understanding the influence of $\Lambda \neq 0$ on convergence notice that positive $\Lambda < 4$ can produce a discriminant with imaginary values provided $\Lambda > \Lambda_{crit}$ where $\Lambda_{crit} = [1 + K_{eq}C_\infty]^2/[4K_{eq}C_\infty]$. In terms of curve fitting using the pattern search algorithm this is ideal since only real values would be inputs or outputs i.e. there is a unique real

solution for $\Gamma_\infty/\Gamma_{eq}$. This would suggest that systems possessing large positive values for $4 > \Lambda > \Lambda_{crit}$ will conditionally converge to the correct values for Γ_∞ and subsequently K_{eq}. But for $\Lambda < \Lambda_{crit}$ the discriminant is real suggesting that it is possible to have two real solutions for $\Gamma_\infty/\Gamma_{eq}$. Therefore, any negative Λ satisfies this condition since $K_{eq} > 0$ and $C_\infty > 0$. This is a problematic condition for any minimization algorithm because it suggests two minima exists. Furthermore, if Λ is not close to zero then the expansion of the exponential term performed above requires higher order polynomials in Γ_∞ for better accuracy. So there is a potential for producing multiple local minima when using the pattern search algorithm if $\Lambda < 0$.

2.4.2 *Results: transport parameters*

While the convergence of the objective function for the isotherm and equation of state is conditional the equations themselves are straightforward to manipulate and do not require integration. For this discussion we will focus on using the unknown parameters $(c_{1,n}, c_{2,n}, c_{3,n}) = (K_n, \Gamma_{\infty n}, \Lambda_n)$ in eq. 2.8 to develop a pattern search algorithm. One only needs to provide $(K_{eq,0}, \Gamma_{\infty,0}, \Lambda_0)$ for a range of initial bulk concentrations C_i where $C_s = C_i$ when neglecting depletion. The ability to claim $C_s = C_i$ will be discussed in chapter 3. Then eq. 2.8 must be iterated to find Γ_{eq} for that range of concentrations. For this process we use a bisect method with tolerance control to iterate the solution until the errors between two consecutive steps is less than 5×10^{-16}. Once these values are found the Γ_{eq} values are input into eq. 2.9 and the norm can be determined as the difference between the experimental and numerical values for the surface tension denoted $\gamma_{eq,exp}$ and $\gamma_{eq,num}$, respectively.

Initial values for the unknowns $(c_{1,0}, c_{2,0}, c_{3,0}) = (K_{eq,0}, \Gamma_{\infty,0}, \Lambda_0)$ are chosen based on available data for these parameters. The bulk surfactant distribution coefficient $K_{eq,0}$ is never negative so we choose values that are initially greater than 1. The ΔK_{eq} is chosen to be $0.1\Delta K_{eq}$. The molecular interaction parameter Λ_0 must be less than 4, and can be negative. To remove any bias from the initial choice we choose this value as initially zero

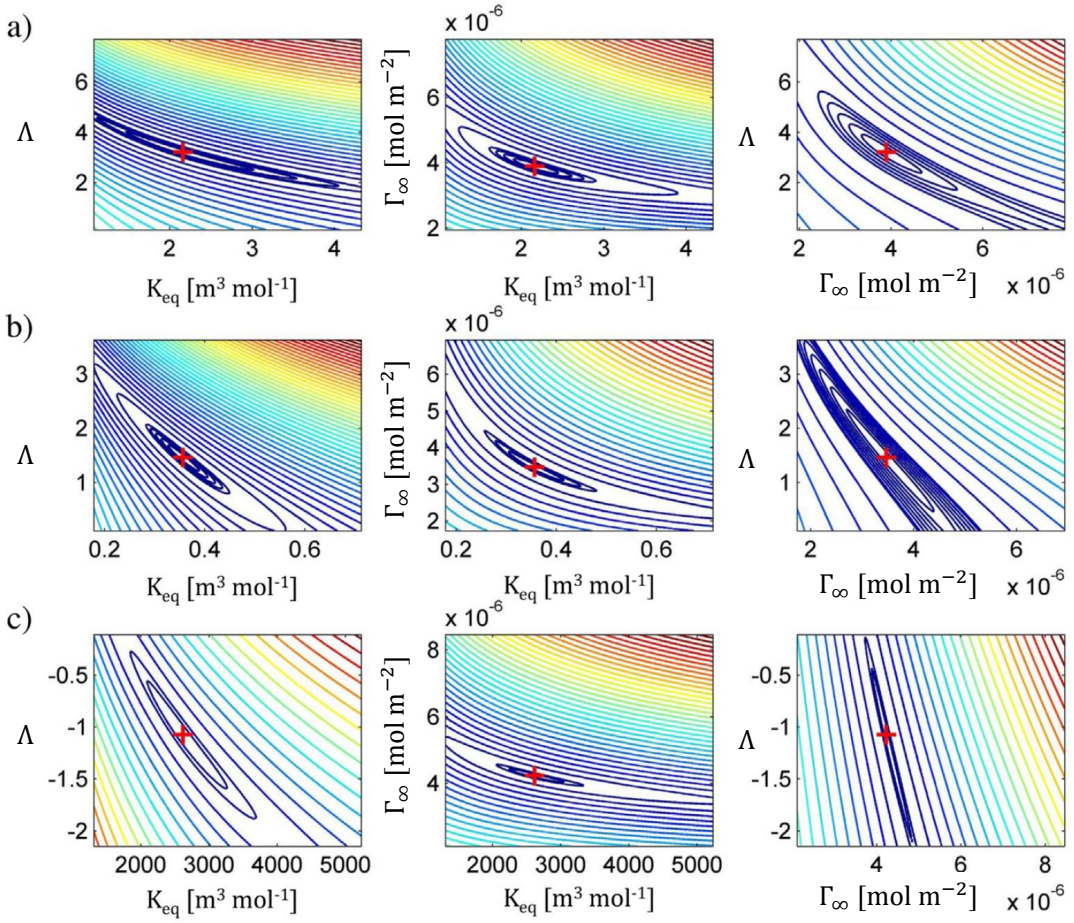

Figure 2.5 *Graphs of the objective function in either* Λ-K_{eq}, Γ_∞-K_{eq} *or* Λ-Γ_∞ *plane for a) aqueous SO in mineral oil (pendant drop), b) SDS in air (69) (du Noüy ring) and c) aqueous* $C_{12}E_4$ *in air (pendant drop) (64). The red + shows the equilibrium value found using the pattern search algorithm.*

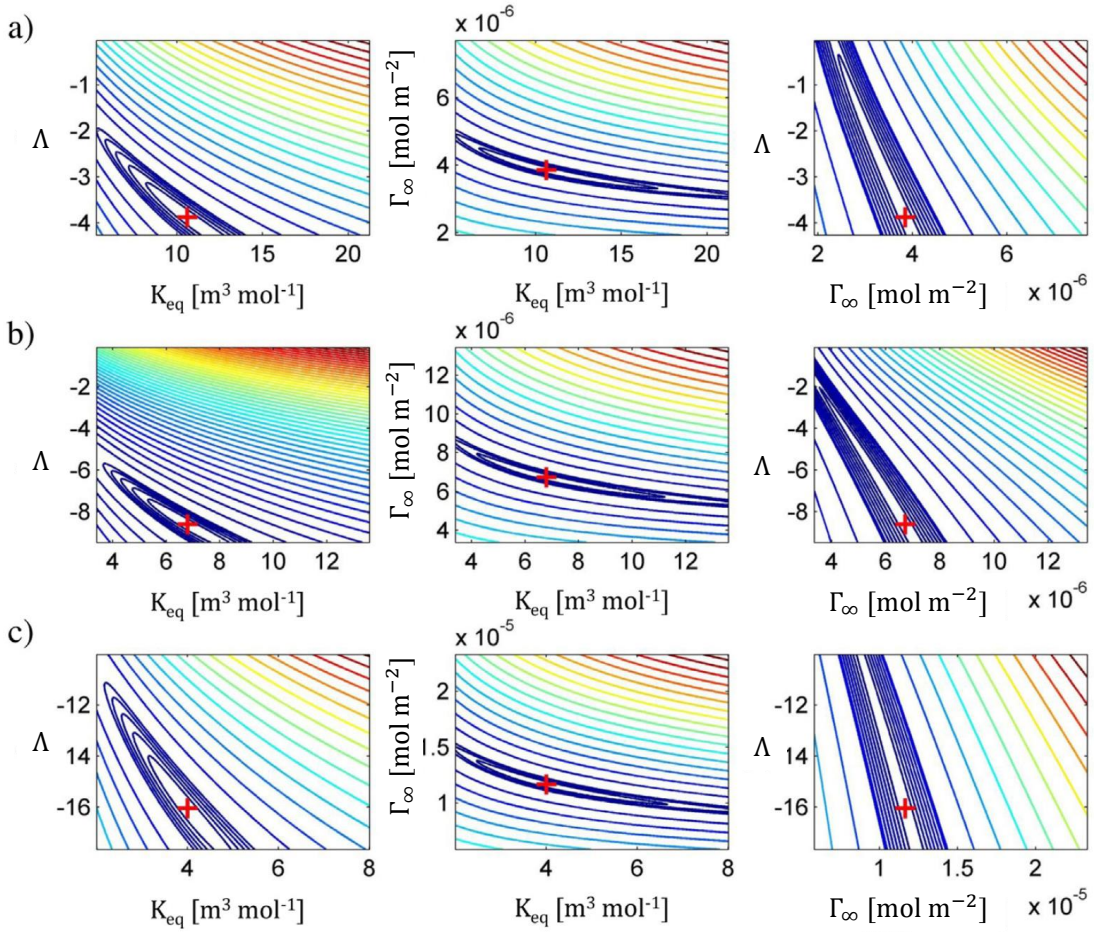

Figure 2.6 *Graphs of the objective function in either* Λ-K_{eq}, Γ_∞-K_{eq} *or* Λ-Γ_∞ *plane for aqueous SDS in mineral oil a)-c). The red + shows the equilibrium value found using the pattern search algorithm with three different initial conditions a)-c).*

with $\Delta\Lambda = 0.1$. The maximum surface coverage Γ_∞ can have the most salient influence on the final result because, as mentioned in previous paragraphs, Γ_{eq} is also an unknown and the ratio of these two variables appears in both the isotherm and equation of state. We choose an initial value of $\Gamma_{\infty,0} = 1 \times 10^{-5}$. The value for $\Delta\Gamma_\infty = 0.01\Gamma_{\infty,0}$ is seen to provide fast convergence. Note that the stencil size for this algorithm is 3^p where $p = 3$ or 27. So 27 calculations are required to determine the path to the local minimum if it exists. Assigning address values begin from left to right, top to bottom, then front to back. Therefore, the central coordinate, used as the location for the initial and updated point, is located at address 14.

The algorithm is applied to several sets of data for γ versus C_i to show the range results when using the pattern search method. The sets include two pendant drops and one pendant bubble study: aqueous sodium oleate (SO) drops in mineral oil, aqueous sodium dodecyl sulfate (SDS) drops in mineral oil, and air bubbles in aqueous $C_{12}E_4$ (64). We also include two historical studies involving aqueous SDS in air (66; 67) where equilibrium surface tension values are determined by foaming (68) and du Noüy ring (69) methods. The authors of this paper have produced the data for the two liquid-liquid pendant drop surface tension measurements.

The objective function for the three dimensional isotherm curve fits are shown in each of three planes $\Lambda - K_{eq}$, $\Gamma_\infty - K_{eq}$ and $\Lambda - \Gamma_\infty$ in Figs. 2.5 and 2.6 in the vicinity of the local minimum. Fig. 2.5(a)-(c) shows data for (a) aqueous SO in mineral oil (pendant drop), (b) aqueous SDS in air (69) (du Noüy ring), and aqueous $C_{12}E_4$ in air (64) (pendant bubble). The red cross in each plot denotes the location of the minimum determined from the pattern search algorithm. Each row corresponds to the computation of the objective function for a given system. In each plot there is a clear local minimum as defined by the closed circles that surround the red cross in each graph. Fig. 2.6 shows data for the aqueous SDS in mineral oil (pendant drop) system. The initial conditions $(K_{eq,0}, \Gamma_{\infty,0}, \Lambda_0)$ are varied to produce the three plots as indicated in the caption. Unlike the previous set of plots these do not

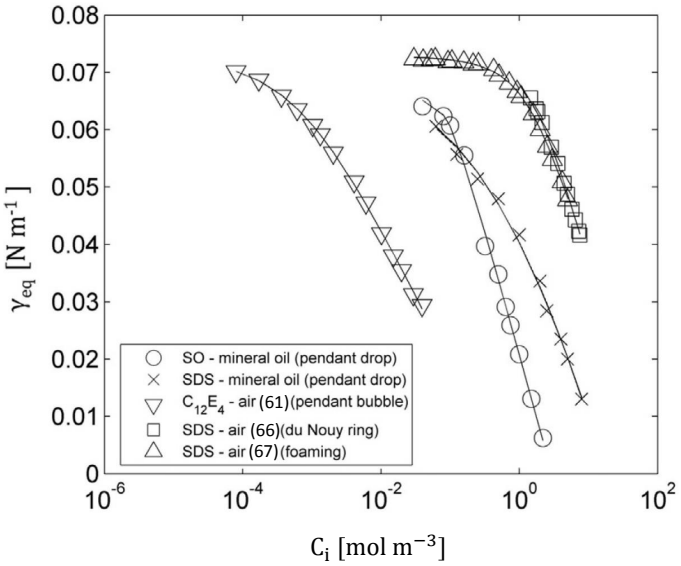

Figure 2.7 *Plots of equilibrium surface tension versus bulk concentration for sodium oleate (SO) and sodium dodecyl sulfate (SDS). The lines are the best fit curve generated from the pattern search algorithm.*

necessarily yield closed domains in the first and last columns of data. They do appear to close if the graphs were continued in the positive Λ direction but this is difficult to say with certainty since the graphs evolve in three-dimensions.

The results of the pattern search minimization procedure are shown in Fig. 2.7 through plots of γ versus C_i for each system. The bulk surfactant concentrations span 10^{-4} to 10 mM when including all the data sets. The individual data sets span a much smaller range of about two orders of magnitude for each system. The $C_{12}E_4$ non-ionic surfactant data spans the lowest concentration values while the SDS surfactant systems span the largest. The surface tension values range from a minimum less than 10 mN m^{-1} for the aqueous SO in mineral oil to values that are near the clean interface case for water in air 72 mN m^{-1} and water in mineral oil 67 mN m^{-1}. For the SDS in mineral oil data the minimization values for each of the three different initial conditions is plotted on the same figure where the lines overlap.

2.5 Discussion

The pattern search method appears to be a robust and efficient means of finding the best fit of eqs. 2.4-2.6 for a given experimental drop shape. The pattern search algorithm was capable of fitting pendant drop and bubble halves with surface tensions up to 72.39 mN m^{-1} and as low as 0.54 mN m^{-1} using the same initial guess for γ as shown in Fig. 2.3. The drop and bubble in Fig. 2.4(b) and 2.4(c) have lower Bo^* and this typically means the pendant drop method risks returning less accurate results (51). The corresponding contour plots of ψ_R in Fig. 2.3(b) and 2.3(c) provide a visual explanation. When compared to the drop in Fig. 2.4(a), the level curves of ψ_R become elongated in the γ-direction as you approach the best fit. Given that the same convergence criteria is used in Fig. 2.3(a)-(c), this means that a wider range of γ could satisfy those criteria in Fig. 2.3(b) and 2.3(c). This effect would become magnified as the drop shape approaches a sphere, leading to a wider range γ potentially satisfying the convergence criteria. Then in order to accurately fit a low Bo^* drop, one would need a sufficient combination of high image resolution and strict convergence criteria.

Using $\gamma_0 = 5\Delta\rho g b_x^2$, the four example fits of I_R in Fig. 2.3 were determined within 0.95 and 1.54 s for pendant drops and bubbles with widely varying sizes and γ. Further analysis of the computation time is provided in Fig. 2.10 where transient surface tension measurements of a 2 mM SO drop in mineral oil are plotted. In Fig. 2.10(a) $\gamma(t)$ is shown representing successive fits to experimental pendant drop images taken every 10 s for just over 6 min. Figure 2.10(b) then shows the time taken to fit both I_L and I_R for each image, t_{calc}. For each image I_L and I_R had roughly 630 coordinates. The Bo^* for the first image in Fig. 2.10(a) is 0.073 and at the last image $Bo^* = 0.15$. The first image took nearly 4 s to fit, but subsequent images took roughly half the time since initial guesses for b_0 and γ_0 were taken as the solution of the previous time step. The total time taken to fit the 39 images in Fig. 2.10 is 77.3 s or 1.98 s per image. This is significantly faster than the time interval between successive images. Thus the pattern search algorithm can be used to fit experimental images

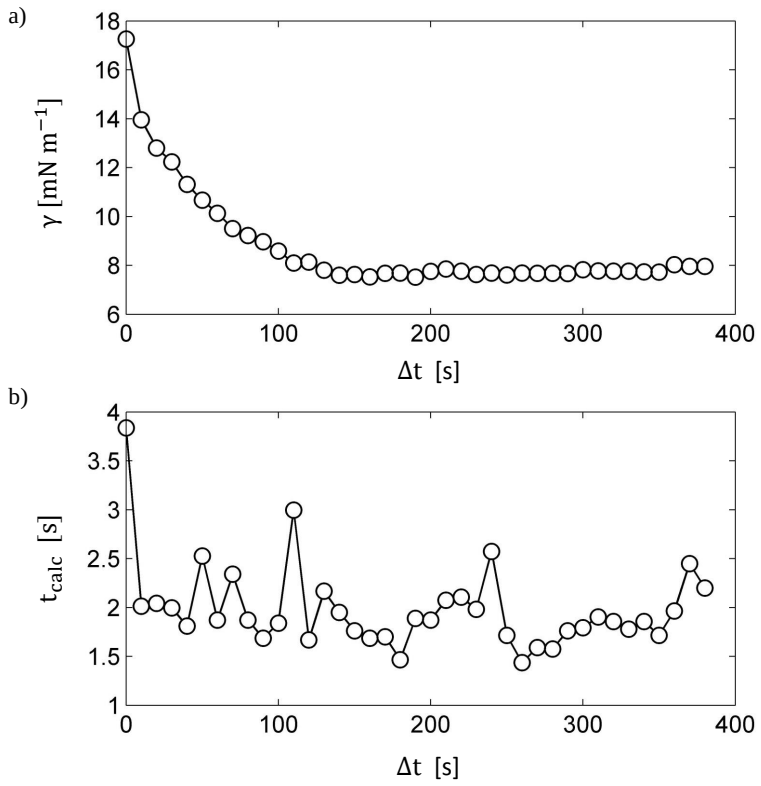

Figure 2.8 *A plot of (a) $\gamma(t)$ for a drop of 2 mM SO in mineral oil is shown along with (b) the total time taken to fit eqs. 2.4-2.6 to both I_L and I_R for each experimental image.*

while the images are being captured simultaneously. This would be true for many pendant drop experiments save for ones requiring very short time intervals between images.

A summary of the estimates for the surfactant transport parameters determined by fitting the equilibrium surface tension data to the three parameter Frumkin isotherm are presented in Table 1. The first column show the estimates for Γ_∞ where all values are similar and range from 3.47-4.22 $\times 10^{-6}$. The SDS in air (69) has the lowest value while the non-ionic $C_{12}E_4$ has the largest. The trends are similar for the estimates for the bulk surfactant distribution coefficient K_{eq} which span some 4 orders of magnitude for the range of data presented.

Perhaps the most interesting results from the estimates of the surfactant transport parameters appear in the last two columns which provide information for the molecular interaction

Table 2.1 *Frumkin isotherm model constants.*

	Γ_∞ mol m^{-2}	K_{eq} m^3 mol^{-1}	Λ –	Λ_{crit} –
SO - mineral oil (pendant drop)	3.89×10^{-6}	2.16	3.21	1.89
SDS -mineral oil (pendant drop)	3.84×10^{-6}	10.6	-3.88	21.7
$C_{12}E_4$ - air (64) (pendant bubble)	4.22×10^{-6}	2615	-1.07	33.18
SDS - air (68) (foaming)	3.86×10^{-6}	0.214	2.02	1.07
SDS - air (69) (du Noüy ring)	3.47×10^{-6}	0.356	1.45	1.30

parameter. This parameter has been the subject of much debate where it is now generally understood that there is an upper limit of $\Lambda = 4$ above which the isotherm provides multiple solutions. Here we have proposed another critical Λ based on the C_∞ (57) and K_{eq} which may be initiated using data provided from the Langmuir isotherm. For $\Lambda > \Lambda_{crit}$ there is only one unique solution to Eq. 2.10 used to determine stability. This hypothesis is confirmed in the set of data presented in Table 1. Therefore, any negative Λ should be viewed with suspicion given this criteria. In this regard the equilibrium surface tension data for the SDS-mineral oil does produce multiple solutions where we have chosen the smallest value because it provides the smallest Γ_∞ (largest ratio of $\Gamma_{eq}/\Gamma_\infty$). The $C_{12}E_4$ also produces a negative Λ but is a special case because the discriminant in Eq. 2.10 is extremely small such that it is essentially the same as having one unique non-trivial solution i.e. it is conditionally stable. This is somewhat confirmed in the plots shown in Fig. 2.5 where the objective functions for $C_{12}E_4$ has a very narrow band in both planes containing Λ. So for systems with large K_{eq} it is possible to find a unique solution through minimization.

2.6 Conclusions

Surface tension measurements were made using axisymmetric drop shape analysis (ADSA) of a pendant drop with the pattern search method as the minimization algorithm. Here, it has been successfully used to fit ADSA data to numerical solutions of Young-Laplace equa-

tion without the need to calculate gradients. This is in contrast to the otherwise nearly universal use of gradient based minimization methods (16). The non-gradient based Nelder-Mead simplex method (49) has been used in the context of the pendant drop method by using the MATLAB function *fminsearch* (51), but the pattern search method used here has been mathematically proven to be capable of consistently converging to a local minimum (52; 53).

After producing equilibrium surface tension data from pendant drops for aqueous sodium oleate (SO) and sodium dodecyl sulfate (SDS) in mineral oil we fit this data to the Frumkin isotherm also using the pattern search method. We analyze the convergence criteria for the equation and extend the upper bound limit for the molecular interaction parameter Λ using a Taylor series expansion of the Frumkin isotherm equation for small fractional surface coverage. The curve fits from the pattern search method and stability criteria determined from linearization of the Frumkin isotherm fit the data fairly well.

Future analysis of the pattern search method for ADSA should include sessile drops. It may also be possible to apply the method for direct estimates of adsorption/desorption rates in single and multi-surfactant systems using transient surface tension data.

2.7 Addendum - Drop trace refinement

In section 2.3.1 a simple threshold analysis was used to define pixels in an experimental image either occupied by the pendant drop or occupied by the continuous phase (55). The drop surface was then traced, the trace being at the mercy of the image resolution. This served the purposes of the original publication well, particularly because the image resolution was high (1200×1600 pixels). However as studied by other authors (54), an estimate of pendant drop surface coordinates with sub-pixel resolution can be achieved through an additional fitting process. Since the publication of the original article above, such a process has been added to the pendant drop surface tension measurement program and is yet another application of the pattern search algorithm.

In ref. (54), after making an initial trace of the drop surface, at each original surface coordinate a sigmoid function was fit to the pixel value profile in the direction normal to the drop surface. After determining the best fit of the sigmoid function to the pixel value profile, the surface coordinate was adjusted so that it matched the inflection point of the function. The result is a refined drop trace with sub-pixel resolution. The authors found that the additional trace refinement had little effect on well-deformed drops. Where the trace refinement can be particularly beneficial is for low-resolution images, less-deformed (more spherical) drops, and observing changes in surface tension for a single drop over small time steps.

In our edge refinement algorithm we similarly make an initial trace using the threshold analysis and tracing algorithm described earlier. At each initial surface coordinate a slice of the pixel value profile is taken. The direction of the slice is not necessarily normal; instead it is either horizontal, vertical, at 45° going up from left to right, or at 45° going down from left to right. The direction of the slice is chosen to best approximate the normal direction at each point. The number of pixels at either side of the original surface coordinate is chosen as 15, however it should be noted that this may need to be adjusted based on image resolution and contrast. The result is a profile of pixel values p versus pixel location s. Next a sigmoid function is defined,

$$g(s) = \frac{p_2 - p_1}{1 + \exp[-B(s - s_0)]} + p_1, \tag{2.11}$$

where p_2 is the upper asymptote of the sigmoid, p_1 is the lower asymptote, s_0 is the location of the inflection point of the sigmoid, and B dictates the maximum slope of the sigmoid. In ref. (54) a similar function was used, and all four of the aforementioned constants were determined using a multivariate fitting procedure. This added another computationally expensive routine to the overall process, and would not be suitable when fitting many pendant drop images over time. Instead we assume p_2 is the maximum pixel value in the slice and p_1

is the minimum value. We are then left with two unknowns, s_0 and B, which we determine with the efficient pattern search algorithm.

In Fig. 2.7 an example slice of pixel values for a 40 μl aqueous 1 mM SDS drop suspended in 1000 cSt Si oil is shown. In 2.7(a) the pixel values from the image are the white circles and the solid black line is the best fit of the sigmoid function. The initial and new surface coordinates are labeled. Figure 2.7(b) shows the gray scale image of the drop with the location of the slice shown.

The improvement in the drop trace is shown in Fig. 2.7. In Fig. 2.7(a) the raw image of the drop is shown and the drop trace is shown in white. A blown up view of the region indicated in Fig. 2.7(a) is shown in Fig. 2.7(b). Here the original trace is shown as gray squares and the new trace with sub-pixel resolution is shown as white circles.

Using this drop trace refinement process has several advantages. First it is clear in Fig. 2.7(b) that the refined trace is smoother and more accurate. As a result subtle changes in the drop shape can be more easily detected. This makes fitting successive images of a single drop over short time steps a possibility, and it also can make fitting drops that are more spherical in shape more accurate. Additionally this means lower resolution images can be used with likely comparable accuracy to higher resolution images that take up considerably more space on computer hard drives. Finally this trace refinement step could eliminate the effects of gradients in lighting that may sometimes find themselves in experimental images.

As this is merely an addendum to the originally published article, any additional analysis of improving the drop trace step will be saved for future work. Future work may include a detailed analysis on how sub-pixel resolution traces impact transient surface tension measurements using many successive images. This would involve understanding limits in time steps for observing a measurable change in surface tension, and finding a balance between the added computation time for the trace refinement step and added accuracy in the surface tension results.

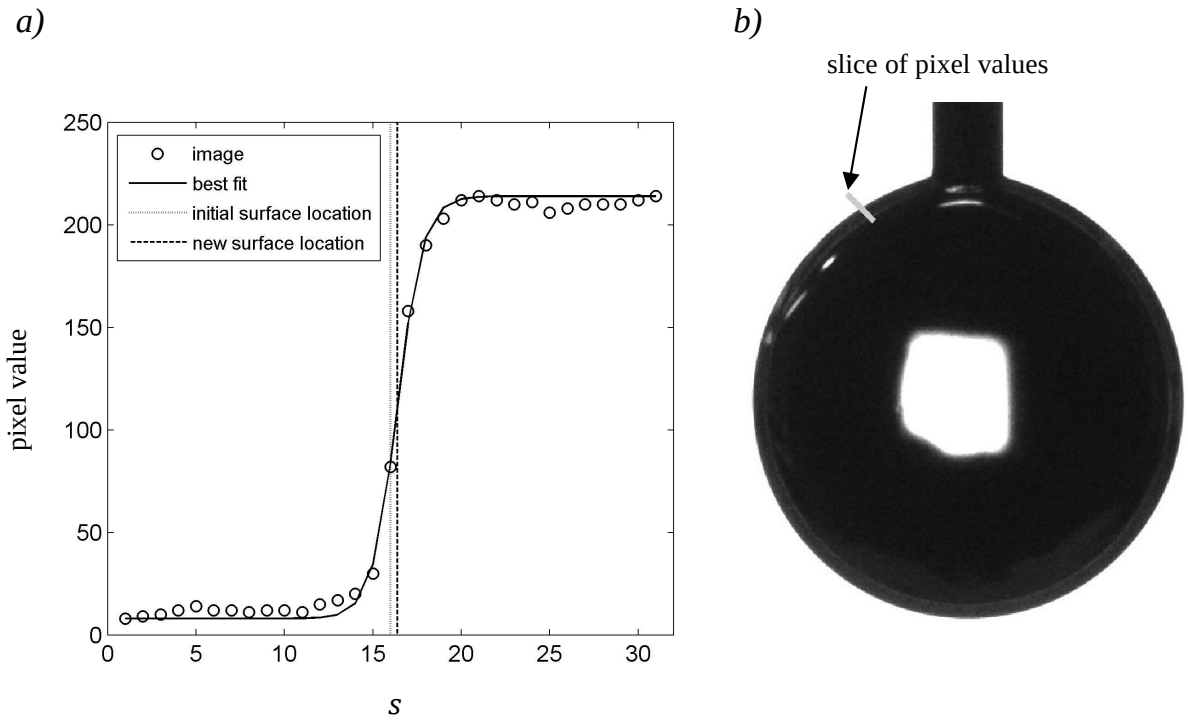

Figure 2.9 *In (a) a slice of pixel values is shown corresponding to the slice shown in (b). The solid black line is the best fit of the sigmoid function. The dashed line is the original guess at the surface coordinate and the dotted line is the new surface coordinate with sub-pixel resolution.*

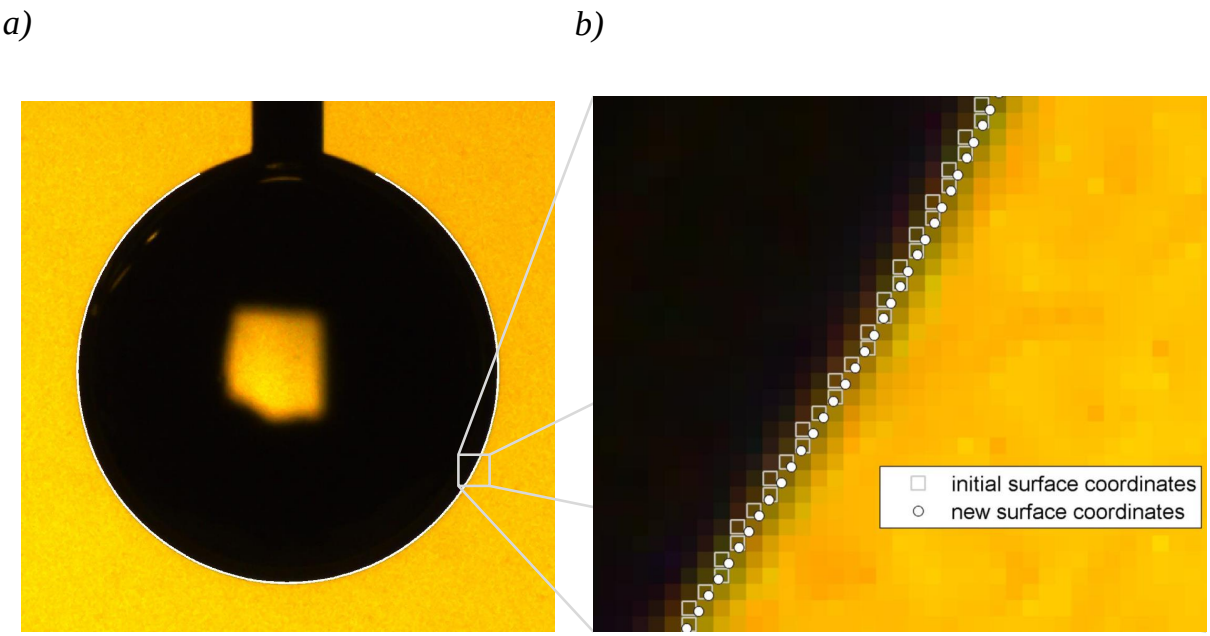

Figure 2.10 *A 40 µl aqueous drop containing 1 mM SDS is suspended in 1000 cSt Si oil. In (a) the white line is the drop trace with sub-pixel resolution. In (b) the original trace (gray squares) is compared to the new sub-pixel resolution trace (white circles) in the region indicated in (a).*

CHAPTER 3. DETERMINING EQUILIBRIUM SURFACTANT TRANSPORT PARAMETERS FROM PARTIALLY DEPLETED PENDANT DROPS

3.1 Introduction

When a surfactant is present in one phase and is insoluble in the other, a commonly used isotherm and equation of state is the Frumkin model (45; 64; 65) like that used in chapter 2:

$$\theta_{eq} = \frac{K_{eq} C_{eq}}{K_{eq} C_{eq} + e^{-\Lambda \theta_{eq}}}, \tag{3.1}$$

$$\gamma_{eq} = \gamma_0 + n \hat{R} T \Gamma_\infty \left[\frac{1}{2} \Lambda \theta_{eq}^2 + \ln\left(1 - \theta_{eq}\right) \right]. \tag{3.2}$$

Here $\theta_{eq} = \Gamma_{eq}/\Gamma_\infty$ is the fractional surface coverage at equilibrium, Γ_∞ is the maximum surface concentration assuming a monolayer with maximum packing, γ_0 is the surface tension for a clean ($\theta_{eq} = 0$) surface, K_{eq} is the surface-bulk distribution coefficient, $\hat{R}$ is the ideal gas constant, and T is temperature. The interaction parameter Λ accounts for non-ideal interactions between surfactant molecules where a positive value indicates net attraction and a negative value indicates net repulsion. The coefficient n is 2 for 1:1 ionic surfactants and 1 for non-ionic surfactants (63).

In practice eqs. 3.1 and 3.2 are fit to experimental surface tension data, for example using pendant drop or bubble tensiometry as in chapter 2, to determine K_{eq}, Γ_∞ and Λ which are important in modeling various fluid dynamics problems involving surfaces. Typically

when fitting to the surface tension data it is assumed that $C_{eq} = C_i$. However for certain surfactants, as the ratio of surface area to surfactant-containing volume becomes larger or as bulk surfactant concentrations become smaller, it is possible that enough surfactant will adsorb such that the bulk concentration depletes significantly relative to the initial concentration C_i (70; 71; 72; 73). In such a case eqs. 3.1 and 3.2 cannot be fit to experimental data unless C_{eq} can be determined.

Determining if depletion in the bulk will be significant and to what degree has been investigated for surfactant transport to fluid-fluid interfaces where surfactant originates in one phase and is insoluble in the other. A global mass balance combined with the Langmuir isotherm (eq. 3.1 when $\Lambda = 0$) results in two dimensionless parameters (73): a surface-bulk distribution parameter $f^* = \frac{K_{eq}\Gamma_\infty A_s}{V}$ and a bulk mass loss parameter $\zeta^* = \frac{\Gamma_\infty A_s}{C_i V}$. The superscript '$*$' indicates dimensionless quantities. Here A_s is the surface area and V is the volume of the surfactant-containing phase.

The parameter f^* is the ratio of the maximum number of molecules of surfactant that can absorb to the surface, $\Gamma_\infty A_s$, to what can be interpreted as the potential for a molecule of surfactant in the bulk to adsorb to the surface at equilibrium, V/K_{eq}. When f^* is small there is a relatively low likely hood that a surfactant molecule will adsorb relative to the number of adsorption sites available, and when f^* is large the number of molecules likely to adsorb becomes significant relative to the number of adsorption sites. The bulk mass loss parameter ζ^* is a ratio of the quantity $\Gamma_\infty A_s$ to the number of molecules of surfactant initially present in the bulk, $C_i V$. When ζ^* is small there is a relative abundance of surfactant molecules in the system compared to the number of adsorption sites, whereas when ζ^* is large there are many more adsorption sites than surfactant molecules in the system. In general when both of these quantities are small depletion in the bulk becomes less likely. In ref. (73) the authors determined that, for equilibrium conditions, a small $f^* \sim O(10^{-2})$ will prevent depletion in the bulk. Above this limit, the combination of increasing f^* and ζ^* will increase the effects of depletion.

Researchers have also taken advantage of depletion to make better estimates of surfactant and protein adsorption at an air-liquid interface by comparing pendant drop and pendant bubble tensiometry measurements for a given system (70; 71; 72; 74). Their pendant bubble measurements were unaffected by depletion since the surfactant-containing continuous phase volumes were large. On the other hand their pendant drops were affected by depletion. However when γ_{eq} is the same for the pendant drop and pendant bubble that means Γ_{eq} must also be the same for both cases according to eq. 3.2. Thus when the surface tensions were equal the difference in initial bulk concentrations between the drop $C_{i,D}$ and bubble $C_{i,B}$ along with knowledge of the pendant drop volume V_D and drop surface area A_D was used to estimate the surface concentration $\Gamma_{eq} = \frac{A_D}{V_D}(C_{i,D} - C_{i,B})$.

Situations may arise where pendant drop experiments cannot be designed to neglect the effects of depletion, for example if limited or expensive materials are under investigation. However by using a global mass balance along with eqs. 3.1 and 3.2 it will be shown that the fitting parameters K_{eq}, Γ_∞ and Λ can still be determined directly from such experiments. In this chapter the Frumkin isotherm incorporating a global mass balance will be used with eq. 3.2 to fit pendant drop tensiometry experiments when depletion cannot be neglected. Additionally a better understanding of the limits of f^* and ζ^* to produce a significant change in γ_{eq} will be established for different Λ. This predictive analysis will be useful in not only designing pendant drop experiments but in controlling depletion in any number of interfacial fluid mechanics problems.

In the next section the Frumkin isotherm incorporating the global mass balance will be presented followed by an analysis of the limits of ζ^* and f^* to prevent a significant change in γ_{eq}. This will be followed by a description of pendant bubble and drop experiments. Finally results of the pendant drop and bubble experiments and fits to the modified Frumkin isotherm will be presented along with some conclusions.

3.2 Analysis

Consider a surface with area A_s separating two immiscible fluids. In one phase surfactant is present which will adsorb to the surface. At equilibrium the number of surfactant molecules adsorbed to the surface is $\Gamma_\infty \theta_{eq} A_s$ and the amount of surfactant molecules remaining in the bulk volume is $C_{eq}V$. Using the initial amount of molecules in the bulk volume $C_i V$, a global mass balance can be established, $C_i V = C_{eq}V + \Gamma_\infty \theta A_s$. Inserting eq. (3.1) into this mass balance yields a quadratic equation in terms of C_{eq} similar to ref. (73) which has the positive root

$$C_{eq} = \frac{1}{2} C_i \left[1 - \frac{\zeta^*}{f^*} e^{-\Lambda\theta} - \zeta + \sqrt{\left(\frac{\zeta^*}{f^*} e^{-\Lambda\theta} + \zeta^* - 1 \right)^2 + 4 \frac{\zeta^*}{f^*} e^{-\Lambda\theta}} \right]. \tag{3.3}$$

This equation predicts the change in bulk concentration given ζ^*, f^* and Λ. Since C_{eq} can be predicted with eq. 3.3 one can then insert it back into eq 3.1 to yield a modified Frumkin isotherm which accounts for depletion,

$$\theta = \frac{\frac{1}{2} K_{eq} C_i \left[1 - \frac{\zeta^*}{f^*} e^{-\Lambda\theta} - \zeta + \sqrt{\left(\frac{\zeta^*}{f^*} e^{-\Lambda\theta} + \zeta^* - 1 \right)^2 + 4 \frac{\zeta^*}{f^*} e^{-\Lambda\theta}} \right]}{e^{-\Lambda\theta} + \frac{1}{2} K_{eq} C_i \left[1 - \frac{\zeta^*}{f^*} e^{-\Lambda\theta} - \zeta + \sqrt{\left(\frac{\zeta^*}{f^*} e^{-\Lambda\theta} + \zeta^* - 1 \right)^2 + 4 \frac{\zeta^*}{f^*} e^{-\Lambda\theta}} \right]}. \tag{3.4}$$

This isotherm can be used with eq 3.2. Note that when using eq 3.4 instead of eq 3.1 no new fitting parameters have been added aside from the geometry A_s and V which should be known i.e. the fitting parameters remain Γ_∞, K_{eq} and Λ. This modified Frumkin isotherm can be used to fit γ_{eq} versus C_i data using existing methods such as in chapter 2 as long as A_s and V are known even if depletion is significant.

Now for a single combination of surfactant and two immiscible fluids, consider one case where depletion does not occur and one case where depletion does occur. The case *with*

depletion will result in a surface tension $\gamma_{eq,2}$ that is greater than the case *without depletion*, $\gamma_{eq,1}$. We will define the error between the two cases as

$$\chi = \frac{\gamma_{eq,2} - \gamma_{eq,1}}{\gamma_{eq,1}}. \tag{3.5}$$

Using the Frumkin equation of state this quantity is identical to

$$\chi = \frac{\frac{1}{2}\Lambda(\theta_{eq,1}^2 - \theta_{eq,2}^2) + \ln\left(\frac{1-\theta_{eq,1}}{1-\theta_{eq,2}}\right)}{\frac{1}{2}\Lambda\theta_{eq,1}^2 + \ln(1-\theta_{eq,1})} \tag{3.6}$$

where $\theta_{eq,1}$ and $\theta_{eq,2}$ are the equilibrium surface coverages for the cases without and with depletion, respectively. For a given error in surface tension values χ and surface coverage without depletion $\theta_{eq,1}$, eq. 3.6 can be used to get $\theta_{eq,2}$ using standard numerical methods such as the secant method. Thus the change in surface coverage corresponding to a particular error in γ_{eq} due to depletion can be determined.

Moving on, for a given $\theta_{eq,1}$ and $\Lambda < 4$ (62) there exists a single quantity $K_{eq}C_i$. Note that the quantity ζ^*/f^* is identical to $(K_{eq}C_i)^{-1}$. Then for the given $\theta_{eq,1}$, Λ and χ, by using eq. 3.1 to determine $K_{eq}C_i$ and eq. 3.6 to determine $\theta_{eq,2}$, there is only a single unknown in eq. 3.4 which is ζ^*. Equation 3.4 can be solved numerically for ζ^* using the $\theta_{eq,2}$ and $K_{eq}C_i$ that correspond to a given $\theta_{eq,1}$, Λ and χ. The returned value of ζ^* is the maximum allowable ζ^* to keep the error in surface tension due to depletion less than χ. The result of the above analysis is the ability to predict when depletion will cause a certain amount of error in γ_{eq} for a given ζ^*, $K_{eq}C_i$ and Λ.

3.3 Experimental Section

Surface tension measurements were made using the pendant drop or bubble method, the theory of which can be found in good detail elsewhere (16; 17). A 100 μl Hamilton Gastight syringe was used with either a straight 22 gauge stainless steel needle for pendant drops

or an inverted 14 gauge J-needle (Ramé-Hart) for pendant bubbles. For pendant bubble measurements a 25×25×50 mm transparent acrylic cell was filled with reverse osmosis filtered water containing between 0.001 and 0.03 mM > 98.0% tetraethylene glycol monododecyl ether ($C_{12}E_4$) (Sigma-Aldrich). An air bubble was generated by submerging the J-needle in the $C_{12}E_4$ solution and displacing 10 μl of air in the syringe using a syringe pump (New Era Pump Systems). For pendant drop experiments the same acrylic cell was partially filled with reverse osmosis water below the reach of the needle and the cell was sealed so that the remaining air in the cell could become nearly saturated with water vapor. The straight 22 gauge needle was inserted through a small hole in the seal and a pendant drop of water containing some initial bulk concentration of $C_{12}E_4$ was suspended in the water vapor-saturated air within the cell. This prevented the drop from evaporating as best as possible (70). Pendant drop volumes were 2.5 and 6.5 μl.

A CCD camera (PixeLINK) was used to take images of the drop or bubble over time while a lamp illuminated the drop or bubble from the side opposite of the camera. Intervals between images were between 5 and 30 s and experiments lasted up to several hours. The in-house MATLAB program described in chapter 2 was used to extract experimental drop and bubble shapes from the images and compare them to solutions of the Young-Laplace equation (16; 17). Best fits of the Young-Laplace equation were determined using the in-house program incorporating a 2-parameter pattern search algorithm. The resulting equilibrium surface tension data was fit to the isotherm and equation of state discussed in the next section to determine the fitting parameters Γ_∞, K_{eq} and Λ. Best fits of the isotherm and equation of state were determined using a 3-parameter pattern search algorithm as was done in chapter 2.

3.4 Results and Discussion

Before looking at the experimental results we can predict if any of the pendant bubble or pendant drop experiments involving $C_{12}E_{4(aq)}$ will be subject to depletion in the bulk

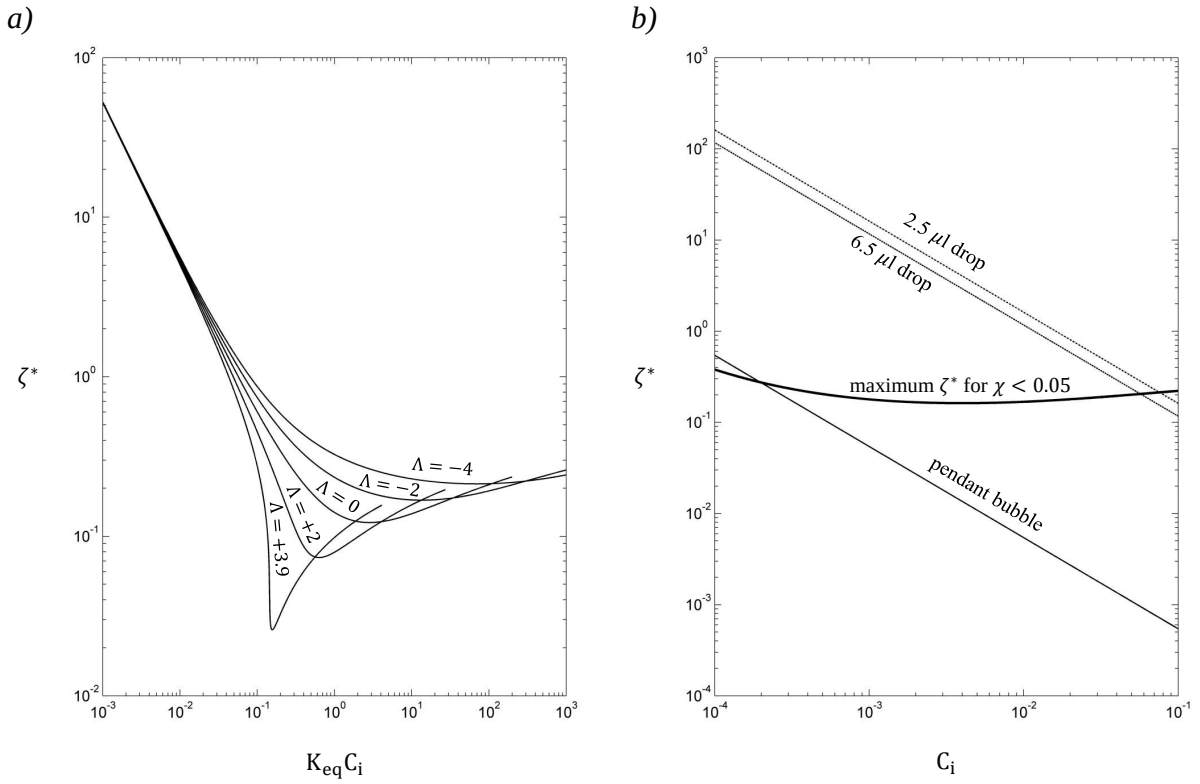

Figure 3.1 *In (a) the maximum allowable ζ^* versus $K_{eq}C_i$ for different Λ to keep $\chi < 0.05$ is shown. In (b) the estimated ζ^* for the pendant bubbles and drops is shown, and the cut-off line for when depletion will cause $\chi > 0.05$ is shown.*

phase. Using the analysis described above in section 3.2, we can predict the maximum allowable $\zeta^* = \frac{\Gamma_\infty A_s}{C_i V}$ for different $K_{eq}C_i$ to prevent a change χ in γ_{eq} relative to a case without depletion. This is demonstrated in Fig. 3.1(a) where a threshold of $\chi = 0.05$ was chosen. For a range of Λ values from -4 to +3.9, the solid lines represent the maximum ζ^* allowed to prevent γ_{eq} from changing by more than 5% relative to a case without depletion. At very low bulk concentrations, depletion can be significant but its effect on surface tension is not since the $\theta_{eq} = 0$ surface tension γ_0 is approached here. Therefore it is possible to get away with relatively large ζ^* without affecting γ_{eq}. Approaching $K_{eq}C_i = 0.1$ differences begin to emerge depending on the value of Λ. For positive Λ which indicates net attraction between surfactant molecules, adsorption is enhanced and so depletion becomes a greater issue. Negative Λ has the opposite effect. Generally speaking, for $K_{eq}C_i$ greater than 0.1 the bulk mass loss parameter should be $\zeta^* < O(0.1)$ to keep $\chi < 0.05$.

For the experiments in this analysis, the $\frac{A_s}{V}$ ratios are 12.0, 2590 and 3570 m^{-1} for the 10 μl pendant bubbles in a 25 mm×25 mm×50 mm volume, the 6.5 μl pendant drops and the 2.5 μl pendant drops, respectively. Note in determining $\frac{A_s}{V}$ for the pendant bubble, A_s includes the surface area of the bubble as well as the area of the free surface of the acrylic box. Using the Frumkin equilibrium sorption parameters from ref. (64) ($\Gamma_\infty = 4.66 \times 10^{-6}$ mol m^{-2}, $K_{eq} = 2840$ m^3 mol-1 and $\Lambda = -1.88$), values for ζ^* can be estimated. In Fig. 3.1(b) plots of ζ^* versus $K_{eq}C_i$ are shown for each pendant bubble and drop. Also the maximum allowed ζ^* to keep $\chi < 0.05$ is shown. This indicates that depletion will not have a significant impact on the pendant bubble experiments. However the two pendant drop experiments will clearly be affected by depletion particularly at lower C_i. As the CMC ($C_i \approx 0.03$ mM) (57) is approached we can expect depletion to have less of an impact on γ_{eq}, but there likely will still be differences between the pendant drops and bubble.

Moving on to the experiments, Fig. 3.2 shows γ versus time data for 0.015 mM $C_{12}E_4$ when using a pendant bubble, the 2.5 μl drop and the 6.5 μl drop. In each case an equilibrium is reached after about 10 min. The 2.5 μl drop shows some small fluctuations which are likely

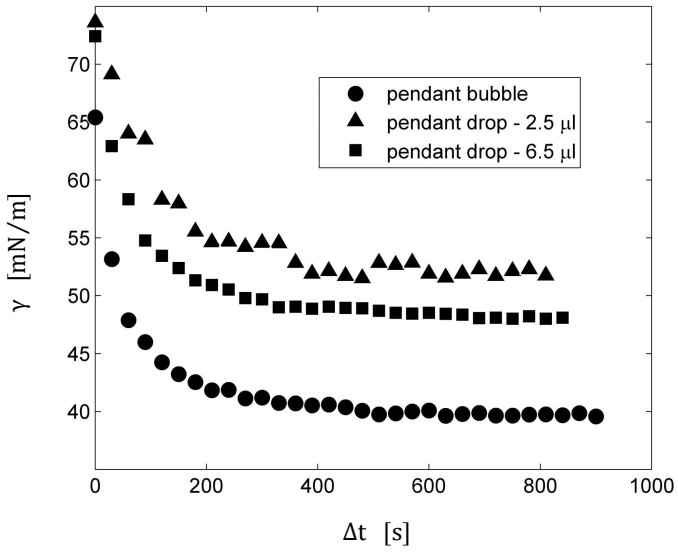

Figure 3.2 *Plots of γ versus time for 0.015 mM $C_{12}E_4$ are shown for pendant bubbles (●), 2.5 µl pendant drops (▲) and 6.5 µl pendant drops (■).*

errors due to the drop being so small and spherical (75). Clearly the equilibrium surface tension values differ between the bubble and two drop volumes.

In Fig. 3.3 the equilibrium surface tension values for the pendant bubble and two pendant drops are shown versus initial concentration C_i. Additionally values for pendant bubbles from ref. (64) are shown to validate our results which are in good agreement. As shown in Fig. 3.2 the equilibrium surface tension values were higher for the pendant drops than the pendant bubble at $C_i = 0.015$ mM. This is true at other initial bulk concentrations as shown in Fig. 3.3(a), making it clear that depletion is significant for the pendant drops as predicted. Even though depletion has significantly affected the γ_{eq} values, eq. 3.2 and 3.4 are used to generate the solid lines of best fit in the figure. The model constants Γ_∞, K_{eq} and Λ corresponding to the best fits are shown in Table 3.1 along with those from ref. (64). The constants for the three systems studied here and the one from ref. (64) are all in excellent agreement.

In the process of fitting eqs. 3.4 and 3.2 the estimated equilibrium bulk concentration C_{eq} is also determined according to eq. 3.3. The equilibrium surface tension values are then

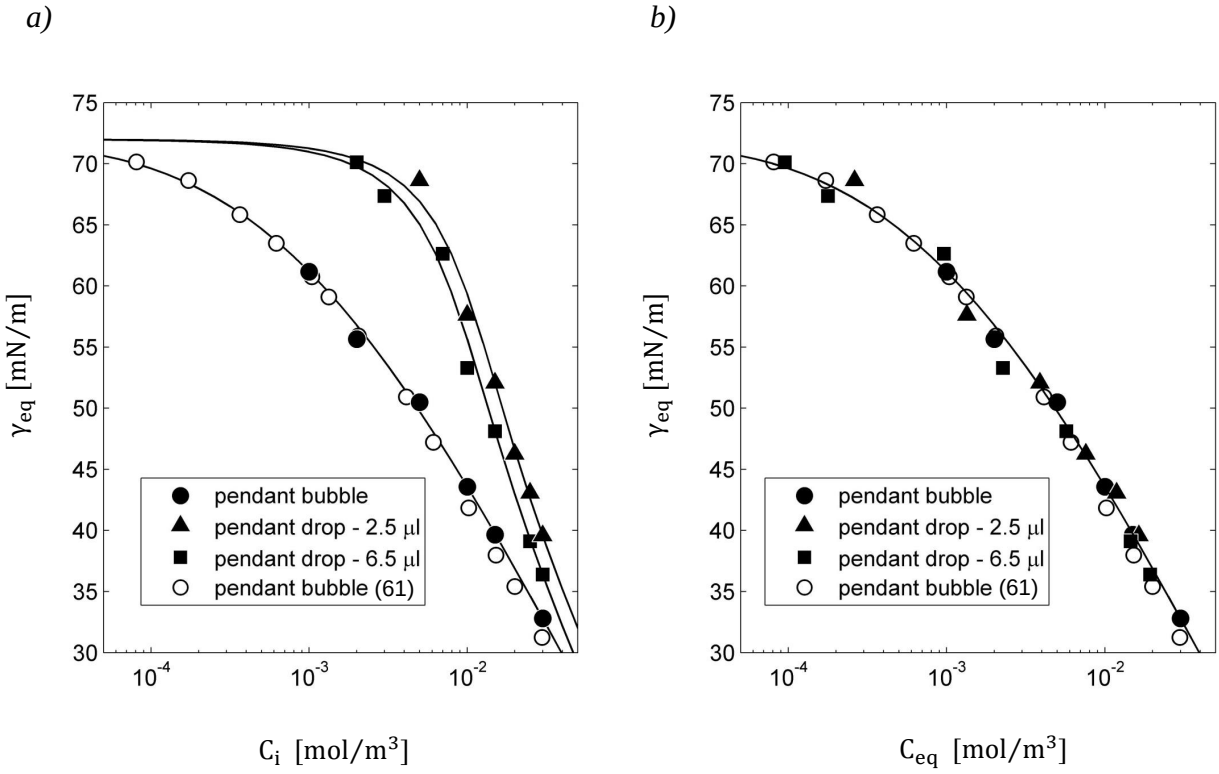

Figure 3.3 *Plots of γ_{eq} versus (a) C_i and (b) C_{eq} are shown for pendant bubbles (●), 2.5 µl pendant drops (▲) and 6.5 µl pendant drops (■). Pendant bubble data from ref. (64) (○) is also shown in (a). Solid lines in (a) are best fits of eqs. [3.2] and [3.4] for each filled-marker data set. In (b) the solid line is a best fit of all data shown.*

Table 3.1 *Model constants corresponding to best fits of eqs. (3.2) and (3.4) as shown in Fig. 3.3. The 'combined fit' are the model constants from Fig. 3.3(b).*

	Γ_∞ mol m^{-2}	K_{eq} m^3 mol^{-1}	Λ –
pendant bubble	4.40×10^{-6}	2920	-1.88
pendant bubble (64)	4.66×10^{-6}	2840	-1.88
pendant drop - 2.5 μl	4.32×10^{-6}	3390	-2.26
pendant drop - 6.5 μl	4.51×10^{-6}	2720	-1.73

plotted versus the estimated C_{eq} values in Fig. 3.3(b). All of the data collapse onto a single curve. The best fit for the pendant bubble case is plotted for visualization purposes. The ability to collapse all of the data onto a single curve, along with the agreement between equilibrium surfactant transport parameters, validate the use of the modified Frumkin isotherm eq. 3.4.

3.5 Conclusions

Three pendant drop/bubble variations were used here to measure γ_{eq} for nonionic $C_{12}E_4$: pendant bubbles where $C_{12}E_4$ was in the continuous phase and $C_{eq} = C_i$, 6.5 μl pendant drops containing $C_{12}E_4$ suspended in air where $C_{eq} \neq C_i$ and 2.5 μl drops suspended in air where $C_{eq} \neq C_i$. Predictions were made using a global mass balance and Frumkin isotherm as to whether depletion would significantly affect γ_{eq} values. The effect of depletion on γ_{eq} was apparent in Fig. 3.3, yet fits of eqs 3.2 and 3.4 for all three cases yielded model constants Γ_∞, K_{eq} and Λ that were in excellent agreement. Thus it is possible to determine these model constants even when depletion is observed.

By eliminating the need for $C_{eq} = C_i$ to determine Γ_∞, K_{eq} and Λ, more freedom is given to designing pendant drop experiments, particularly when dealing with expensive or limited materials where small volumes would be desired. Additionally the analysis provides a robust tool for predicting when depletion will be significant and to what degree. This will be helpful

in designing and characterising many small-scale interfacial fluid dynamics problems such as in microfluidics devices where drop volumes can be $O(10^2)$ nl and smaller and A_s/V ratios could approach $O(10^4)$ m^{-1} and larger.

In the future other adsorption models such as the reorientation model, which has been shown to be better suited for larger ethylene glycol ethers (74) and some polyethylene glycol octylphenyl ethers (Triton X's) (46), could incorporate the same mass balance used here to account for depletion. Additionally for adsorption-limited transient surface tension experiments, transient adsorption models (64) could incorporate this mass balance to better predict adsorption and desorption rate constants in the presence of bulk depletion.

CHAPTER 4. ESTIMATING SURFACTANT SORPTION KINETICS

4.1 Introduction

In chapters 2 and 3 three parameters describing how *equilibrium* surface tension values γ_{eq} vary with the initial bulk surfactant concentration C_i were determined. These are: the maximum surface concentration of surfactant assuming a monolayer, Γ_∞; the surface-bulk distribution coefficient, K_{eq}; and the Frumkin interaction parameter, Λ. These are generally sufficient in describing surfactant adsorption to stationary fluid surfaces in equilibrium.

Aside from the special case of a stationary surface in equilibrium, additional information will be required to satisfactorily describe how surfactant accumulates at a surface separating two immiscible fluids. For example, consider a drop containing surfactant translating in another liquid. Besides surfactant adsorption to the surface, additional transport processes such as desorption, surface convection and diffusion, and bulk convection and diffusion can affect local surface concentrations of surfactant. Correctly modeling such a problem requires an understanding of both the surfactant adsorption and desorption processes.

Correctly accounting for the adsorption and desorption processes necessitates the determination of both an adsorption rate coefficient β and a desorption rate coefficient α. Since transient surface tension values are indicative of surfactant accumulating on the surface over time, they can be fit to adsorption-desorption models to determine these adsorption and desorption rates (45; 76; 77; 78; 79). In this chapter an adsorption-desorption model similar to the one used in the aforementioned references will be used. What will be unique about

the process outlined here is that the pattern search algorithm will be used to simultaneously determine the rate coefficients α and β. To do this Γ_∞ and Λ from fits of equilibrium surface tension values will be used.

In this chapter rate constants characterizing surfactant adsorption and desorption will be determined by examining the transient shapes of pendant drops and bubbles. Here pendant pendant drop experiments will have surfactant originating inside the drop phase while being insoluble in the continuous phase. Pendant bubble experiments will inversely have surfactant in the continuous phase. The experimental systems will be chosen so that depletion of surfactant in the bulk can be neglected based on the analysis in chapter 3. Furthermore the relevance of diffusion in the bulk on the surfactant accumulation process will be determined. The influence of diffusion will be considered by incorporating a finite volume model of Fick's 2^{nd} law inside the pendant drop or outside the pendant bubble. For systems deemed unaffected by diffusion, a concentration dependence on adsorption and desorption rate constants will be determined. This realized concentration dependence will be used to develop sorption models to be incorporated in the analysis for fluid dynamics problems in the following chapters.

In the next section a detailed description of the adsorption-desorption model used will be presented. This will be followed by a description of the methods used to determine the importance of bulk diffusion. Then the procedure for fitting the sorption model to transient surface tension data will be described followed by some results and discussion.

4.2 Analysis

4.2.1 *The adsorption-desorption model*

A commonly used model for surfactant adsorption and desorption at fluid-fluid interfaces is the Langmuir model (45),

$$\frac{\partial \Gamma}{\partial t} = \beta C_s(1-\theta) - \alpha\theta, \tag{4.1}$$

where C_s is the concentration of surfactant just below the surface. If both diffusion and depletion can be neglected then $C_s = C_i$. In this chapter we will only consider cases where depletion can be neglected. This means the bulk mass loss parameter $\zeta^* = \frac{\Gamma_\infty A_s}{C_i V}$ will be small according to chapter 3. Whether or not diffusion in the bulk can be neglected for certain surfactant systems will be determined later in this chapter.

In eq. 4.1 the the first term on the right-hand side describes the adsorption processes. The quantity $(1-\theta)$ represents the number of vacant adsorption sites left on the surface. The last term describes the desorption processes where θ by itself represents the number of filled adsorption sites on the surface. The adsorption and desorption rate coefficients β and α are not necessarily constant. It is common to assume these sorption rate coefficients follow an Arrhenius rate equation form like (45)

$$\beta = B\text{exp}\left(-\frac{E_\beta}{\hat{R}T}\right) \tag{4.2}$$

and

$$\alpha = A\text{exp}\left(-\frac{E_\alpha}{\hat{R}T}\right). \tag{4.3}$$

Above B and A are constants, and E_β and E_α are activation energies for adsorption and desorption, respectively. It has been shown that surfactants with long hydrocarbon chains exhibit non-ideal interactions that have an affect on the activation energies (45). If we assume the activation energies have a linear dependence on the surface coverage θ then $E_\beta = E_{\beta,0} + \nu_\beta\theta$ and $E_\alpha = E_{\alpha,0} + \nu_\alpha\theta$ where ν_β and ν_α are constants. Inserting eq. 4.2 and 4.3 with these linear dependencies into eq. 4.1 brings us to our generalized sorption model

$$\frac{d\Gamma}{dt} = \beta_0 e^{-\lambda_\beta \theta} C_s (1-\theta) - \alpha_0 e^{-\lambda_\alpha \theta} \theta \tag{4.4}$$

where the zero-coverage rate constants are $\beta_0 = B\exp\left(\frac{E_{\beta,0}}{\hat{R}T}\right)$ and $\alpha_0 = A\exp\left(\frac{E_{\alpha,0}}{\hat{R}T}\right)$, and the non-ideal interaction parameters for adsorption and desorption are $\lambda_\beta = \frac{\nu_\beta}{\hat{R}T}$, $\lambda_\alpha = \frac{\nu_\alpha}{\hat{R}T}$. For a surface in equilibrium (i.e. $\frac{d\Gamma}{dt} = 0$) eq. 4.4 reduces to the Frumkin isotherm from chapter 2 where $K_{eq} = \beta_0/\alpha_0$ and $\Lambda = \lambda_\alpha - \lambda_\beta$. It is typically assumed that the non-ideal interactions between surfactant molecules only affect the desorption process (36). In this case $\lambda_\beta = 0$ and $\lambda_\alpha = \Lambda$; we will use this assumption in our analysis and throughout this thesis.

4.2.2 *Bulk diffusion effects on sorption kinetics*

It is possible for diffusion in the bulk to play a significant role in surfactant accumulation on a surface. To predict whether or not diffusion may be significant we can consider relevant time scales for diffusion and adsorption. The diffusion time scale is generally the ratio of the square of the diffusion length scale ℓ_D and the diffusion coefficient D, or $\tau_D = \ell_d^2/D$. The adsorption or kinetic time scale comes from the analytical solution of eq. 4.4 when $\lambda_\beta = \lambda_\alpha = 0$ and is $\tau_k = \Gamma_\infty[\alpha_0(K_{eq}C_i + 1)]^{-1}$.

For spherical drops with radius b previous authors have analyzed these competing time scales when surfactant is outside the drop (79; 80). The relevant diffusion length scale for this situation is (80)

$$\ell_{D,out} = \left(\frac{3b^2\Gamma_{eq}}{C_i} + b^3\right)^{\frac{1}{3}} - b \tag{4.5}$$

and this length scale is likewise relevant to pendant bubble experiments when surfactant is in the continuous phase. The competing time scales when surfactant is inside a spherical drop has also been analyzed, but only for a case where depletion in the bulk will occur (73). In this situation the relevant length scale for diffusion becomes the radius of the drop b. When

surfactant is present inside the drop and depletion is not significant, the relevant diffusion length scale will be less than the radius.

To determine the diffusion length scale when surfactant is inside a spherical drop and depletion is not significant we follow a similar analysis as used in ref. (80). At equilibrium the amount of surfactant adsorbed to the surface is $4\pi b^2\Gamma_{eq}$. The diffusion length is then the distance normal to the surface one must travel in order to enclose an equivalent number of surfactant molecules in the bulk. The amount of surfactant enclosed in this volume is $C_{eq}\left[\frac{4}{3}\pi(b^3-(b-\ell_D))^3\right]$. Equating the two expressions and solving for ℓ_D gives the diffusion length scale,

$$\ell_{D,in} = b - \left(b^3 - \frac{3b^2\Gamma_{eq}}{C_i}\right)^{\frac{1}{3}}. \tag{4.6}$$

Note $C_{eq} = C_i$ because depletion is neglected. Using this length scale in estimating the diffusion time scale, the ratio of the diffusion and kinetic time scales can then help us predict whether or not diffusion will be significant. When surfactant originates outside the sphere

$$\tau_{D/k} = \frac{\alpha_0(K_{eq}C_i+1)}{D\Gamma_\infty}\left[\left(\frac{3b^2\Gamma_{eq}}{C_i}+b^3\right)^{\frac{1}{3}} - b\right]^2, \tag{4.7}$$

and when surfactant originates inside the sphere

$$\tau_{D/k} = \frac{\alpha_0(K_{eq}C_i+1)}{D\Gamma_\infty}\left[b - \left(b^3 - \frac{3b^2\Gamma_{eq}}{C_i}\right)^{\frac{1}{3}}\right]^2. \tag{4.8}$$

We can expect when $\tau_{D/k} \ll 1$ surfactant accumulation is adsorption-controlled, while when $\tau_{d/k} \gg 1$ it is diffusion controlled. When $\tau_{D/k}$ approaches O(1) both adsorption and diffusion would be important.

In addition to investigating the time scales, the surfactant accumulation process can be modelled to include diffusion. When adding diffusion to the model it is no longer assumed that $C_s = C_i$ and instead $C_s = f(t)$. Also the concentration inside the drop or outside the

bubble will no longer be assumed uniform and will instead be $C = f(r,t)$. Since the fluid is considered to be at rest mass transfer in the bulk is governed by Fick's second law of diffusion,

$$r^2 \frac{\partial C}{\partial t} = D \frac{\partial}{\partial r}\left(r^2 \frac{\partial C}{\partial r}\right). \tag{4.9}$$

We will make the assumption that the pendant drop or bubble can be approximated as a spherical drop with radius b. For the pendant bubble when surfactant is outside the sphere, two boundary conditions and the initial conditions are

$$C_{r\to\infty} = C_i \tag{4.10}$$

$$D\left(\frac{\partial C}{\partial r}\right)_{r=b} = \frac{d\Gamma}{dt}. \tag{4.11}$$

For the pendant drop when surfactant is inside the sphere,

$$\left(\frac{\partial C}{\partial r}\right)_{r=0} = 0 \tag{4.12}$$

$$D\left(\frac{\partial C}{\partial r}\right)_{r=b} = -\frac{d\Gamma}{dt}. \tag{4.13}$$

For both cases, the initial conditions are

$$C_{t=0} = C_i \tag{4.14}$$

$$\Gamma_{t=0} = 0. \tag{4.15}$$

A finite volume representation is used to solve these equations. For the case of surfactant being inside the drop, consider the approximately spherical drop to consist of I concentric

shells with thickness Δr bounded by r_i and r_{i+1}. For the case of surfactant being outside an approximately spherical bubble, consider instead I concentric shells outside the bubble with thickness Δr bounded by r_i and r_{i+1}. Multiplying eq. 4.9 by $4\pi dr$ and integrating from r_i to r_{i+1},

$$\int_{r_i}^{r_{i+1}} \frac{\partial C}{\partial t} 4\pi (r')^2 dr' = D \int_{r_i}^{r_{i+1}} \frac{\partial}{\partial r'} \left((r')^2 \frac{\partial C}{\partial r'} \right) 4\pi dr', \tag{4.16}$$

yields the result

$$C_i^{n+1} = \frac{4\pi D \Delta t}{V_i} \left[r_{i+1}^2 \left(\frac{C_{i+1}^n - C_i^n}{\Delta r} \right) - r_i^2 \left(\frac{C_i^n - C_{i-1}^n}{\Delta r} \right) \right] + C_i^n \tag{4.17}$$

where $V_i = \frac{4}{3}\pi(r_{i+1}^3 - r_i^3)$ is the volume of the i^{th} spherical shell and n is the time step. Additionally eq. 4.4 is discretized like

$$\Gamma^{n+1} = \Delta t \beta_0 C_s^n \left(1 - \frac{\Gamma^n}{\Gamma_\infty} \right) - \alpha_0 \frac{\Gamma^n}{\Gamma_\infty} e^{-\Lambda \Gamma^n / \Gamma_\infty} + \Gamma^n \tag{4.18}$$

where $C_s^n = C_I^n$ for surfactant inside the drop and $C_s^n = C_1^n$ for surfactant outside the bubble. Equation 4.18 is included in the boundary condition eq. 4.13. Essentially this finite volume model is used to estimate $C_s(t)$ which is simultaneously used in eq. 4.4.

4.2.3 *Fitting procedure*

The goal is to fit eq. 4.4 to sets of γ versus t for different surfactant systems and bulk concentrations. The fitting procedure is split into two parts: fitting without diffusion ($C_s = C_i$) and fitting with diffusion ($C_s = f(t)$). For either process, first the equilibrium fitting parameters Γ_∞ and Λ must be known. The surface-bulk distribution coefficient K_{eq} is not necessary. These parameters are determined by fitting the Frumkin isotherm and equation of state to sets of γ_{eq} versus C_i as in chapter 2.

Following the determination of Γ_∞ and Λ, eq. 4.4 is fit to sets of γ versus t by fixing $C_s = C_i$. The two unknowns are β_0 and α_0, and so a two-dimensional pattern search method as described in chapter 2 is used. Taking some initial guess for $\beta_{0,init}$ and $\alpha_{0,init}$, the pattern search stencil has initial widths $\Delta\beta_0 = 0.5\beta_{0,init}$ and $\Delta\alpha_0 = 0.5\alpha_{0,init}$. The adsorption-desorption model is solved with a simple forward Euler approximation of the time derivative. The first surface tension value at experimental time $t = 0$ is used to initialize the model. This is done using the Frumkin isotherm and equation of state along with the previously determined Γ_∞ and λ to determine the Γ that produces $\gamma(t = 0)$. Equation 4.4 is then solved up to a time just beyond the duration of the experiment. The ℓ^2-norm between the model and the experimental data set is used to define the objective function in the pattern search algorithm. A local minimum is established when both $\Delta\beta_{0,n} = 0.0001\beta_{0,n}$ and $\Delta\alpha_{0,n} = 0.0001\alpha_{0,n}$ where n is the current guess in the pattern search algorithm. The pattern search algorithm is reinitialized at this local minimum and iterates until another minimum is found. A final global minimum is established when successive local minimums result in equivalent β_0 and α_0.

After generating rate constants for each data set assuming $C_s = C_i$, the data are fit a second time allowing $C_s = f(t)$. The finite volume scheme outlined in the previous section is used to estimate $C_s(t)$. For a given time step the solution of the finite volume problem and the adsorption problem is performed as follows. Based on the current concentration just near the surface C_s^n, the new amount of surfactant on the surface Γ^{n+1} after the time step Δt is determined using eq. 4.18. Boundary condition eq. 4.11 or 4.13 is also applied based on C^n and Γ^n to determine C_s^{n+1}. Either boundary condition eq. 4.10 or 4.12 is used to get C_I^{n+1} or C_1^{n+1} for the cases of surfactant outside or inside the sphere, respectively. Then the interior concentrations C_i^{n+1} are determined from eq. 4.17. Based on Γ^{n+1}, Γ_∞ and Λ, γ^{n+1} is also determined.

The finite volume scheme is initialized with eqs. 4.14 and 4.15 and solved until a surface tension value equal to the first experimental value is reached. Then the equations are solved

up until a time just beyond the duration of the experiment. Again the ℓ^2-norm between the model and the experimental data set is used to define the objective function in the pattern search algorithm.

4.3 Experiments

Pendant drop experiments were used to capture transient surface tension data for several surfactant systems. Experiments were performed using the same setup from chapter 2 for pendant drops. The continuous phases for the pendant drop experiments were light mineral oil (Fisher Scientific) (ρ =830 kg m^{-3}), heavy mineral oil (Fisher Scientific) (ρ =900 kg m^{-3}), and 1000 cSt polydimethysiloxane oil (Si oil) (Clearco) (ρ =980 kg m^{-3}). The drop phases of the pendant drop experiments were aqueous solutions of either >99% sodium dodecyl sulfate (SDS) (Fisher Scientific), >97% sodium oleate (SO) (TCI), or >99% hexadecyltrimethylammonium bromide (CTAB) (Acros). The SDS and SO surfactants are anionic while CTAB is cationic. The surfactant concentrations used were as high as the approximate critical micelle concentration (CMC) (57) and lower. In addition to the pendant drop experiments, one pendant bubble system was included for comparison. The setup for these experiments was the same as in chapter 3. The bubble phase was air (ρ =1.2 kg m^{-3}) and the continuous phase was an aqueous mixture of >98% tetraethylene glycol monododecyl ether ($C_{12}E_4$) (Sigma-Aldrich), a non-ionic surfactant.

Images of pendant bubbles and drops were taken over time and their change in shape was analyzed to determine the change in surface tension over time. The in-house program from chapters 2 and 3 was used. Intervals between images were between 2 and 600 s depending on the system under investigation. Drop volumes ranged from 5 to 50 μl again depending on the system. The images were captured until an approximate equilibrium in surface tension was reached, resulting in experiments that lasted as short as 5 minutes for $SO_{(aq)}$ - light mineral oil and as long as 15 hours for $CTAB_{(aq)}$ - heavy mineral oil. The resulting transient surface tension data was fit using the models described above.

4.4 Results

Before fitting the adsorption-desorption model to transient surface tension data, the equilibrium fitting parameters must be determined. For $SDS_{(aq)}$ and $SO_{(aq)}$ in light mineral oil this has been done already in chapter 2 and the fitting parameters are repeated in Table 4.1 for convenience. For the other surfactant systems used here equilibrium surface tension values are reported in Fig. 4.1 and fit with the Frumkin isotherm and equation of state using the same procedure from chapter 2. The clean surface tension values used are 72.2 mN m^{-1} for $C_{12}E_{4(aq)}$ - air, 55 mN m^{-1} for $SDS_{(aq)}$ and $CTAB_{(aq)}$ - heavy mineral oil, and 25 mN m^{-1} for $SDS_{(aq)}$ - 1000 cSt Si oil. The surface tensions near the CMC are as low as 4 mN m^{-1} for $SDS_{(aq)}$ - 1000 cSt Si oil and as high as 33 mN m^{-1} for $C_{12}E_{4(aq)}$ - air. In Fig. 4.1 the solid lines are best fits of the Frumkin isotherm and equation of state. The resulting fitting parameters Γ_∞, K_{eq} and Λ are presented in Table 4.1.

The SDS values for Γ_∞ and K_{eq} decrease slightly as the continuous phase changes from light mineral oil to heavy mineral oil to 1000 cSt Si oil. Since the SDS molecule is not changing size, this can potentially be interpreted as less room being available on the surface when moving from mineral oil to Si oil, perhaps due to the increasing size of the molecules in the continuous phase. Still net repulsive interactions between the SDS molecules are predicted based on values of Λ for each continuous phase. The fits of SO and CTAB on the other hand generate positive Λ indicating net attraction between surfactant molecules. The impact of this on fluid dynamics will be investigated in chapter 5 for SO.

Plots of γ versus t for the different surfactant systems with different bulk concentration are shown in Figs. 4.2, 4.3 and 4.4. Note that not every experiment is shown for the sake of clarity. The six systems show a range of surface tension values and times required to reach γ_{eq}. The SDS and SO systems take between 50 and 300 s to reach equilibrium, whereas the $C_{12}E_4$ experiments take up to 2 hours and CTAB experiments as long as 15 hours.

The solid lines in Figs. 4.2, 4.3 and 4.4 are best fits of eq. 4.4 neglecting diffusion i.e. $C_s = C_i$. The adsorption-desorption model fits well visually to the experimental data with

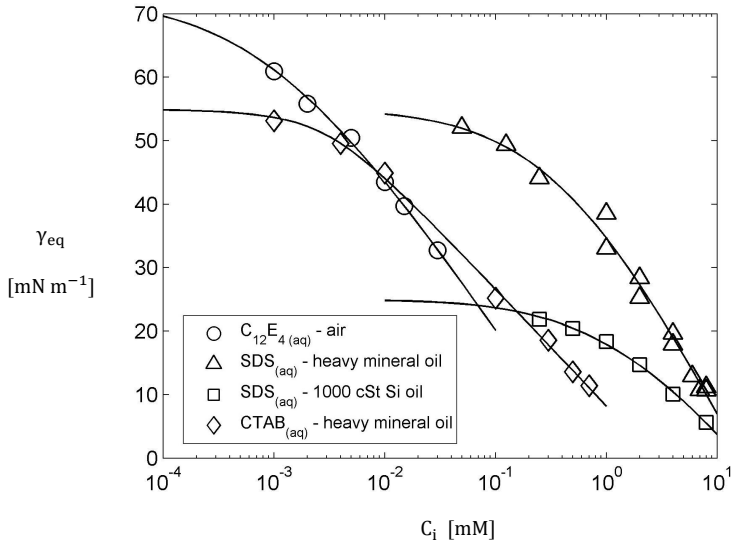

Figure 4.1 *Plots of γ_{eq} versus C_i for $SDS_{(aq)}$ in heavy mineral oil and 1000 cSt Si oil, $CTAB_{(aq)}$ in heavy mineral oil and $C_{12}E_{4(aq)}$ in air. The solid lines are best fits of the Frumkin isotherm and equation of state.*

Table 4.1 *Model constants corresponding to best fits of the Frumkin isotherm and equation of state as shown in Fig. 4.1.*

	Γ_∞ mol m^{-2}	K_{eq} m^3 mol^{-1}	Λ –
$SDS_{(aq)}$ - light mineral oil	3.84×10^{-6}	10.6	-3.88
$SDS_{(aq)}$ - heavy mineral oil	2.89×10^{-6}	7.25	-1.48
$SDS_{(aq)}$ - 1000 cSt Si oil	2.06×10^{-6}	1.53	-1.89
$SO_{(aq)}$ - light mineral oil	3.89×10^{-6}	2.16	3.21
$C_{12}E_{4(aq)}$ - air	4.40×10^{-6}	2920	-1.88
$CTAB_{(aq)}$ - heavy mineral oil	1.62×10^{-6}	161	1.47

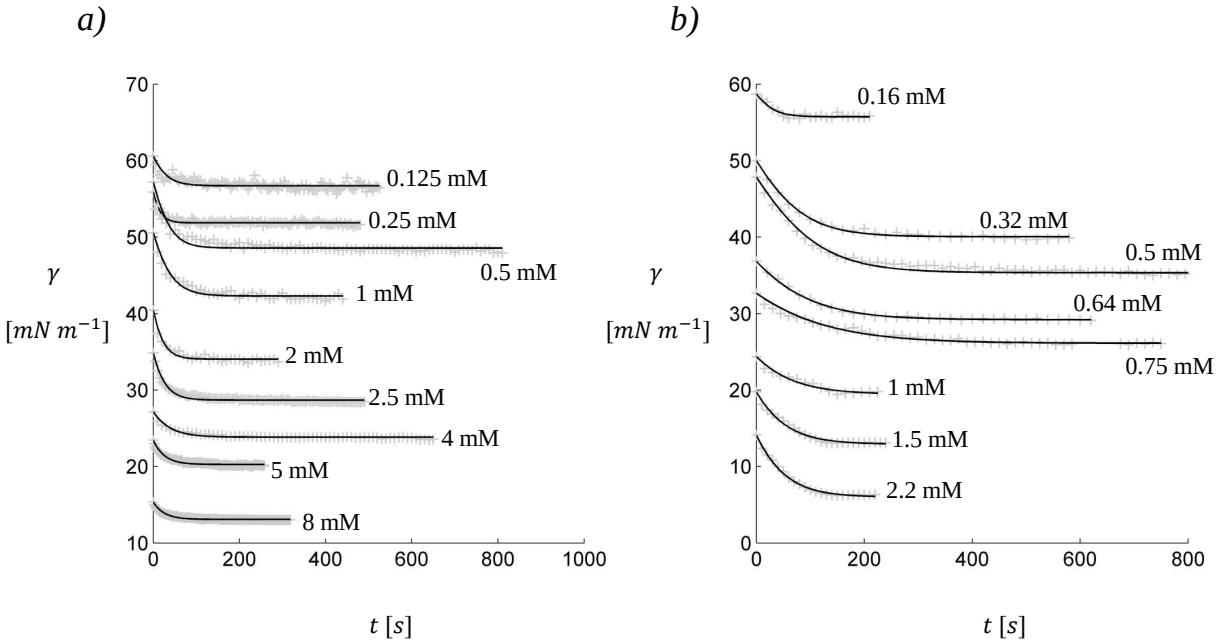

Figure 4.2 *Plots of γ vs t for a) $SDS_{(aq)}$ and b) $SO_{(aq)}$ pendant drops suspended in light mineral oil. The surfactant concentrations corresponding to each set of data is shown. The $+'s$ represent individual surface tension values determined from a single image and the solid black lines are best fits of eq. 4.4 neglecting diffusion ($C_s = C_i$).*

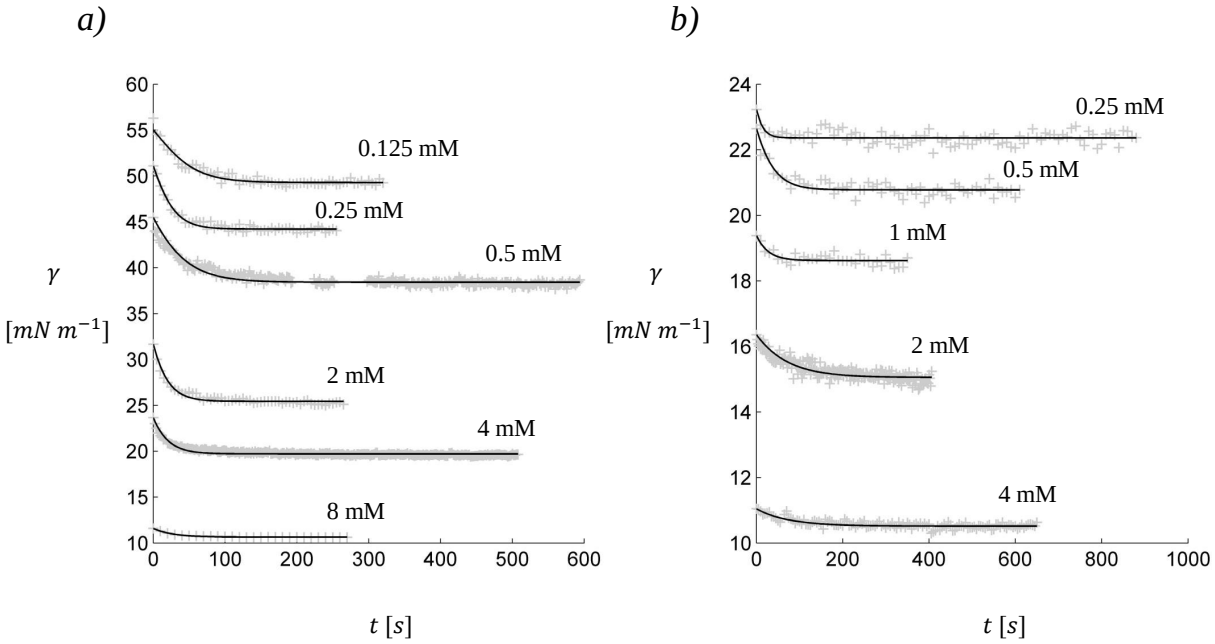

Figure 4.3 *Plots of γ vs t for a) $SDS_{(aq)}$ drops suspended in heavy mineral oil and b) $SDS_{(aq)}$ drops suspended in 1000 cSt Si oil. The surfactant concentrations corresponding to each set of data is shown. The $+'s$ represent individual surface tension values determined from a single image and the solid black lines are best fits of eq. 4.4 neglecting diffusion ($C_s = C_i$).*

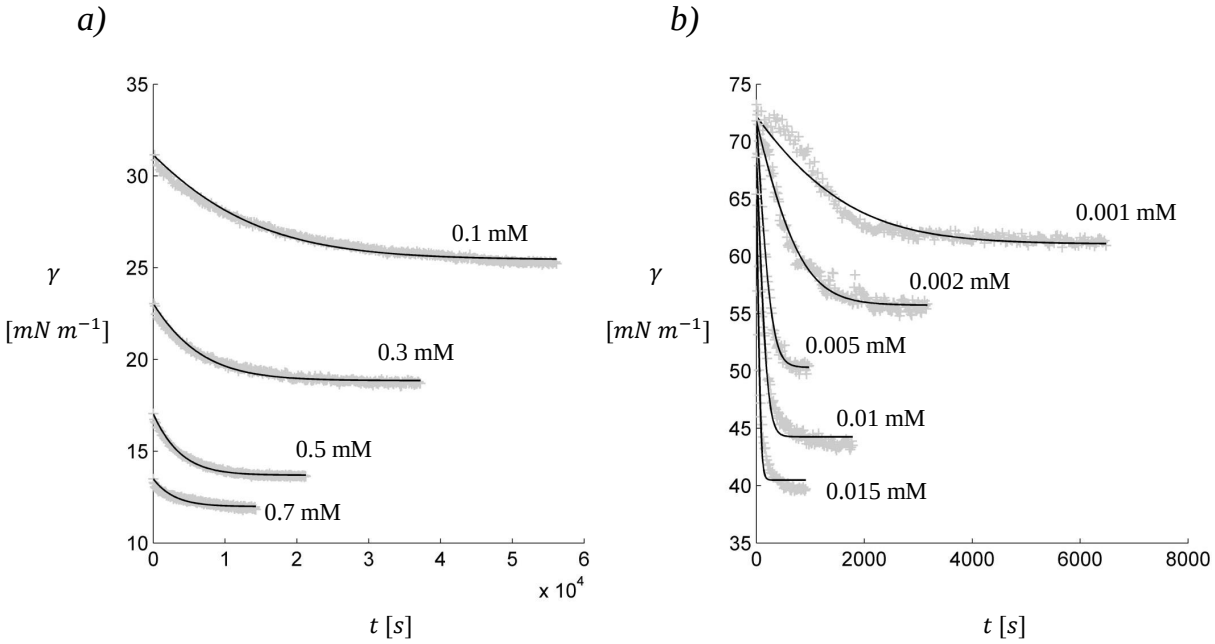

Figure 4.4 *Plots of γ vs t for a) $CTAB_{(aq)}$ drops suspended in heavy mineral oil and b) air bubbles in $C_{12}E_{4(aq)}$. The surfactant concentrations corresponding to each set of data is shown. The $+'s$ represent individual surface tension values determined from a single image and the solid black lines are best fits of eq. 4.4 neglecting diffusion ($C_s = C_i$).*

Table 4.2 *Comparisons between K_{eq} from fits of the Frumkin isotherm and equation of state to γ_{eq} data and the ratio β_0/α_0 from fits of eq. 4.4 to transient surface tension data when $C_s = C_i$. The mean of the ratio β_0/α_0 for a given system,* mean $\left(\frac{\beta_0}{\alpha_0}\right)$*, and the corresponding standard deviation,* std $\left(\frac{\beta_0}{\alpha_0}\right)$*, is shown.*

	K_{eq} $m^3\ mol^{-1}$	mean $\left(\frac{\beta_0}{\alpha_0}\right)$ $m^3\ mol^{-1}$	std $\left(\frac{\beta_0}{\alpha_0}\right)$ $m^3\ mol^{-1}$
$SDS_{(aq)}$ - light mineral oil	10.6	10.40	1.13
$SDS_{(aq)}$ - heavy mineral oil	7.25	7.00	2.49
$SDS_{(aq)}$ - 1000 cSt Si oil	1.53	1.40	0.08
$SO_{(aq)}$ - light mineral oil	2.16	1.87	0.11
$C_{12}E_{4(aq)}$ - air	2920	2860	311
$CTAB_{(aq)}$ - heavy mineral oil	161	153	21.8

the exception of the $C_{12}E_{4(aq)}$ - air data set. The inability to fit eq. 4.4 with $C_s = C_i$ to the $C_{12}E_{4(aq)}$ - air experiments is likely because diffusion effects are significant with this system as will be discussed later.

The adsorption rate constants β_0 and desorption rate constants α_0 used to generate the fits in Figs. 4.2, 4.3 and 4.4 are plotted versus C_i in Fig. 4.5. For a particular system the rate constants can span up two orders of magnitude, and overall the rates constants span several orders of magnitude. Interestingly the rate constants all decrease with increasing C_i except for $C_{12}E_{4(aq)}$ - air, but again the fits for that particular system are relatively poor.

Since β_0 and α_0 were determined simultaneously it is important to check the ratio β_0/α_0. At equilibrium the adsorption-desorption model reduces to the Frumkin isotherm where $K_{eq} = \beta_0/\alpha_0$, so this relationship must hold for the values shown in Fig. 4.5. The mean of the ratio β_0/α_0 for each system studied, mean $\left(\frac{\beta_0}{\alpha_0}\right)$, as well as the corresponding standard deviation std $\left(\frac{\beta_0}{\alpha_0}\right)$ is presented in Table 4.2. The ratios β_0/α_0 are in very good agreement with the surface-bulk distribution parameters K_{eq} determined from fits of equilibrium surface tension data.

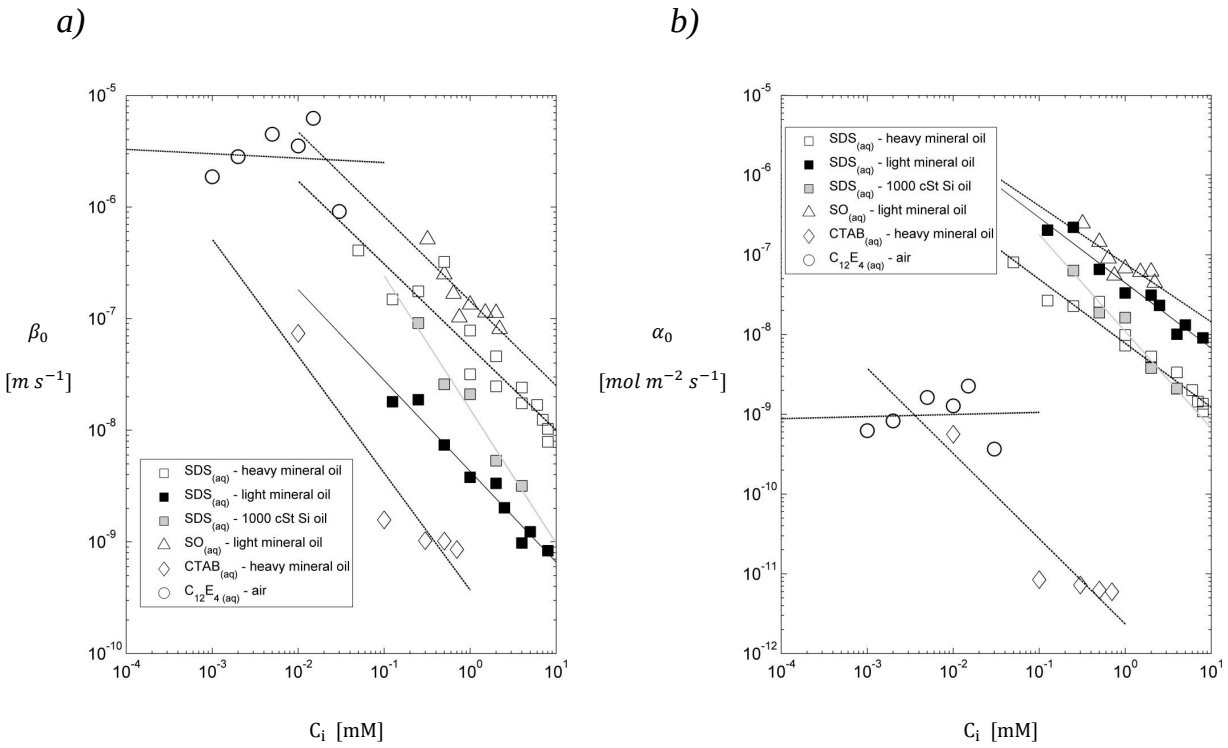

Figure 4.5 *The a) adsorption rate constants β_0 and b) desorption rate constants α_0 corresponding to the fits of eq. 4.4 shown in Fig. 4.2, 4.3 and 4.4 are plotted versus C_i. Solid lines are linear best fits on the log-log scale.*

As discussed earlier it is necessary to determine if diffusion is relevant and if the assumption $C_s = C_i$ is valid. We will first use eq. 4.7 or 4.8 to determine the order of magnitude of $\tau_{D/k}$ for each system for different C_i. This ratio of diffusion and adsorption time scales requires several parameters, some of which can be difficult to determine. Values for D are not known for the systems used here, but a value of $1{\times}10^{-10}$ m^2 s^{-1} is chosen as a conservative value based on others reported in the literature (80). Values for K_{eq} and Γ_∞ come from Table 4.1 and values for Γ_{eq} come from best fits of the Frumkin equation of state and isotherm. Estimates for α_0 come from Fig. 4.5. The values used for α_0 are $1{\times}10^{-7}$ mol m^{-2} s^{-1} for each SDS system, $1{\times}10^{-10}$ mol m^{-2} s^{-1} for the CTAB$_{(aq)}$ - heavy mineral oil system, and $1{\times}10^{-9}$ mol m^{-2} s^{-1} for the $C_{12}E_{4(aq)}$ - air system. Based on the volumes of the pendant drops and bubbles, the radii for equivalent spheres range from about 1 to 2 mm; for the purposes of estimating the order of magnitude of $\tau_{D/k}$ a fixed value of b =1.5 mm is used.

In Fig. 4.6 estimates of $\tau_{D/k}$ are plotted versus C_i. First it is clearly expected that $C_{12}E_{4(aq)}$ - air will be affected by diffusion as estimates of $\tau_{D/k}$ are O(10-100). This prediction agrees with other studies where similar surfactant systems were used (64; 78; 79). It also explains the relatively poor fits in Fig. 4.4(b).

Each of the SDS and SO systems have $\tau_{D/k}$ O(0.1) or less, with the SO$_{(aq)}$ - 1000 cSt Si oil $tau_{D/k}$ being O(0.001) and lower. In these systems it might be expected that diffusion plays a less significant role and the assumption $C_s = C_i$ may be valid at least for higher C_i. The CTAB$_{(aq)}$ - heavy mineral oil system has a $\tau_{D/k}$ O(0.001-0.01) at higher C_i, but just below C_i =0.01 mM it approaches O(1). For this surfactant diffusion may become significant at these lower concentrations.

To better determine if diffusion can be neglected, the pendant drop and bubble systems are modeled using eq. 4.4 where $C_s = f(t)$. The finite volume method outlined earlier is used to estimate $C_s(t)$ and $D = 1 \times 10^{-10}$ m^2 s^{-1} is used. The same $D = 1 \times 10^{-10}$ m^2 s^{-1} used in the analysis of time scales is used in the finite volume model. The adsorption rate

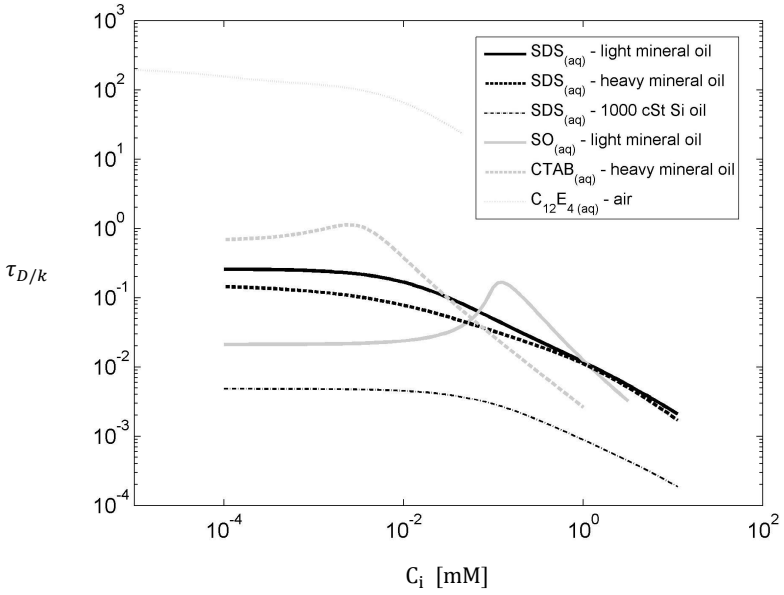

Figure 4.6 *Estimates of the ratio of diffusion to adsorption time scales $\tau_{D/k}$ are plotted versus C_i.*

constants determined by including bulk diffusion, $\beta_{0,\text{diff}}$, are compared to those determined when $C_s = C_i$ in Fig. 4.7. Similar differences are found for the desorption rates.

Above $C_i = 1$ mM adding diffusion changes the adsorption rate constants by less than about 10% for each of the SDS, SO and CTAB systems. Below 1 mM the adsorption rate constants differ by 20-80% for $\text{SDS}_{(aq)}$ - light and heavy mineral oil and $\text{SO}_{(aq)}$ - light mineral oil. The CTAB system does not see much difference when adding diffusion until around 0.01 mM where a difference of about 40% is observed. In general increasing C_i decreases the effect of adding diffusion to the model.

As mentioned earlier the $\text{C}_{12}\text{E}_{4(aq)}$ - air system is expected to be impacted by diffusion or even diffusion-controlled. A single comparison between adsorption rate constants determined with and without diffusion is shown in Fig. 4.7 at $C_i = 0.03$ mM which is approximately the CMC. At this concentration there is already a more than 200% difference in rate constants when adding diffusion. Fits of lower concentrations were unsuccessful because those systems

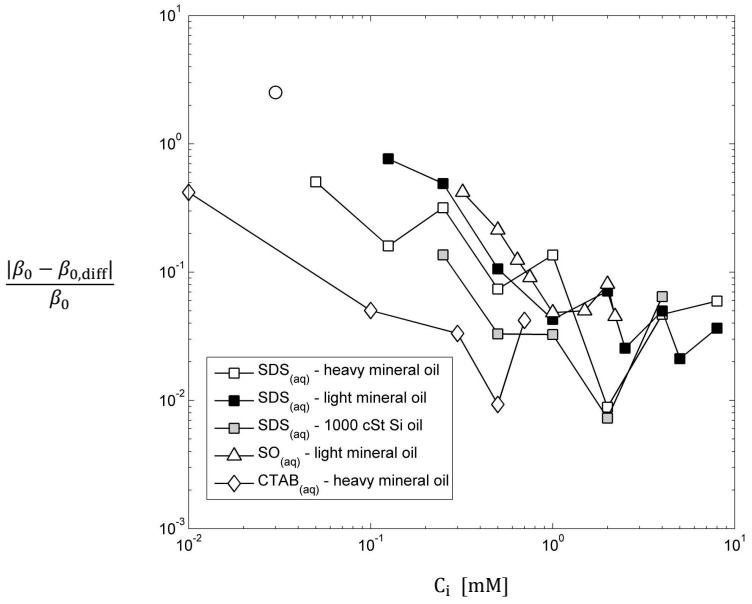

Figure 4.7 *The relative difference between adsorption rate constants when $C_s = C_i$ and when $C_s = f(t)$ are shown versus C_i.*

are likely diffusion-controlled. The diffusion time scales are so much larger than the adsorption time scales that changing $\beta_{0,\text{diff}}$ and $\alpha_{0,\text{diff}}$ essentially does not affect how γ changes with time, making it very difficult to determine $\beta_{0,\text{diff}}$ and $\alpha_{0,\text{diff}}$.

4.5 Discussion

In this chapter adsorption and desorption rate constants characterizing the transient surfactant accumulation process was sought. This was done by fitting an adsorption-desorption model eq. 4.4 along with the Frumkin isotherm and equation of state to transient surface tension data generated from pendant drops and bubbles. In order for the resulting fitting parameters β_0 and α_0 to be acceptable, the concentration of surfactant in the bulk phase had to remain constant and uniform. This means depletion in the bulk had to be limited and diffusion in the bulk had to be insignificant relative to the adsorption and desorption

processes. To prevent depletion, the analysis from chapter 3 was considered. The bulk mass loss parameters ζ^* were kept low enough to consider depletion negligible.

To determine if diffusion could be neglected and C_s would remain roughly constant the competing diffusion and adsorption time scales were analyzed. Additionally a finite volume method was incorporated into the adsorption-desorption model to estimate $C_s(t)$ and determine diffusion's impact on β_0 and α_0. While exact values for the diffusion coefficient D were not known, a conservative value based on similar values in the literature was used. Based on an analysis of the time scales, the $C_{12}E_{4(aq)}$ - air system was expected to be significantly affected by diffusion, and this was confirmed when comparing fits of eq. 4.4 when diffusion was incorporated. Thus the β_0 and α_0 in Fig. 4.5 should not be considered indicative of the adsorption and desorption rates in the $C_{12}E_{4(aq)}$ - air system.

The $CTAB_{(aq)}$ - heavy mineral oil system was expected to be potentially affected by diffusion only at lower concentrations based on the ratio of diffusion and adsorption time scales. This is backed up by a comparison of β_0 with and without diffusion. At concentrations $C_i > 0.1$ mM diffusion affected β_0 by less than 10%. At 0.01 mM the difference increased to almost 40%. The lower concentrations were not considered because a sufficient number of transient surface tension data points were not collected to fit eq. 4.4; instead only equilibrium values are presented for these concentrations in Fig. 4.1. It is also of note that adsorption and desorption rates were considerably smaller for $CTAB_{(aq)}$ - heavy mineral oil than any of the other systems studied in this chapter. This would make this surfactant difficult to study in experimental fluid dynamics problems due to its slow sorption kinetics.

The three $SDS_{(aq)}$ systems and the $SO_{(aq)}$ - light mineral oil system were not expected to be greatly affected by diffusion based on the analysis of time scales. The effect of adding diffusion on the determination of β_0 for these systems in shown in Fig. 4.7. At concentrations above 1 mM the differences in β_0 with and without diffusion were less than 10% using a conservative guess for the diffusion coefficient. Decreasing C_i increased this difference which approached 100% at low 0.1 mM and below. This however is a very conservative analysis

considering the diffusion coefficient used and likely overestimates the impact of diffusion. Therefore for the purposes of estimating β_0 and α_0 we will consider diffusion nearly negligible down to about 0.1 mM for these systems and $C_s = C_i$.

Continuing to consider the $SDS_{(aq)}$ systems and the $SO_{(aq)}$ - light mineral oil system, the rate constants in Fig. 4.5 appear to scale with C_i to some constant power m. Additionally the power m appears to be similar for both α_0 and β_0. It is then proposed that the adsorption-desorption model eq. 4.4 could be modified to

$$\frac{d\Gamma}{dt} = \hat{\beta}_0 C_i^{1+m}(1-\theta) - \hat{\alpha}_0 C_i^m e^{-\Lambda\theta}\theta \tag{4.19}$$

where $\hat{\beta}_0$ and $\hat{\alpha}_0$ are interpreted as the adsorption and desorption rate constants at $C_i = 1$ mM. Importantly when $d\Gamma/dt \to 0$ eq. 4.19 still reduces to the Frumkin isotherm, making this a valid adsorption-desorption model to use with the Frumkin isotherm and equation of state. This concentration dependence allows us to develop a single model describing surfactant adsorption for a particular surfactant system. For the three $SDS_{(aq)}$ systems and the $SO_{(aq)}$ - light mineral oil system, the constants $\hat{\beta}_0$, $\hat{\alpha}_0$ and m to be used in eq. 4.19 based on the linear fits in Fig. 4.5 are shown in Table 4.3. Due to powers m units are not explicitly given in the table, but the quantities $\hat{\beta}_0 C_i^{1+m}$ and $\hat{\alpha}_0 C_i^m$ both have units mol m^{-2} s^{-1}. These single models describing how adsorption and desorption rates change with C_i, along with the parameters Γ_∞ and Λ taken from previous fits of γ_{eq} versus C_i, can be used in the analysis of interfacial fluid dynamics problems.

4.6 Conclusions

In this chapter adsorption-desorption models for several surfactant systems were determined. The systems for which models were developed involved surfactant that was soluble in one phase and insoluble in the other. Depletion in the bulk surfactant concentration was neglected, and models were only developed for systems where bulk diffusion could be

Table 4.3 *The model constants $\hat{\beta}_0$, $\hat{\alpha}_0$ and m for the three $SDS_{(aq)}$ systems and the $SO_{(aq)}$ - light mineral oil system corresponding to eq. 4.19 are shown. Note these constants do have units, but units are not shown due to the powers m.*

	$\hat{\beta}_0$	$\hat{\alpha}_0$	m
$SDS_{(aq)}$ - light mineral oil	4.45×10^{-8}	4.29×10^{-9}	-0.82
$SDS_{(aq)}$ - heavy mineral oil	5.21×10^{-8}	7.70×10^{-9}	-0.77
$SDS_{(aq)}$ - 1000 cSt Si oil	1.53×10^{-8}	1.10×10^{-8}	-1.21
$SO_{(aq)}$ - light mineral oil	1.43×10^{-7}	7.69×10^{-8}	-0.74

neglected. The model constants came from fitting transient surface tension data collected using the pendant drop or bubble method.

A diffusion length scale for the case of surfactant residing inside a spherical drop was established and the ratio of diffusion and adsorption time scales was used as a first indication of the ability to neglect diffusion in the bulk. Transient surface tension data was subsequently fit while incorporating a finite volume model to account for diffusion. For certain models rate constants were not significantly affected by the inclusion of diffusion, supporting the assumption that diffusion is negligible for those cases.

In systems where diffusion was neglected, the rate constants were found to be dependent on the bulk concentration. The Langmuir-Frumkin adsorption-desorption model was modified with the new fitting parameter m to reflect this concentration dependence. Using the modified adsorption-desorption model, a single set of five constants can describe adsorption for a given surfactant system with a given bulk concentration as long as bulk depletion and diffusion can be neglected. These five constants are the maximum surface concentration ,Γ_∞, the Frumkin interaction parameter ,Λ, the adsorption and desorption rate constants for $C_i = 1$ mM, $\hat{\beta}_0$ and $\hat{\alpha}_0$, and the new exponent, m. These models can be incorporated into the analyses of fluid dynamics problems involving surfactants.

CHAPTER 5. MARANGONI STRESS INDUCED FILM THICKENING AND TAIL-STREAMING OF SURFACTANT-LADEN DROPS IN A HORIZONTAL ROTATING CYLINDER

Modified from a paper submitted to *Phys. Rev. Fluids*

Andrew R. White[1], Azeez Odesanya[2], Caroline Periera[2], Thomas Ward[3]

Department of Aerospace Engineering, Iowa State University, Ames, IA 50011

5.1 Introduction

In this chapter we study, through experiment and computation, the effect of an anionic surfactant, either sodium dodecyl sulfate (SDS) or sodium oleate (SO), on the equilibrium oil film thickness between aqueous drops and a rotating horizontal cylindrical tank wall. The experimental setup consists of a rotating horizontal tank (81) of radius R half-filled with light mineral oil. Drop volumes, V_d, were small such that locally the tank wall relative to the drop interface may be considered nearly flat i.e. $[3V_d/(4\pi)]^{1/3}/R \ll 1$. As the tank steadily rotates with rate ω a visible thin liquid film forms between the tank wall and the drop interface which we measure. The range of surfactant concentrations spanned from just above the minimum concentration where the surface tension is lowered to just below the bulk critical micellar concentration (CMC) denoted c_∞ (mol m^{-3}). For the SO surfactant near the

[1]Primary researcher and author

[2]Undergraduate student researcher

[3]Corresponding author. E-mail: thomasw@iastate.edu

CMC we observe considerable stretching of the drop that results in tail-streaming indicating saturation of the local interface with surfactant. However this observation does not occur for all rotation rates suggesting transport of surfactant to the drops rear is key to understanding this behavior. To estimate the local surface coverage of surfactant we use the coupled species conservation and and two-dimensional thin film equations (4; 25; 82; 83; 84; 85; 86) with surfactant transport (27; 38; 41; 87; 88; 89; 90) and kinetics based on the well known Frumkin isotherm (60; 61). To confirm the validity of the numerical data we compare those results with the minimum film thickness, h_{min}, as a function of the capillary number, Ca^* (25).

Accurate predictions of surface coverage is vital to understanding the observed surfactant transport and subsequent physico-chemical phenomena. Therefore in this chapter we stress the importance of utilizing an appropriate isotherm and associated equation of state for a given surfactant and range of concentrations. Measurement of equilibrium surfactant transport and transient kinetic parameters for each surfactant were performed in chapters 2 and 4. Here we demonstrate that measurement of these parameters based on the Frumkin isotherm (60; 61) is suitable for the study of transport of real surfactants. To date there have been numerous computational studies on surfactant effects at moving interfaces such as drops and bubbles (36; 91; 92; 93) and thin films (38; 39; 40; 41). Many of these studies use either a linearized or Langmuir isotherm and associated equation of state to describe the relationship between surface concentration, Γ, and surface tension, γ (58; 59). While these equations may be accurate for surfactant concentrations well below the CMC they clearly cannot provide meaningful results for all situations. In particular the Langmuir isotherm and equation of state can yield a false physical result of complete surface coverage as the bulk surfactant concentration approaches the CMC (92).

The Frumkin isotherm and equation of state remedy these shortcomings through a complete description of surfactant behavior, as measured through surfactant transport parameters. These parameters are the surface-bulk distribution coefficient K_{eq}, the maximum surface surfactant concentration assuming a monolayer, Γ_∞, and a nonlinear molecular in-

teraction parameter Λ. The molecular interaction parameter separates the Frumkin isotherm from the Langmuir isotherm where a positive Λ suggests net attraction between molecules and a negative Λ indicates net repulsion. Adding more surfactant to the bulk does not necessarily enhance the surface concentration for negative Λ surfactants. Meanwhile for surfactants with positive Λ and hence more efficient surface packing it is possible to nearly reach complete surface coverage well before the bulk concentration is at the CMC. These two types of surfactants are represented in the SDS and SO systems studied here where different behavior is observed as the bulk concentration approaches the CMC, denoted C_∞, for nearly equivalent Ca^* when it is based on the clean ($\Gamma = 0$) surface tension. This would suggest that the capillary numbers based on the clean surface tension may not be useful in characterizing any contrasting behavior observed between the two surfactant systems. So we use computation to estimate the minimum surface tension (maximum surface concentration) and update its value.

The experimental system, consisting of a drop in a rotating horizontal cylindrical tank that is half-filled with oil, is modeled as a bounded two-dimensional stationary interface parallel to a moving planar wall. Unfortunately, the horizontal tank setup used here does not allow the study of long drops or bubbles without the need to consider curvature of the tank. It does however allow the visualization of a stationary drop adjacent to a moving wall. To compare the experiments and numerical data we introduce a method to model the thin film region of oil between a finite length drop and the tank wall. The method consists of performing a partial lubrication analysis of the governing equations.

The lubrication approximation is applied to the momentum equations yielding the typically parabolic velocity profile. Then, instead of using the approximation to also eliminate $O[(dh/dx)^2]$ terms in the film evolution and species conservation equations most of the terms are retained. Including these additional terms allows one to impose boundary conditions that accurately represent those seen in the experiments. The conditions include precise specification of the curvature $\kappa = f(dh/dx, d^2/dx^2)$ at the leading edge of the drop, removing the

need to specify the film thickness *a priori*. At the trailing edge the curvature is constant with an interface height set equal to the unspecified leading edge value. Along with plots of film profiles the data presentation includes an interface velocity profile analysis which shows the production of stagnation points. We classify these stagnation points and relate their type to some of the experimental observations.

In the next section the thin film and species conservation equations are discussed. This is followed by a brief overview of the solution method that required solving simultaneously the transient film evolution and species conservation equations until an equilibrium film and concentration profile were reached. Details on the numerical methods will be included in the paper submitted to *Phys. Rev. Fluids*. The experimental setup, material and procedure then follow. This section includes some particle image velocimetry measurements made in the horizontal rotating tank. Pendant drop data was used to estimate the surface coverage for the SO and SDS where it was determined that they generate complete and partial surface coverage at the CMC, respectively. The numerical and experimental results for film thickness and profiles were compared with good agreement between them. The chapter concludes with a summary and some possible direction for future work.

5.2 Theory and analysis: lubrication approximation

5.2.1 *Theory*

Consider a horizontal right-cylindrical tank partially filled with a viscous oil. Subscripts in this chapter for fluid properties such as the density ρ_i and dynamic viscosity μ_i are denoted as dispersed ($i = 1$) or continuous ($i = 2$). The cylinder rotates counterclockwise about its symmetric axis with angular velocity ω and wall velocity $U = \omega R$ where R is the tank radius. An aqueous drop that contains a surfactant with bulk concentration C_0, volume V_d, and volume-equivalent spherical radius $b = [3V_d/(4\pi)]^{1/3}$ with $b/R \ll 1$ is inserted into the oil phase. The surfactant surface concentration and surface tension between the two phases

are denoted Γ and γ. After some time the drop is located at the equilibrium angular position ϕ measured counterclockwise from the tank vertcial symmetry plane. The cross section for the drop local horizontal and vertical coordinate system is denoted x_L and y_L, respectively. Due to shear and Marangoni stresses the drop stretches to a measured length L_γ relative to the measured length of the drop under the same conditions (capillary number) with no surfactant in the bulk, L_0.

Now consider the viscous thin film of fluid separating the fluid-fluid interface from the wall as a two-dimensional interface. The thin film region begins at the distance $x_{0,exp}$ measured from the drops leading edge $x_L = 0$ and has the minimum thickness denoted h_{min} (see Fig. 5.1). The local thin film coordinate system is denoted using the x and y where $x = x_l - x_{0,exp}$ and $y = y_L$ such that $y = 0$ and $y = h(x)$ are the wall and thin film location, respectively. Since the viscosity of the thin film is much larger than that of the drop phase we mathematically treat it as inviscid so that the velocity, $\boldsymbol{v}_1$, and pressure, P_1, are both zero.

In the following analysis the transport of surfactant to the interface is due to sorption kinetics i.e. the interface transport is *sorption controlled*, also called the insoluble surfactant limit (36; 88; 90; 91; 92). This simplifies the problem since mass transport from the bulk may be neglected. The simplification also means the proposed system is analogous to one with the surfactant in the continuous thin film phase. The sorption controlled surface transport assumption is valid when depletion of surfactant from the bulk drop phase is negligible and discussed in chapter 3 and when diffusion can be neglected as discussed in chapter 4.

5.2.2 *Momentum equation*

In the stationary frame of reference the wall velocity relative to the equilibrium position of the drop can be written as U. The sorption (both adsorption and desorption) of surfactant to the interface can cause gradients in the surface tension. These can result in a Marangoni stress τ_γ at the free surface depending on the surfactant properties and flow conditions as

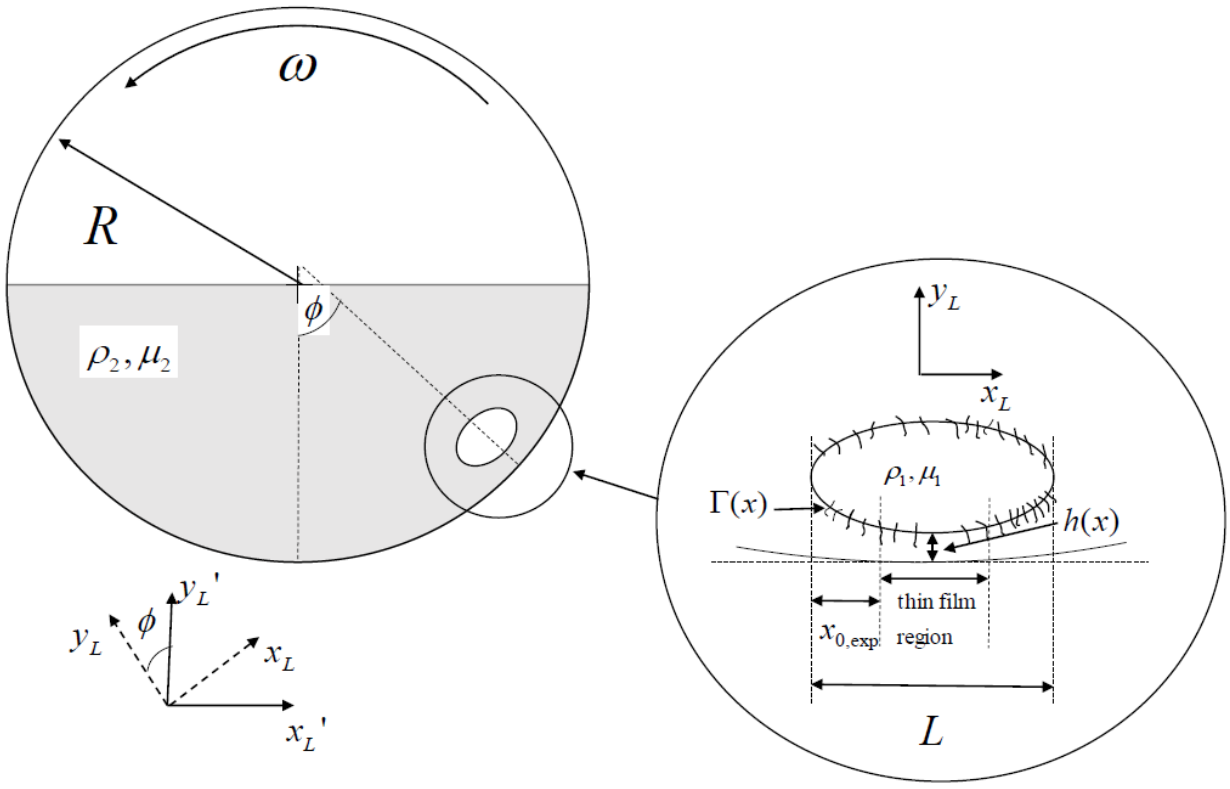

Figure 5.1 *Problem schematic showing the cross section of a horizontal tank half-filled with a viscous liquid that contains a surfactant laden drop with bulk concentration C_o. The rotates with rate ω causing the drop to reach the equilibrium angle ϕ. Locally there is a thin film, $h(x)$, shown in the inset that separates the drop from the tank wall.*

measured by the capillary number $Ca^* = U\mu_2/\gamma_0$. Here γ_0 denotes the surface tension in the absence of surfactant, also called the clean interface surface tension. Assuming steady and incompressible fully developed flow in the low Reynolds number ($Re_h^* = \rho_2 U h_{min}/\mu_2$) limit it is possible to approximate the horizontal velocity component in the viscous thin film region as

$$u_2 = \frac{1}{2\mu_2}\frac{dP_2}{dx}(y^2 - 2hy) + \frac{\tau_\gamma}{\mu_2}y + U \tag{5.1}$$

by performing a standard lubrication analysis (82). To utilize the lubrication approximation we use the minimum film thickness h_{min} and capillary length $\ell_c = \sqrt{\gamma/\Delta\rho g}$ as the natural length scales for the think film regions x and y directions, respectively. Here, g denotes the gravitational acceleration constant with $\Delta\rho = \rho_1 = \rho_2 > 0$. Then the geometric and dynamic requirement for the lubrication approximation are small gradients in the film $dh/dx < 1$ and $(h_{min}/\ell_x)Re_h^* < 1$, respectively.

The area flux of fluid through the thin film region inlet and outlet boundaries located at $x = 0$ and $x = x_{end}$, respectively, may be determined by integrating the velocity once yielding

$$q = -\frac{1}{3\mu_2}\frac{dP_2}{dx}h^3 + \frac{\tau_\gamma}{2\mu_2}h^2 + Uh. \tag{5.2}$$

The pressure in the thin film P_2 and Marangoni shear stress τ_γ are determined from the interface stress balance $\boldsymbol{n}\cdot\boldsymbol{\sigma}_1 - \boldsymbol{n}\cdot\boldsymbol{\sigma}_2 = -\boldsymbol{\nabla}_s\gamma + \boldsymbol{n}\gamma\kappa$ where $\boldsymbol{\sigma}_i = -p_i\boldsymbol{I} + \boldsymbol{\tau}_i$ is the stress tensor. Here $p_i = P_i - \rho_i g(ycos\phi - xsin\phi)$ is the modified pressure with the viscous stress component written $\boldsymbol{\tau}_i = \mu_i[\boldsymbol{\nabla u} + (\boldsymbol{\nabla u})^T]$. The surface gradient operator $\boldsymbol{\nabla}_s$ is defined as $\boldsymbol{\nabla}_s = (\boldsymbol{I} - \boldsymbol{nn})\cdot\nabla$. The two-dimensional interface normal is

$$\boldsymbol{n} = (n_x, n_y) = \frac{1}{\left[1 + \left(\frac{dh}{dx}\right)^2\right]^{1/2}}\left(-\frac{dh}{dx}, 1\right). \tag{5.3}$$

Through an order of magnitude analysis of the terms in the normal component of the interface stress balance an expression for the static pressure in the film is found,

$$P_2 = -\gamma \boldsymbol{\nabla} \cdot \boldsymbol{n} - \Delta\rho g(h\cos\phi - x\sin\phi). \tag{5.4}$$

The order of magnitude of the terms in the tangential component of the interface stress balance were also considered and expression for the Marangoni stress is found,

$$\tau_\gamma = \mu_2 \frac{\partial u}{\partial y} = \left[1 + 3\left(\frac{dh}{dx}\right)^2\right] \frac{d\gamma}{dx}. \tag{5.5}$$

Many of the $O[(dh/dx)^2 \ll 1]$ terms were retained in order to derive the above equations so that we are able to apply boundary conditions for the curvature, κ, at the leading edge of the thin film region, $x = 0$. Details on this analysis will be available in the paper submitted to *Phys. Rev. Fluids.*

5.2.3 *Surfactant equation of state and interface species conservation*

In general there is an inverse relationship between surfactant concentration and surface tension. An equation of state is required to relate these two quantities. Here we used the non-linear equation of state

$$\gamma = \gamma_0 + n\hat{R}T\Gamma_\infty \left[\ln(1-\theta) + \frac{1}{2}\Lambda(\theta)^2\right], \tag{5.6}$$

where $\theta = \Gamma/\Gamma_\infty$ is the fractional surface coverage as used in previous chapters. The equation of state was derived from the Frumkin isotherm $\theta_{eq} = [K_{eq}C_i]/[e^{-\Lambda\theta_{eq}} + K_{eq}C_i]$ that is used to relate a bulk subsurface concentration, C_i, to an equilibrium surface concentration, Γ_{eq} (60; 61; 62). The parameter n is either 1 or 2 denoting a non-ionic or ionic species, respectively. Only 2 is used here but we write the full expression for reference. The isotherm has three unknown parameters Γ_∞, Λ and K_{eq} representing the maximum surface coverage,

molecular interaction parameter and bulk distribution coefficient, respectively. Pendant drop analysis of equilibrium surface tension data was used to tabulate these values from chapter 2.

To determine the surfactant distribution on the interface we consider the species conservation equation (87),

$$\boldsymbol{\nabla}_s \cdot (\boldsymbol{u}_s \Gamma) + (\boldsymbol{\nabla}_s \cdot \boldsymbol{n})(\boldsymbol{n} \cdot \boldsymbol{u})\Gamma - j = 0 \tag{5.7}$$

where $\boldsymbol{u}_s = [\boldsymbol{I} - \boldsymbol{nn}] \cdot \boldsymbol{u}$. The flux j of surfactant to the interface is the model developed in chapter 4,

$$j = \hat{\beta}_0 C_i^{1+m}(1-\theta) - \hat{\alpha}_0 C_i^m e^{-\Lambda\theta}\theta. \tag{5.8}$$

The surface-bulk surfactant distribution coefficient is related to the adsorption and desorption rate constants at $C_i = 1$ mM, $\hat{\beta}_0$ and $\hat{\alpha}_0$, according to the relationship $K_{eq} = \hat{\beta}_0/\hat{\alpha}_0$.

5.2.4 *Non-dimensionalization, solution method and boundary conditions*

To model the thin film region with Marangoni stresses we solved the depth averaged flux equation with Eq. 5.2 and the unsteady form of the species conservation equation Eq. 5.7 with the pressure and Marangoni shear stress provided by Eqs. 5.4 and 5.5. The equations were integrated until equilibriums were reached.

The terms that were included in the depth averaged continuity equation were made dimensionless using the following parameters:

$$h^* = \frac{h}{\ell_c}, \quad x^* = \frac{x}{\ell_c}, \quad P^* = \frac{\ell_c}{\gamma_0}P, \quad q^* = \frac{\mu_2}{\gamma_0 \ell_c}q, \quad t^* = \frac{\gamma_0}{\ell_c \mu_2}t. \tag{5.9}$$

These yield the dimensionless flux equation

$$q^* = -\frac{1}{3}\frac{\partial P_2^*}{\partial x^*}h^{3*} + \frac{\tau_\gamma^*}{2}h^{2*} + Cah^*, \tag{5.10}$$

that was used with the dimensionless depth averaged continuity equation

$$\frac{\partial h^*}{\partial t^*} = -\frac{\partial q^*}{\partial x^*}. \tag{5.11}$$

As part of the solution procedure the curvature at the leading edge of the thin film region $\kappa^* = m_2/(1+m_1^2)^{3/2}$ is fixed. Here $m_1 = [\partial h^*/\partial x^*]_{x^*=0}$ and $m_2 = [\partial^2 h^*/\partial x^{*2}]_{x^*=0}$. These constants m_1 and m_2 are determined using fits of a fourth order polynomial to the experimental drop profiles. Additional details on the solution procedure for these equations including initial and boundary conditions are included in the paper submitted to *Phys. Rev. Fluids*.

The species conservation equation and equation of state were made dimensionless using,

$$\theta = \frac{\Gamma}{\Gamma_\infty}, \quad \gamma^* = \frac{\gamma}{\gamma_0} \tag{5.12}$$

with associated dimensionless Frumkin equation of state

$$\gamma^* = 1 + nCa^*Ma^*\left[\ln(1-\theta) + \frac{1}{2}\Lambda\theta^2\right]. \tag{5.13}$$

To solve the interface species conservation equation we recast Eq. 5.7 in the unsteady conservation form

$$\frac{\partial \theta}{\partial t^*} = -\boldsymbol{\nabla}_s^* \cdot (\boldsymbol{u}_s^*\theta) - (\boldsymbol{\nabla}_s^* \cdot \boldsymbol{n})(\boldsymbol{n} \cdot \boldsymbol{u}^*) + j^*. \tag{5.14}$$

with the dimensionless interface flux written as

$$j^* = Ca^*Bi_\beta^*(1-\theta) - Ca^*Bi_\alpha^*\theta e^{-\Lambda\theta}. \tag{5.15}$$

The problem depends upon the following dimensionless groups,

$$Ca^* = \frac{U\mu_2}{\gamma_0}, \quad Ma^* = \frac{RT\Gamma_\infty}{U\mu_2}, \quad Bi^*_\beta = \frac{\beta C_0 \ell_c}{U\Gamma_\infty}, \quad Bi^*_\alpha = \frac{\alpha \ell_c}{U\Gamma_\infty} \tag{5.16}$$

which are the capillary, Marangoni and adsorption/desorption Biot numbers, respectively. We use the dimensionless groups as operating parameters for comparison between the experimental and computational results. Note that the clean interface surface tension was used in non-dimensionalization.

5.3 Experiments and results

5.3.1 *Setup, procedure and range of parameters*

Experiments were performed by using an acrylic cylindrical tank placed on two roller bars that were driven by a DC motor. The tank had an inner radius of 34.5 mm, length of either 67 or 80 mm, and was closed with circular acrylic pieces at both ends. One circular end of the tank had two holes on opposite ends of the face that were closed with threaded plugs. These holes were necessary for filling the tank with oil and inserting the drop containing surfactant, as well as for emptying and cleaning. The tank was filled halfway with light mineral oil (Fisher Scientific) ($\rho_2 = 830$ kg m^{-3}, $\mu_2 = 48$ mPa s) through one of the access holes. A 400 μl drop was carefully placed in the tank using a pipette (BioHit) with flexible plastic tubing attached to the pipette tip. This allowed the drop to be placed gently in the tank without the risk of causing breakup. The drop contained either $> 99\%$ sodium dodecylsulfate (SDS) (Fisher Scientific) or $> 97\%$ sodium oleate (SO) (TCI) mixed with deionized water ($\rho_1 = 1000$ kg m^{-3}, $\mu_1 = 1$ Pa s). Surfactants were used as received. Surfactant concentration ranges were $1 < C_i < 8$ mM and $0.5 < C_i < 2$ mM for the SDS and SO, respectively. Transient and equilibrium surface tensions were measured using the pendant drop method and a pattern search algorithm from chapter 2. A similar pattern search method was used to estimate the sorption/desorption rates using the transient pendant drop

Table 5.1 *Frumkin isotherm model constants and maximum surface coverage at C_∞.*

	C_∞ mol m^{-3}	Γ_∞ mol m^{-2}	Λ –	θ_{eq} at C_∞ –	β m s^{-1}	α mol m^{-2} s^{-1}
SDS -mineral oil	8	3.84×10^{-6}	-3.88	0.75	7.2×10^{-8}	6.2×10^{-9}
SO - mineral oil	2.2	3.89×10^{-6}	3.21	0.99	1.2×10^{-7}	6.2×10^{-8}

Table 5.2 *Langmuir isotherm model constants and maximum surface coverage at C_∞.*

	C_∞ mol m^{-3}	Γ_∞ mol m^{-2}	θ_{eq} at C_∞ –	β m s^{-1}	α mol m^{-2} s^{-1}
SDS -mineral oil	8	2.51×10^{-6}	0.99	5.1×10^{-8}	6.2×10^{-9}
SO - mineral oil	2.2	5.26×10^{-6}	0.91	2.9×10^{-7}	6.2×10^{-8}

data in chapter 4. Curve fits of the equilibrium data were produced using both the three parameter Frumkin and two parameter Langmuir isotherms and associated equations of state. A summary of the surfactant transport and kinetic parameters appears in Tables 5.1 (Frumkin) and 5.2 (Langmuir). The adsorption and desorption rate coefficients are given in the tables where $\beta = \hat{\beta}_0 C_i^{1+m}$ and $\alpha = \hat{\alpha}_0 C_i^m$ from chapter 4.

After placing the drop in the tank the access holes were immediately sealed and the tank was placed on the roller bars. The motor began to rotate the roller bars, and subsequently the tank, at inner wall velocities between 9 and 70 mm s^{-1}. A CCD camera was oriented normal to the circular face of the tank without access holes while the drop was illuminated with a fluorescent lamp from the side. Before images were taken the drop remained in the rotating tank for a minimum time equal to the time required for the surface tension to reach equilibrium based on the pendant drop measurements for the surfactant and C_i being used. Images were then taken of the drop positioned at the equilibrium angle ϕ where the value depended on the wall velocity.

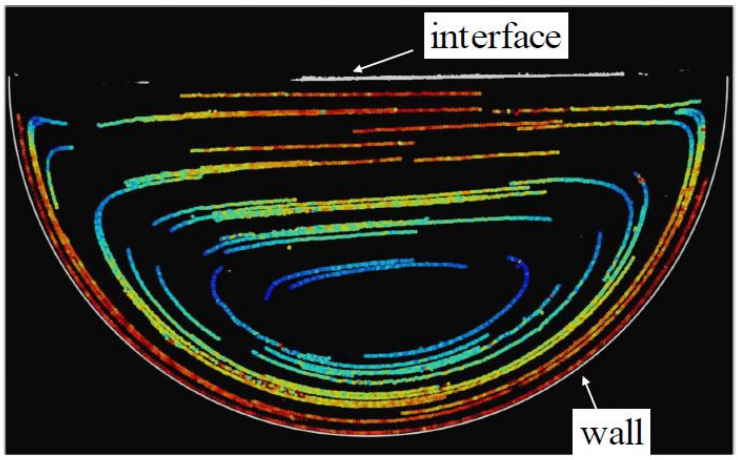

Figure 5.2 *Example of streamline visualization using PIV/PTV in the horizontal tank apparatus. The wall speed is approximately 9 mm s^{-1}. Fluid slip appears in the vicinity of the interface at approximately 80° measured from the bottom.*

Following an experiment the images were analyzed in MATLAB to extract the drop profile and determine the thickness of the film of oil between the drop and tanks wall. The image resolution was between 20 and 30 μm per pixel width where the cameras pixels were square. At least five images for a given drop and wall velocity were taken. The acrylic tank was emptied and rinsed several times with denatured alcohol to remove mineral oil residue followed by a rise with water. The tank was then dried with compressed air.

It was clear that oil velocities just next to the tank wall would experience slip as the free surface was approached. To determine if the drops reached an equilibrium ϕ in this region a PIV/PTV study was performed in the same range of Reynolds numbers. The tank was half filled with corn oil ($\rho = 925$ kg m^{-3}, $\mu = 55$ mPa s). A drop containing 50 mM NaOH was placed in the tank and a saponification reaction occured at the drop surface, producing sodium caboxylate surfactants which greatly lower the surface tension. The drop was allowed to breakup, producing a dispersion of small spherical droplets with radii $b < 0.5$ mm (94). The Stokes numbers for these PIV experiment were $St^* \ll 1$ where $St^* = \frac{2}{9}\frac{\rho_1}{\rho_2}\left(\frac{b}{R}\right)^2 Re_b^*$ with

$Re_b^* = Ub/\nu_2$ (95). A planar laser was used to illuminate the middle cross section of the tank and videos of the tank containing the droplet suspension were recorded for wall velocities of 9.2, 21.2 and 33.2 mm s^{-1}. At higher speeds we were not able to track the individual particles due to frame rate and resolution limits of the CCD camera. An example of the droplets that followed the streamlines is shown in Fig. 5.2. The arc length traveled s versus time t was fit with a linear line indicating a constant velocity even up to an angular position of 80° (81). These velocities closely matched the tank wall velocity for all speeds therefore any effects from the free surface on the flow around the drops in the experiments were negligible.

Based on these parameters, and others mentioned later in the text, it was possible to estimate a range of values for the operating parameters. The capillary length for water in mineral oil was approximately, $\ell_c = 6$ mm. There are a number of Reynolds numbers based on different length scales that were used to describe the system. The Reynolds number based on the tank radius $Re_T^* = UR/\nu_2$ were in the range $5 < Re_T^* < 42$. Reynolds numbers based on the drops length scale b, $Re_b^* = Ub\nu_2$, and thin film, Re_h^*, were $0.7 < Re_b^* < 5.5$ and $0.2 < Re_h^* < 1.5$, respectively. Reynolds numbers based on the capillary length were $1 < Re_{\ell_c}^* < 7$. The corresponding capillary numbers were in the range, $0.005 < Ca^* < 0.05$. The Marangoni numbers were $1.6 < Ma^* < 22$ for both the SDS and SO surfactants. The adsorption Biot numbers were $1 \times 10^{-3} < Bi_\beta^* < 0.1$ and $8 \times 10^{-4} < Bi_\beta^* < 0.05$, for the SDS and SO surfactants, respectively. The desorption Biot numbers were $8.5 \times 10^{-5} < Bi_\alpha^* < 1 \times 10^{-3}$ and $8.4 \times 10^{-4} < Bi_\alpha^* < 0.01$, for the SDS and SO surfactants, respectively.

5.3.2 *Drop profiles and* ϕ

Fig. 5.3 shows images of drops in the horizontal tank apparatus. The left and right columns correspond to aqueous SDS and SO systems, respectively, at concentrations listed below each image. The highest concentrations of 8 mM and 2 mM correspond to experiments performed at the approximate C_∞ value for each surfactant. The capillary number was fixed at $Ca^* = 0.04$ in each experiment. The first two rows of images are for drops that showed

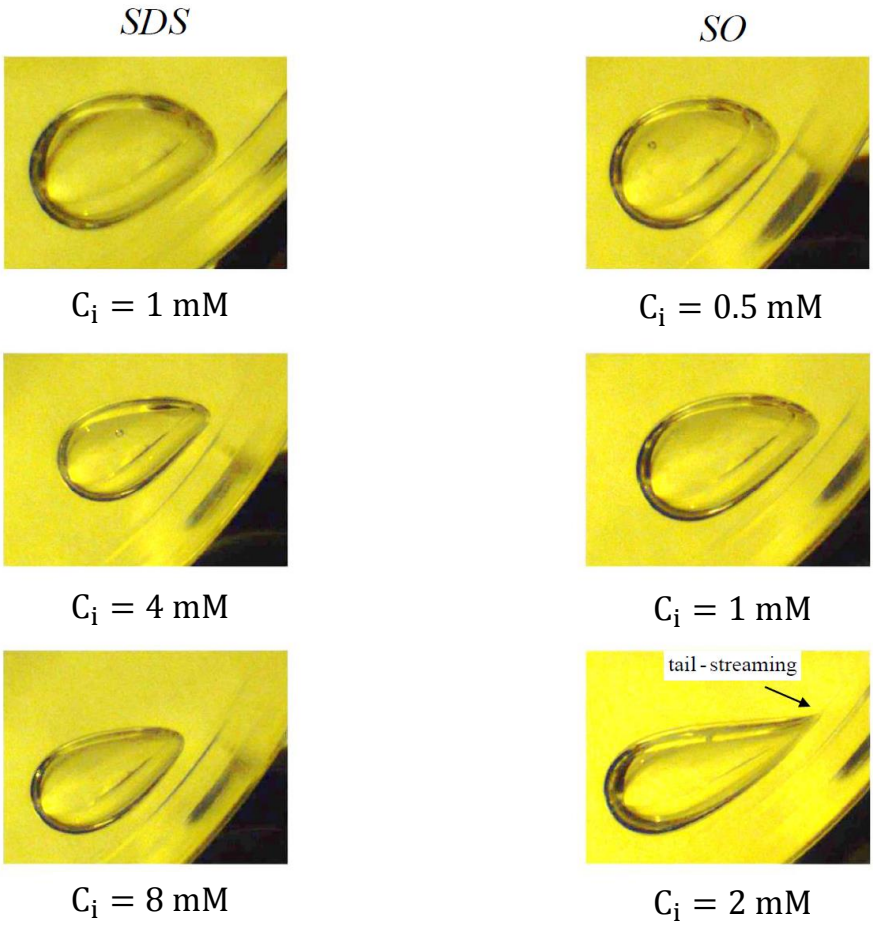

Figure 5.3 *Images of aqueous 400 ml drops containing surfactant concentrations as listed. The capillary number was fixed at* $Ca^* = 0.04$ *in each image shown. As the surfactant concentration increased there was a noticeable change in the drop length* L_γ*. The change was much larger for the SO drops where tail streaming occurred at the highest surfactant concentration (bottom right image).*

similar deformation where the drops were elongated for the 1 and 4 mM SDS and the 0.5 and 1 mM SO surfactant concentrations. Above these concentrations the images differ. The 8 mM SDS experiment showed only marginal additional elongation of the drop when compared to the 4 mM SDS case while the 2 mM SO experiment showed elongation until tail streaming (96) occurred. When viewed from above the SO drops form an unstable cusped region at the trailing edge (97) as seen in Fig. 5.4. This is in contrast to the profile of SDS drops as seen in Fig. 5.5.

In Fig. 5.6 we plot the measured equilibrium angle ϕ corresponding to the drops central location relative to the tank wall versus Ca^*. Values for ϕ were measured for all experiments. Symbols are used to denote the concentration of surfactant and type as listed in the legend. The range of equilibrium ϕ values span from just above 10° for $Ca^* \approx 0.005$ to 40°-50° for $Ca^* \approx 0.05$. The curve for each concentration show similar trends of an increase in ϕ with increasing Ca^*. The shape of each curve is also similar with minor differences in ϕ at the initial and terminal Ca^* values shown.

5.3.3 *Drop profile analysis and m_1, m_2 curvature parameters*

In Fig. 5.7 we plot examples of the experimentally measured drops' cross section profile for two experiments. Fig. 5.7(a) shows the profile for 4 mM SDS and Fig. 5.7(c) for 1 mM SO, both at $Ca^* = 0.045$. The vertical and horizontal axes correspond to the dimensionless profile height y^* and length x^*, respectively. The dotted line adjacent to the horizontal axis is the wall boundary location while the dotted line above denotes the drop profile. The profiles were measured at a distance normal to the wall using image threshold analysis. The solid line is the best fit curve ($4th$ order polynomial) to the drop profile extending from the drops leading edge to just beyond the minimum film thickness. In Fig. 5.7(b) we plot the first and second derivative, m_1 and m_2, along with the curvature for the SDS drops. The dotted line spanning the two images denotes $x^*_{0,exp} = 0.6$ where the approximate leading edge of the thin film region begins i.e. $\kappa^* \approx d^2h^*/dx^{2*}$. These two examples of drop profiles have

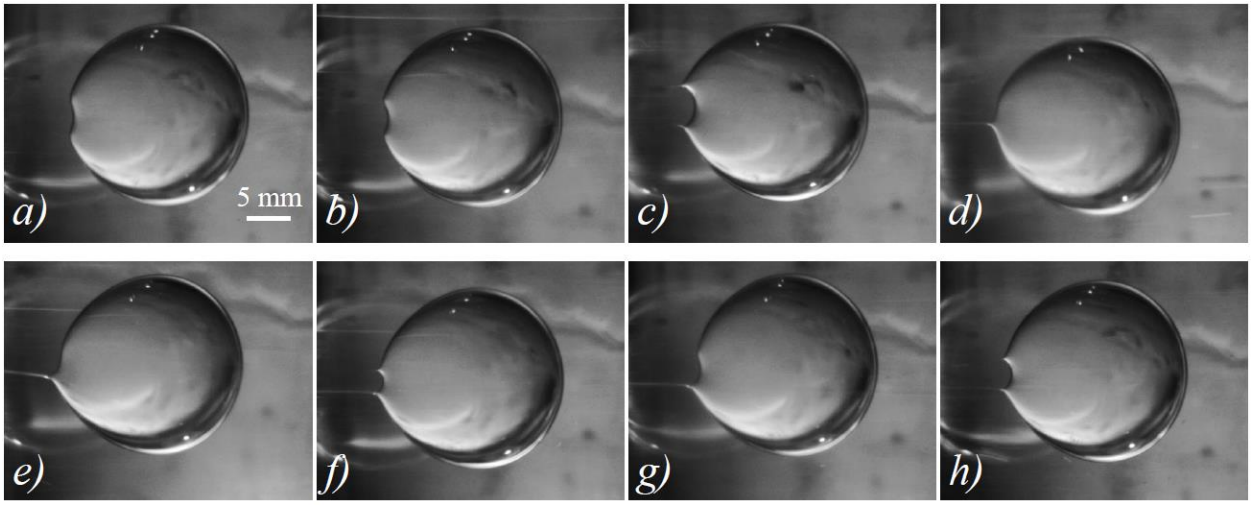

Figure 5.4 *A 400 μl drop with C_i = 2 mM SO in the horizontal tank half-filled with light mineral oil and viewed from above. The capillary numbers are fixed at Ca^* =0.03 in each image. The 8 panels are consecutive images taken at 1 s intervals. They show rather tansient type behavior that accompanies the tail streaming for this surfactant.*

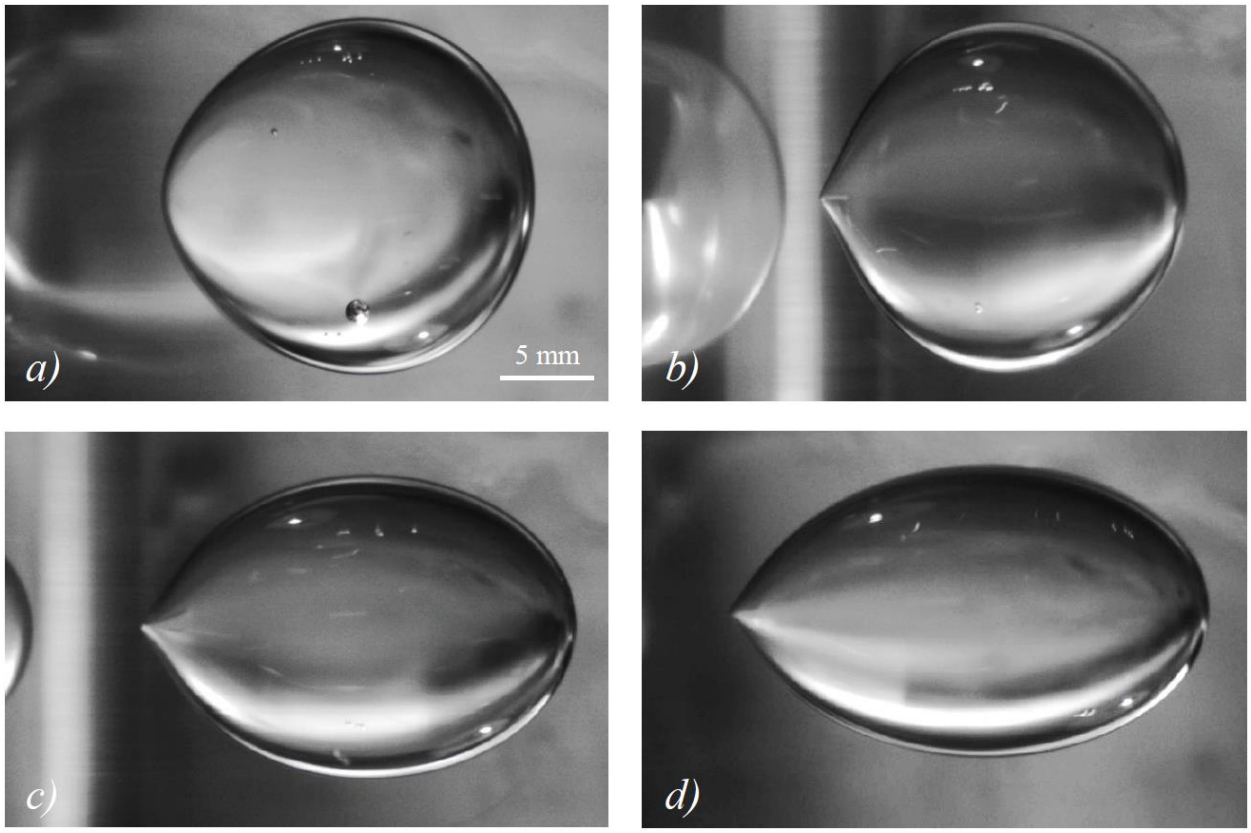

Figure 5.5 *A 400 μl drop with C_i = 8 mM SDS in the horizontal tank appratus half–filled with light mineral oil and viewed from above. The capillary numbers are Ca^* = a) 0.03, b) 0.07, c) 0.11, and d) 0.15. The range of capillary numbers are larger than the ones discussed elsewhere in the chapter and demonstrate that tail streaming is possible with the SDS at high capillary numbers according to panels (c) and (d).*

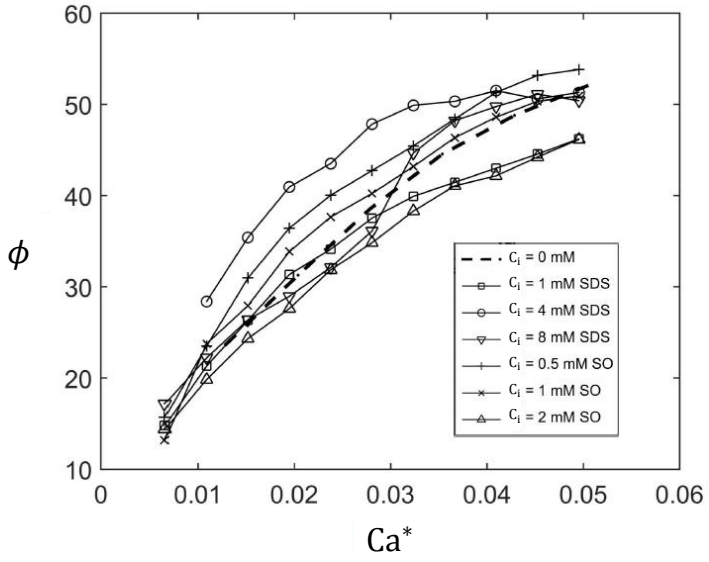

Figure 5.6 *Plot of drop equilibrium wall angles ϕ versus Ca^*. Symbols are used to denote the surfactant concentration as listed in the legend. The symbol-surfactant concentration relationships shown here are used throughout this chapter.*

similar shape with a constant curvature region near the drops leading edge following by a nearly flat region where the minimum film thickness occurs, then a sharp transition upward at the trailing edge. The 1 mM SO drop has a slightly larger overall length, L_γ, than the measured length for the 4 mM SDS profile.

In Fig. 5.8 data for these m_1 and m_2 values were plotted versus Ca^*. The location where the thin film region begins was not arbitrary and was fixed at $x^*_{0,exp} = 0.6$ (see Fig. 5.7(a)-(b)). The location $x^*_{0,exp} = 0.6$ was chosen to satisfy the lubrication requirement that $dh^*/dx^* < 1$ which results in $\kappa^* \approx d^2h^*/dx^{2*}$ (see Fig. 5.7(b)) while providing a dimensionless domain length of approximately one (A broader discussion of how the profiles generated from numerical integration of the governing equations change with $x^*_{0,exp}$ and several other parameters appears later in the text). The solid lines are best fits to each of the data sets with each line corresponding to a given surfactant concentration. There are two global trends of a decrease in m_1 and an increase in m_2 both for an increase in Ca^*. The range of m_1 values are slightly more negative at the highest surfactant concentration

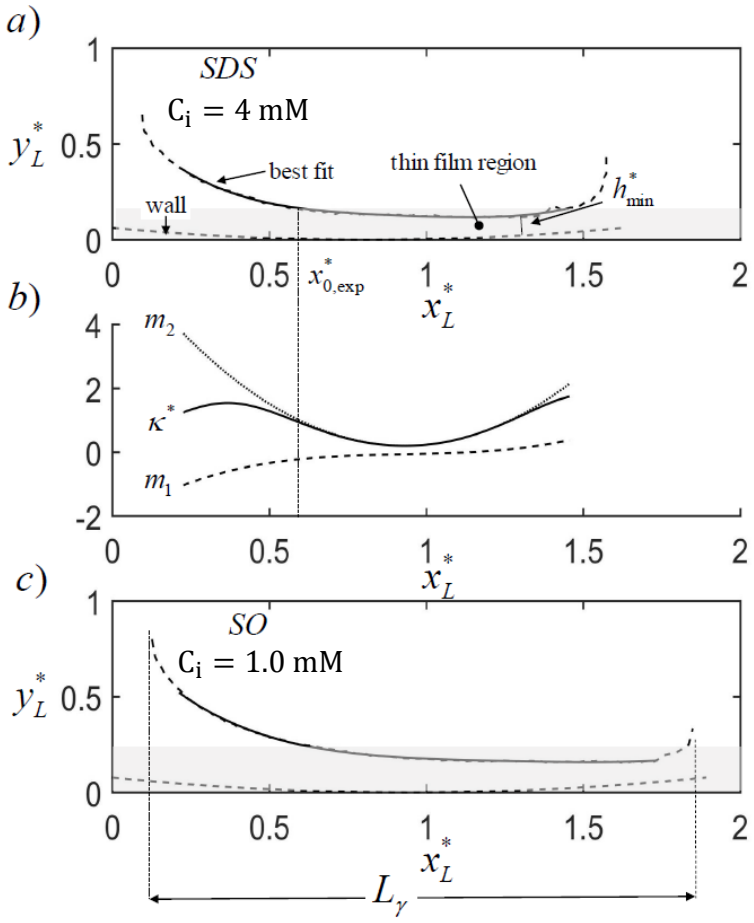

Figure 5.7 *Two examples of dimensionless drop profile height and wall location (dotted lines) made dimensionless using the capillary length $\ell_c = 6$ mm. The concentrations were a) 4 mM SDS and c) 1 mM SO. The capillary number for the experiments were Ca^*=0.045 in these two images. The solid line overlaying the drop profiles denotes the best 4th order polynomial curve fit of the experimental profile. Panel b) shows the resulting derivatives $m_1 = dh^*/dx^*$ and $m_s = d^2h^*/dx^*$ and curvature κ^* of the 4th order polynomial for (a).*

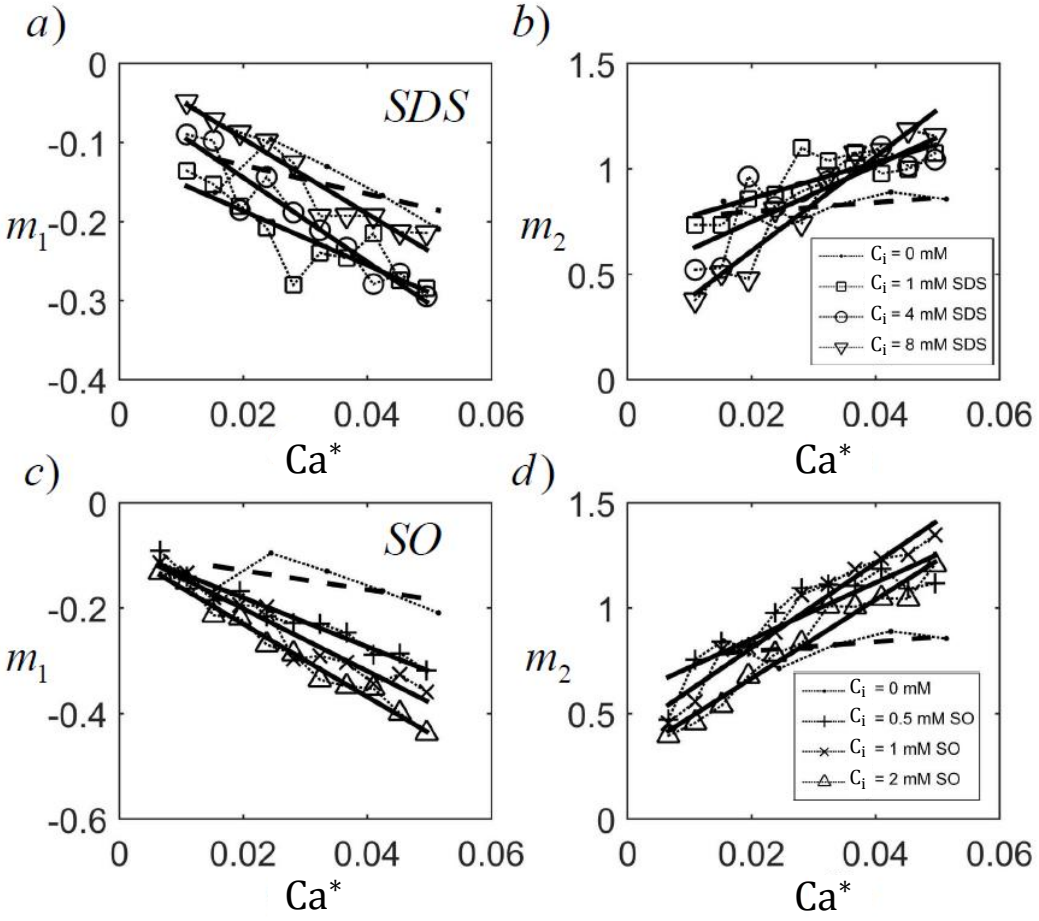

Figure 5.8 *Plots of the first and second derivatives m_1 and m_2 from the polynomial fits to the drop profiles for $x^*_{o,exp} = 0.6$. Solid lines are linear best fits to the data for each concentration. The dotted line is the $C_i = 0$ mM case. The slope and intercept for each curve was used to estimate the curvature boundary conditions at the leading edge of the drop.*

and capillary number for the SO experiments when compared to the SDS. For the m_2 values they are similar when comparing the two surfactants. There is an intersection in the m_2 values for the SDS and SO surfactant that appear at $Ca^* = 0.04$ and 0.02, respectively.

5.4 Comparison between theory and experiments

5.4.1 *Numerical method*

The film evolution equation, eq. 5.11 with appropriate boundary conditions were solved with the interface species conservation equation, eq. 5.14. The equations were simultaneously advanced in time using an explicit Runge-Kutta-Merson algorithm (98) until the film thickness and surface concentration reached an equilibrium (83). Details on the numerical solution procedure are included in the paper submitted to *Phys. Rev. Fluids*.

5.4.2 *Computational results*

In Fig. 5.9 thin film and surfactant concentration profiles from the integration of the governing equations were plotted for SO surfactant at $C_i = 1$ mM with $Ca^* = 0.045$. Data is shown for *i*. $x_{0,exp} = 0.6$ and *ii*. 0.7 both using the Frumkin surfactant model, *iii*. $x_{0,exp} = 0.6$ using the Langmuir model i.e. $\lambda = 0$, and *iv*. $x_{0,exp} = 0.6$ with $x^*_{end} = 2$. The $x_{0,exp} = 0.7$ film profile has the largest h^*_{min} of the three cases with $x^*_{end} = 1$. The $x_{0,exp} = 0.6$ using the Langmuir and Frumkin surfactant models have similar h^*_{min} values but the h^*_{min} locations are not similar where the minimum film thickness appears closer to the drops trailing edge when using the Frumkin model. Larger computational domains produce the largest values for h^*_{min} when comparing the $x^*_{end} = 2$ profile to the others shown. Also it appears that the profile begin to resemble the classic one predicted by F. P. Bretherton (25).

Results for the surface concentrations are also shown in Fig. 5.9. The Langmuir surfactant model produces the lowest surface concentration shown. This is not surprising since $\theta < 1$ at C_∞ for SO surfactant according to the Langmuir isotherm. So complete equilibrium surface coverage requires a higher bulk concentration C_i that exceeds C_∞ for SO surfactant when using the transport parameters for the Langmuir isotherm. The same is not true when

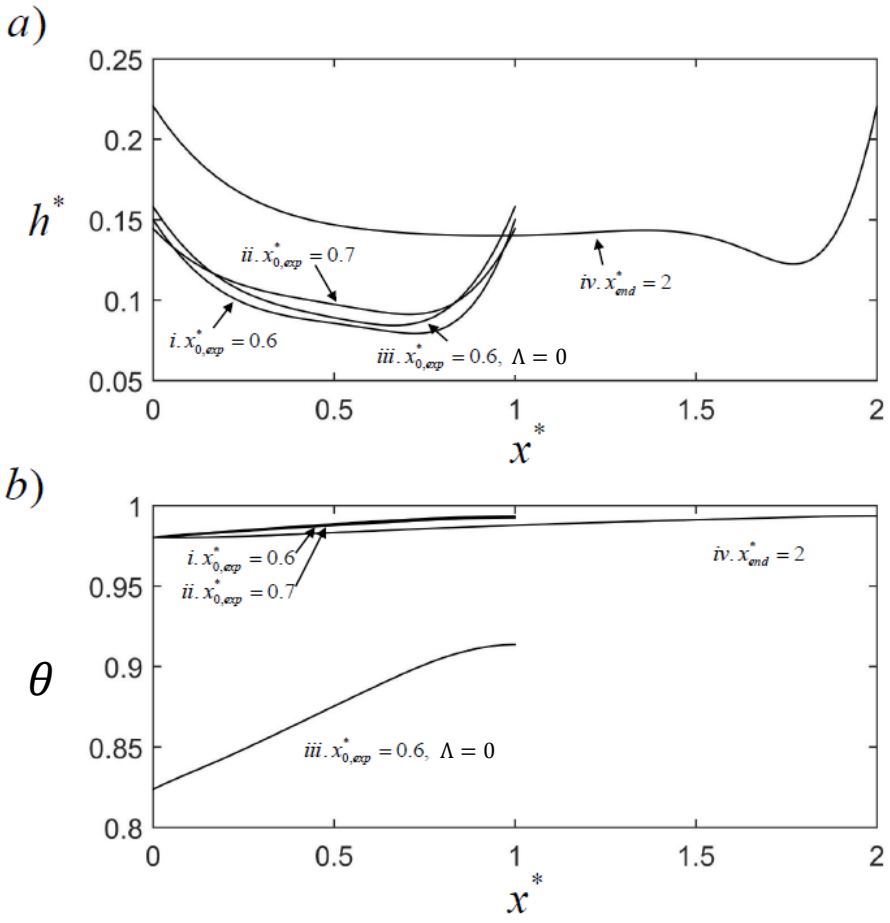

Figure 5.9 *Numerically generated graphs showing the a) thin film h^* and b) concentration Γ^* profiles for SO at 1 mM and $Ca^* = 0.045$ with i.) $x^*_{0,exp} = 0.6$, ii.) $x^*_{0,exp} = 0.7$, iii.) $x^*_{0,exp} = 0.6$ with $\Lambda = 0$ (Langmuir), and iv.) $x^*_{0,exp} = 0.6$ with $x^*_{end} = 2$.*

using the Frumkin isotherm model where higher equilibrium surface coverage is achieved even at bulk concentrations half of C_∞. Also, notice that the maximum surface concentrations are similar for all of the Frumkin isotherm results independent of x^*_{end} or small changes in $x_{0,exp}$.

Fig. 5.10(a)-(c) shows thin film profiles (thick solid lines) from integration of the governing equations for a) $C_i = 0$ mM b) SDS at $C_i = 8$ mM and c) SO at $C_i = 2$ mM all at $Ca^* = 0.05$. The velocity profiles in the corresponding thin film regions for the stationary-wall frame of reference are also shown along with corresponding experimental images next to each plot. When plotting the velocity profiles in the stationary-wall frame of reference it is possible for two types stagnation points to appear (84). The first type, called attractive, is a stagnation point where the velocity is positive to the left and negative to the right so that the velocity vectors point toward the stagnation point. Repulsive stagnation points are the opposite, so the velocity vectors point away from the stagnation point. Note that the use here of attractive and repulsive is different from the one used to describe the molecular interaction parameter in the introduction. Also note that whenever two stagnation points appear on the interface in the thin film region they cannot be of the same type i.e. two attractive points cannot reside next to one another and vice versa.

The result Fig. 5.10(a) for $C_i = 0$ mM shows two stagnation point regions, a repulsive stagnation point at the leading edge of the thin film region followed by a repulsive one. The $C_i = 8$ mM SDS surfactant shows a repulsive stagnant region near the thin film regions trailing edge. Here the Marangoni stresses drag fluid from the rear into the thin film region. The same is seen for the $C_i = 2$ mM SO surfactant except that the repulsive stagnation point is situated well before the thin films trailing edge. This results in a reversal of the velocity at the thin films trailing edge for the SO surfactant at this particular concentration and value for Ca, and the fluid after the repulsive stagnation point locally moves the fastest. A seen in the experimental image to the right of Fig. 5.10(c) this flow reversal coincides with experimental observations of tail streaming.

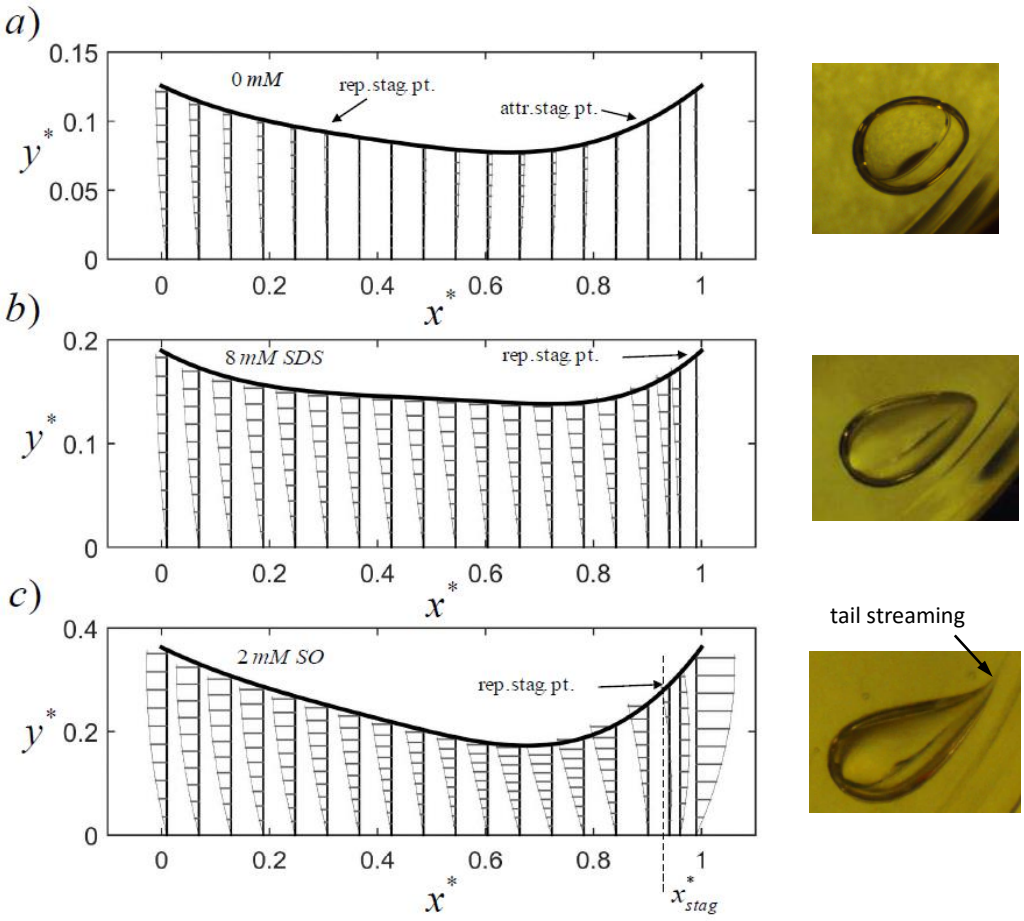

Figure 5.10 *Three examples of results from numerical integration showing film profiles (thick solid lines) at C_i = a) 0 mM SDS, b) 8 mM SDS, and c) 2 mM SO all at Ca^* =0.05. Also plotted are the thin film velocity profiles in the drops frame of reference. Attractive and repulsive stagnation points are labeled. To the right of each plot is an experimental image of a drop corresponding to the conditions represented in the numerical solutions.*

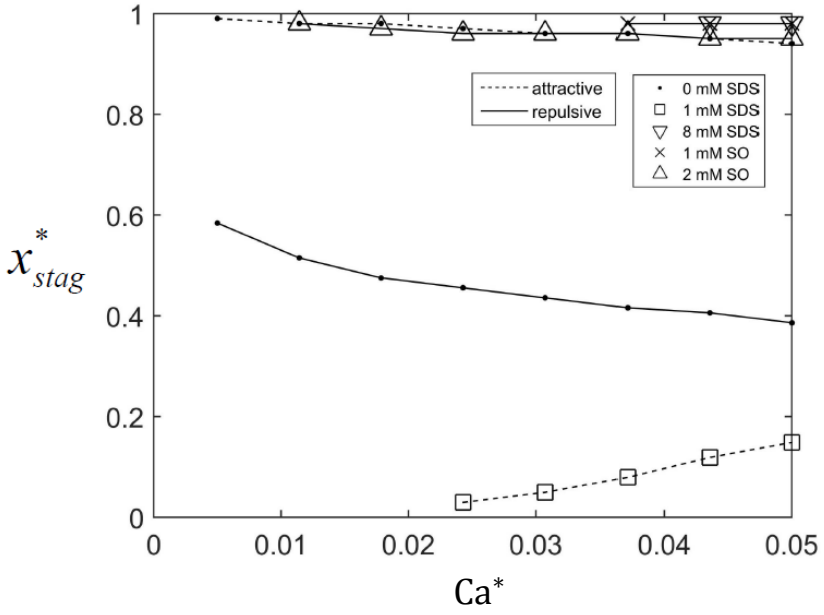

Figure 5.11 *Plot of stagnation point location x^*_{stag} versus capillary number. The symbols are used to denote the bulk surfactant concentration, C_0, for the cases where stagnation points appear in the thin film region. Line types are used to distinguish between attractive (dashed line) and repulsive (solid line) stagnation points.*

In Fig. 5.11 we plot the location of the stagnation points x^*_{stag} determined from the numerical data versus capillary number. The type of stagnation point is denoted using a dashed (attractive) or solid (repulsive) line. Symbols are used to denote the surfactant concentration and type as listed in the legend. The general trends are the appearance of two stagnation points when no surfactant is present. Both of these stagnation points move toward the thin film regions leading edge as the capillary number increases. At low SDS surfactant concentration there is a single attractive stagnation point that appears near the thin film regions leading edge and moves toward the rear as the capillary number increases. For intermediate concentrations, $C_i = 4$ mM SDS and 0.5 mM SO, there are no stagnation points in the thin film region. At the highest concentrations though a repulsive stagnation point appears. The location of the repulsive stagnation point is closer to the thin films

leading edge for the $C_i = 2$ mM SO surfactant when compared to the $C_i = 8$ mM SDS surfactant.

5.4.3 *Comparison between experiments/theory and discussion*

In Fig. 5.12 we plot both the experimentally measured and numerically determined dimensionless minimum film thickness, h^*_{min} versus capillary number, Ca^*. The lines with symbols correspond to the experiments while the solid line with dots $- \cdot -$ are the curves generated from numerical data. Also plotted for reference is the zero surface tension data. No errorbars are plotted along with the experimental data since they are uniform and correspond to the size of a single pixel. The range of values for the minimum film thickness span 5-20% of the capillary length.

Both sets of data show the expected general trend of an increase in the film thickness with an increase in the capillary number. This is true across all the experiments and numerical data sets. Also, the trends are nearly similar in regards to the rate of increase in minimum film thickness for a given concentration, where an increase in concentration typically results in a relatively larger rate of increase in the minimum film thickness. This trend though is not true for all of the numerical SDS data where the $C_i = 4$ mM curve crosses the $C_i = 8$ mM curve near $Ca^* \approx 0.040$. The experimental data though does show a narrowing of the distance between the two curves for the $C_i = 4$ and 8 mM data sets over the same region. But at the highest capillary number, $Ca^* = 0.050$ the experimentally measured minimum film thickness is greatest at 8 mM. It is clear from the data though that the minimum film thickness for both 4 and 8 mM SDS have a greater rate of increase than the $C_i = 0$ and 1 mM SDS in both the measured and calculated data sets. For the SO data the measured and computed minimum film thickness values show good agreement for most concentrations and capillary numbers. The few exceptions exist at the moderate capillary numbers $0.020 < Ca^* < 0.035$ where for a brief period of Ca^* values the film thickness is larger for the $C_i = 0.5$ mM when compared to the $C_i = 1$ mM SO data. This was not reproduced in the numerical data

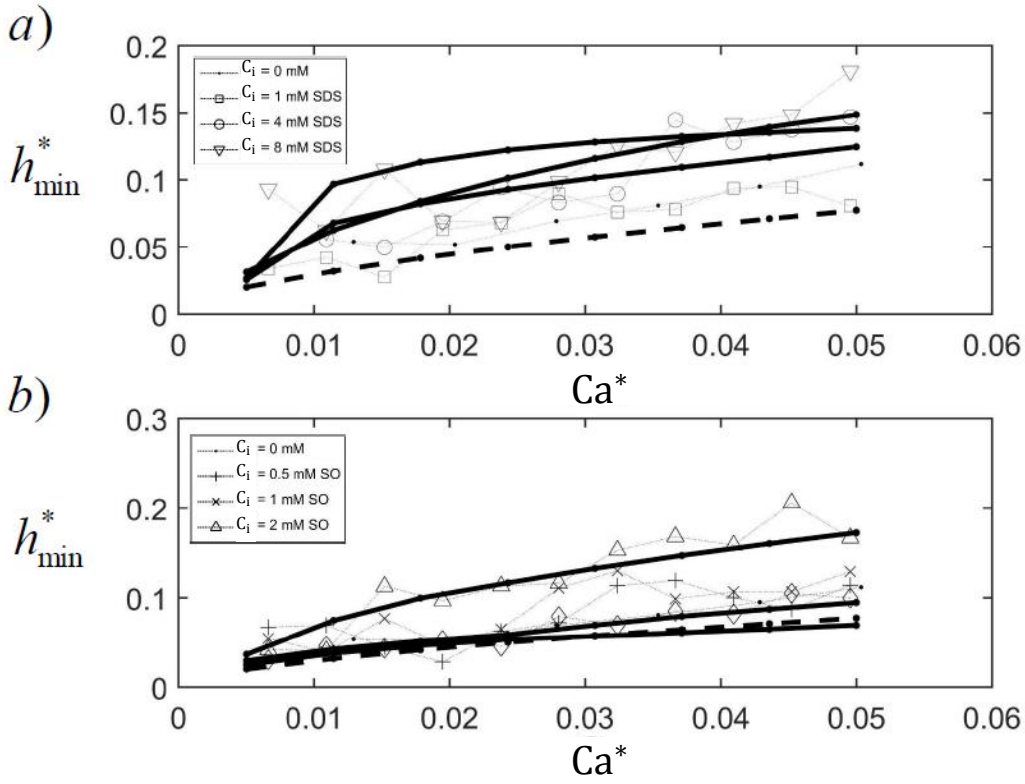

Figure 5.12 *Comparison between experiments and numerics for the minimum film thickness h_{min} versus capillary number Ca^*. The solid and dashed lines are results of the numerical integration over the same range of capillary, Marangoni and Biot numbers as measured in the experiments.*

curve with much clearer trends of an increase in concentration results in a thicker film for a given capillary number. The computed film thickness data shown in Fig. 5.12(b) does reproduce the trends seen in the measured values where there is a greater rate of increase in the minimum film thickness between the $C_i = 1$ and 2 mM curves when compared to the $C_i = 0.5$ to 1 mM ones.

Given the good agreement between experiments and theory, in terms of measurements for the minimum film thickness, we now use the numerical data to estimate the maximum surfactant concentration and subsequently the minimum surface tension. The purpose is to update the capillary number with the minimum surface tension and use those values

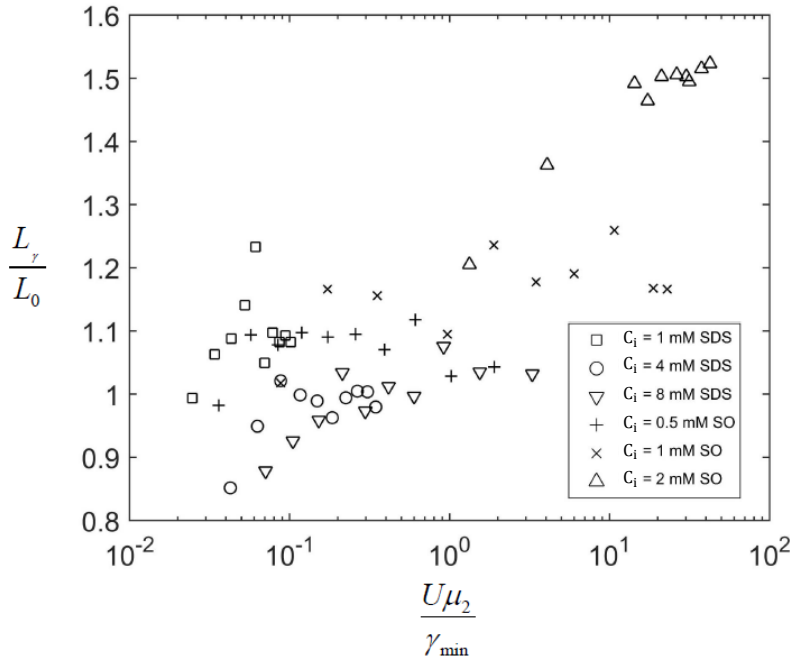

Figure 5.13 *Plot of the normalized drop length L_γ/L_0 versus maximum capillary number $U\mu_2/\gamma_{min}$ based on the minimum surface tension γ_{min} determined from the integration of the couple thin film and species conservation equations.*

to generate plots of the measured drops' elongation, L_γ versus $Ca^*_{max} = U\mu_2/\gamma_{min}$. The results from the analysis are shown in Fig. 5.13, detailing the normalized elongation, L_γ/L_0 (here L_0 is the $C_i = 0$ mM drop length) versus the modified capillary number based on the estimates from the numerical data for the minimum surface tension, Ca^*_{max}. The normalized elongation spans from just below 0.9 to a maximum of approximately 1.5. The modified capillary number spans 4 orders of magnitude from just above 0.01 to just below 100. The data seems to confirm the experimental observations where larger modified capillary numbers correspond to greater drop elongation. Few of the SDS experiments have elongation greater than unity while most of the SO values do. The capillary number for this transition appears to be in the range 0.1 to 1.

Whether or not the flow reversal seen in Fig. 5.10 is responsible for the tail-streaming observed in the experiments or just a coincidence is difficult to decisively conclude. The main

reason is the fact that the experiments contain three-dimensional effects (97) that cannot be accounted for in the two-dimensional simulations. Also, since the computational domain is fixed in this thin film analysis ($x^*_{end} = 1$) it is difficult to make a one-to-one comparison. But the fact that the Frumkin isotherm predicts complete coverage for the SO surfactant at concentrations below the CMC would at least suggest that the use of the more complex isotherm has its benefits in understanding surfactant behavior in thin films. Furthermore, the stagnation point analysis does seem to suggest that at high capillary number, Ca^*, and bulk surfactant concentration, C_i, it is possible to produce a flow at the drops rear that would be favorable to tail-streaming.

5.5 Conclusions

In this chapter we presented experiments and computation for the thin film separating a surfactant-laden drop from the rotating wall of a horizontal cylindrical tank. The experiments were preformed using a horizontal rotating tank that contained light mineral oil. The drop phase consisted of either aqueous sodium oleate (SO) or sodium dodecyl sulfate (SDS). Using image analysis we were able to measure the minimum film thickness as a function of capillary number in the range $0.005 < Ca^* < 0.05$. The capillary numbers were based on the clean surface tension. The minimum film thickness for the two surfactants were similar but the SO surfactant showed greater deformation as measured by stretching of the drops which eventually led to tail streaming.

The computation was used to compliment the experiments by providing an estimate for the surfactant concentration and subsequently the surface tension which could be used to provide a better estimate for the capillary numbers. Here a partial lubrication analysis of the momentum and species conservation equations were performed. The partial lubrication analysis allowed us to impose curvature boundary conditions at the drops leading edge. Values for the derivative used to estimate the curvature at the leading edge were taken from the experiments. To model the surfactants we used the Frumkin isotherm and equation of

state. The comparison between experiments and computation were good for the limited range of capillary numbers.

The two surfactants had almost equal and opposite interaction parameters, Λ, with the SDS having a negative (net repulsion) value and the SO having a positive (net attraction) value. This results in the SDS surfactant not reaching complete surface coverage even as the bulk concentration approaches the critical micellar concentration (CMC). In contrast the SO surfactant does reach complete coverage as the bulk concentration approaches the CMC. This behavior allows for lower surface tensions in the SO experiments and provides an explanation for why the SO drops exhibit tail streaming while the SDS drops do not at similar Ca^*. This fundamental difference between the SO and SDS surfactants cannot be captured using the Langmuir equation of state. In fact using the Langmuir equation of state to fit equilibrium surface tension data the SO was predicted to have a lower surface coverage than the SDS. The importance of the equation of state here should not be overlooked as these explanations and theoretical comparisons to experimental behavior could not be made using a linear or even the Langmuir equation of state.

In the future it will be interesting to apply the horizontal tank apparatus to study deformation of non-Newtonian fluids. The experiments could be performed using a non-Newtonian continuous and drop phase. In terms of the partial lubrication analysis it would be interesting to see how well it performs in comparisons to axisymmetric geometries such as drops in tubes.

CHAPTER 6. THEORY AND EXPERIMENTS ON A BUOYANCY-DRIVEN SURFACTANT-LADEN DROP

6.1 Introduction

When a drop falls or rises in another viscous fluid due to gravity its terminal velocity can be significantly affected by the presence of surface tension gradients on the drop surface. In the absence of temperature gradients these surface tension gradients can develop due to the non-uniform accumulation of surfactant on the drop surface. This is well known and the mechanisms by which surfactants affect droplet motion are decently understood. As surfactant residing in either bulk phase adsorbs to the drop surface, surface convection carries adsorbed surfactant to the rear of the drop. Generally more surfactant accumulates in the rear compared to the front and a surface tension gradient develops over the surface. Surface tension gradients result in a tangential stress called the Marangoni stress which acts to slow down the surface velocity. The magnitude of the surface tension gradient dictates the strength of the Marangoni stress, and at its most extreme the surface can be immobilized i.e. the drop translates like a solid sphere. The surface surfactant concentration profile can be dictated by the adsorption and desorption rates of the surfactant, bulk diffusion and convection, and surface diffusion and convection.

Experiments demonstrating the effect of surface tension gradients date as far back at those by W.N. Bond and D.A. Newton in 1928 (18). While large drops and bubbles translated like ideal fluid spheres, small drops and bubbles fell like solid spheres due to the increasing relative effect of Marangoni stress. Theory describing how surface tension gradients affect drop motion came in the following decades (22; 29; 32; 33; 34; 35; 36; 99; 100). While a

considerable amount of theoretical work as been done on the problem, there have been fewer studies directly comparing experiments to the theory.

Recent studies have used settling drop and bubbles experiments to estimate adsorption behavior. N. Paul *et al* used settling drop velocities as a method for estimating the adsorption of sodium dodecyl sulfate and Triton X-100 surfactants on drop surfaces (44). They determined a relationship between surface coverage and terminal velocity, but the Langmuir isotherm was used to determine a relationship between bulk concentration and surface coverage when it has been shown that better models are available for the surfactants used (45; 46). They also assumed a uniform surface coverage is sufficient to characterize the distribution on a translating drop which may not acceptable, and only one drop size was investigated.

In a theoretical and experimental study, R. Palaparthi *et al* observed air bubbles rising in glycerol-water mixtures containing hexaethylene glycol monododecyl ether ($C_{12}E_6$), a non-ionic surfactant (48). They used non-linear adsorption kinetics similar to Chen and Stebe (36) and found agreement between experimental drag coefficients and numerically predicted drag coefficients using experimentally determined sorption kinetics. However the viscous water-glycerol mixtures made measurements of the sorption rate constants difficult because the increased viscosity made the adsorption process diffusion-limited. Instead a range of rates constants were found that provided good agreement between experiments and theory. As a result the authors concluded that settling bubble experiments could be used to estimate sorption kinetics.

Aside from the results in ref. (48) there is not much literature seeking quantitative agreement between experiments and theory for the buoyancy-driven surfactant-laden drop or bubble problem. Additionally in ref. (48) agreement between experimental and theoretical drag coefficients was found for only a limited range of bubble sizes and surfactant concentrations. In this chapter experimentally determined sorption kinetics found in chapter 4 will be used to estimate drag coefficients of settling surfactant-laden drops. The drops will be aqueous and surfactant will be soluble in the drop phase while assumed insoluble in the

continuous oil phase. The experimental materials are carefully considered so that depletion of surfactant inside the drop can be neglected. For two different continuous phases, the terminal velocities of drops with varying surfactant concentrations and radii will be measured. Both an analytical and numerical approach to the theoretical analysis will be provided, and the experimentally determined sorption kinetics will be incorporated. For certain cases it will be shown that the surface diffusion mechanism that is often neglected in this problem may be required. Both qualitative and some quantitative agreement between experimental and predicted drag coefficients will be presented.

In the next section the theoretical formulation of the problem will be presented along with both an analytical and boundary element approach to solving the governing equations. Reasons for using both approaches will be provided. Afterward the experimental procedure and materials will be discussed followed by experimental results. This will be followed by some theoretical results and then a comparison between the experiments and theory. Finally the a discussion of the results will be followed by some conclusions.

6.2 Theory and analysis

6.2.1 *Conservation of momentum and surface stress balance*

Consider an aqueous drop with radius b settling under gravity g in an immiscible liquid. The drop has density and dynamic viscosity ρ_i and μ_i and the continuous phase has density and dynamic viscosity ρ_o and μ_o. For this analysis it is assumed that $\rho_i > \rho_o$ and $\mu_o > \mu_i$. The Reynolds numbers $Re^* = \frac{2\rho_o bU}{\mu_o}$, where U is the terminal velocity, are small so that Stokes flow is assumed. This along with the Bond numbers $Bo^* = \frac{\Delta\rho g b^2}{\gamma_{min}}$ being small, where γ_{min} is the minimum surface tension on the drop surface, lead us to assume the drops remain spherical.

In the low Re^* limit the fluid dynamics are governed by the Stokes equation

$$\boldsymbol{\nabla} p_k = \mu_k \nabla^2 \boldsymbol{u}_k \tag{6.1}$$

where $p_k = P_k - \rho_k g h$ is the modified pressure, and continuity

$$\boldsymbol{\nabla} \cdot \boldsymbol{u}_k = 0 \tag{6.2}$$

where the subscript k is either o or i for the continuous or drop phases, respectively. The boundary conditions are $\boldsymbol{u}_o = 0$ far from the drop, and at the drop surface $\boldsymbol{u}_i = \boldsymbol{u}_o = \boldsymbol{u}_s$ and

$$\boldsymbol{n} \cdot \boldsymbol{\sigma}_o - \boldsymbol{n} \cdot \boldsymbol{\sigma}_i = -\boldsymbol{\nabla}_s \gamma + \gamma \boldsymbol{n} \left(\boldsymbol{\nabla}_s \cdot \boldsymbol{n} \right) \tag{6.3}$$

where $\boldsymbol{\sigma} = -p_k \boldsymbol{I} + \boldsymbol{\tau}_k$ is the stress tensor, $\boldsymbol{n}$ is the surface normal vector pointing outside the drop, γ is the surface tension and $\boldsymbol{\nabla}_s = (\boldsymbol{I} - \boldsymbol{nn}) \cdot \boldsymbol{\nabla}$ is the surface gradient operator. In the definition of the stress tensor $\boldsymbol{\tau}_k = \mu_k [\boldsymbol{\nabla} \boldsymbol{u}_k + (\boldsymbol{\nabla} \boldsymbol{u}_k)^T]$ is the viscous stress tensor caused by the fluid velocity $\boldsymbol{u}_k$. On the right-hand side of eq. 6.3 the first term is the Marangoni stress and the second is the capillary pressure. The capillary pressure always acts normal to the surface, but the Marangoni stress acts tangentially in the direction of increasing γ. This means Marangoni stress can impact the drag experienced by the drop.

The drag force experienced by the drop is generally proportional to the surrounding fluid density, the square of the drop velocity and the cross-sectional area of the drop by the relationship $F_d = C_d^* \frac{\pi}{2} \rho_o U^2 b^2$. The proportionality coefficient C_d^* is the dimensionless drag coefficient. For a "clean" (i.e. no surfactant) fluid sphere translating with $Re^* \ll 1$ the drag coefficient is $C_{d,HR}^* = \frac{8}{Re^*} \left(\frac{2+3\xi}{1+\xi} \right)$ (19; 20) where $\xi = \mu_i / \mu_o$ is the viscosity ratio. The subscript "HR" stands for "Hadamard-Rybczynski" in reference to the Hadamard-Rybczynski solution. When the same clean fluid sphere is translating steadily due to the buoyant force the drag it experiences is equal to the buoyant force $F_b = \frac{4}{3} \pi \Delta \rho g b^3$. It follows that the velocity of the clean fluid sphere is $U_{HR} = \frac{2}{3} (\Delta \rho g b^2 / \mu_o)(1+\xi)/(2+3\xi)$. For the case of $\xi \to \infty$ which corresponds to a solid sphere the drag coefficient reduces to $C_{d,St}^* = \frac{24}{Re^*}$.

Here the subscript "St" stands for "Stokes" in reference to the Stokes drag law for a solid sphere. Drag coefficients for surfactant-laden drops will fall between $C^*_{d,HR}$ and $C^*_{d,St}$.

6.2.2 *Surfactant equation of state and interface species conservation*

Correctly applying eq. 6.3 requires an understanding of the mass transfer problem. The drop initially contains a uniform concentration of surfactant C_i. The surfactant in the drop will be distributed inside the drop due to internal convection and diffusion, however this portion of the mass transfer problem is neglected in this analysis and the concentration just below the drop surface C_s is assumed to remain nearly uniform i.e. $C_s = C_i$. At the drop surface there is a net flux $-j$ of surfactant adsorbing to the surface from the bulk. Frumkin sorption kinetics (36; 45) with the modification from chapter 4 are used to describe this process,

$$-j = \hat{\beta}_0 C_s^{m+1}(1-\theta) - \hat{\alpha_0} C_s^m e^{-\Lambda\theta}\theta, \tag{6.4}$$

where $\hat{\beta}_0$ and $\hat{\alpha_0}$ are adsorption and desorption rate constants at $C_i = 1$ mM, Λ is the non-ideal interaction parameter, $\theta = \Gamma/\Gamma_\infty$ is the fractional surface coverage of surfactant, and m describes the concentration dependence of the rate constants as discussed in chapter 4. It is assumed that the bulk mass loss parameters $\zeta^* = \frac{\Gamma_\infty A_s}{C_i V}$ from chapter 3 are small enough to neglect depletion of surfactant in the drop. Surfactant that adsorbs to the drop surface will be subject to surface convection and diffusion according to (87)

$$\boldsymbol{\nabla}_s \cdot (\Gamma u_s) - D_s \boldsymbol{\nabla}_s^2 \Gamma = -j. \tag{6.5}$$

In eq. 6.5 on the left-hand side the first term is surface convection where u_s is the surface velocity of the drop and the second is surface diffusion where D_s is a surface diffusivity coefficient. The surface dilation term has been neglected since the drops are assumed to remain spherical, and the unsteady term has been neglected since we seek the steady state

solution. On the right hand side is the source term $-j$ which is the net flux of surfactant to the surface eq. 6.4.

Because eq. 6.3 requires knowledge of *surface tension* gradients and eqs. 6.4 and 6.5 describe the transport of *surfactants*, an equation of state relating the two quantities is required. The choice of Frumkin sorption kinetics requires the Frumkin equation of state (60),

$$\gamma = \gamma_0 + n\hat{R}T\Gamma_\infty \left[\ln(1-\theta) + \frac{1}{2}\Lambda\theta^2\right], \tag{6.6}$$

where γ_0 is the surface tension when $\theta = 0$, and n is the Gibbs coefficient which is 2 for 1:1 ionic surfactants and 1 for non-ionic surfactants. The use of this equation of state requires the assumption that at any location the surface is in a local equilibrium.

In eq. 6.3 the Marangoni stress term -$\boldsymbol{\nabla}_s\gamma$ can be rewritten using the chain rule as -$\frac{d\gamma}{d\Gamma}\boldsymbol{\nabla}_s\Gamma$ where the derivative of the equation of state is explicitly displayed. Then the Marangoni stress can be represented by $-\boldsymbol{\nabla}_s\gamma = n\hat{R}T\left[(1-\theta)^{-1} - \Lambda\theta\right]\boldsymbol{\nabla}_s\Gamma$. This representation of the Marangoni stress provides the coupling between the presence of surfactant concentration gradients and their effect on the shear stress on the surface by way of eq. 6.3, and its form is particularly important for moderate and large θ. A number of authors, even recently, have used a linear equation of state to describe interfacial flow problems such as this (32; 34; 35; 101; 102; 103; 104; 105). This leads to a couple issues: first a linear equation of state greatly overestimates surface tension as surfactant concentrations become moderate or large, and second the Marangoni stress is greatly underestimated leading to unrealistic surfactant concentration profiles on the surface. For example in the above representation of the Marangoni stress the $(1-\theta)^{-1}$ term goes to infinity as $\theta \to 1$, effectively immobilizing the surface before an overaccumulation of surfactant ($\theta > 1$) can occur. A Marangoni stress derived from a linear equation of state would not have this quality and could allow for $\theta > 1$

which would generally be unrealistic excluding monolayer compression or the formation of other phases on the surface.

Solving the coupled mass transfer and fluid dynamics problem described by eqs. 6.1, 6.3 and 6.5 can be done both analytically similar to refs. (34; 35; 36) or numerically such as with the boundary element method (106; 107). In this chapter both approaches will be used. First an analytical solution to eqs. 6.1, 6.3 and 6.5 will be developed similar to ref. (36) but with the surface diffusion term included. As will be shown in experiments this term can explain behavior that would otherwise be impossible to describe without surface diffusion. A description of the analytical approach comes in the next subsection.

The analytical approach becomes mathematically stiff for small Bi^*_α, small $K_{eq}C_i$ and large Pe^*_s which will be explained in more detail in the next subsection. This situation corresponds to the stagnant cap regime where very sharp gradients in surfactant concentration develop. For these cases a boundary element approach to solving eqs. 6.1, 6.3 and 6.5 will be used following the methods described in (107). A description of the boundary element approach comes in the subsection following the next.

6.2.3 *Analytical approach*

For the analytical approach we will operate in a polar coordinate system like that depicted in Fig. 6.1 (note θ is the fractional surface coverage while ϕ is the angular position on the meridional plane). We will begin by defining appropriate scales for the variables. The velocity scale is the terminal velocity U, the length scale is the drop radius b, the surfactant concentration scale is the maximum surfactant concentration for a monolayer Γ_∞, and the stress scale is $\frac{b}{\mu_o U}$. The normal component of eq. 6.3 will be neglected since the drop is assumed to be spherical. What is left is the tangential stress balance,

$$\tau^*_{r\phi,o} - \xi\tau^*_{r\phi,i} = nMa^* \left(\frac{1}{1-\theta} - \Lambda\theta\right)\frac{d\theta}{d\phi}, \tag{6.7}$$

where $\tau^*_{r\phi,k}$ is the dimensionless shear stress for the drop phase ($k = i$) or continuous phase

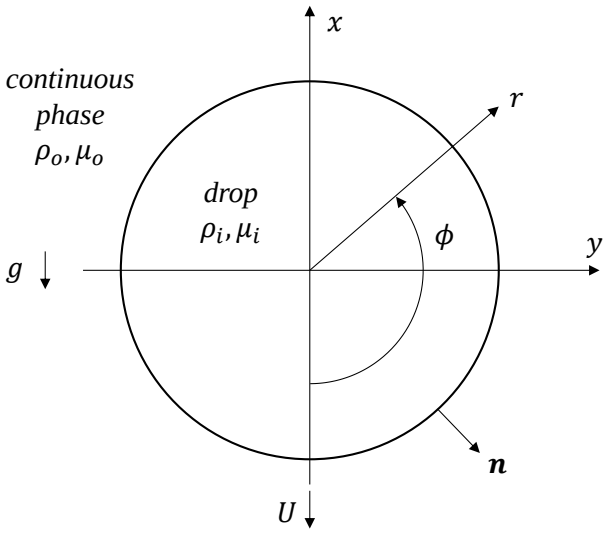

Figure 6.1 *The coordinate system used in the analytical approach.*

$(k = o)$ at the drop surface and $Ma^* = \frac{\hat{R}TT_\infty}{\mu_o U}$ is the Marangoni number relating the importance of Marangoni and viscous stresses. The mass balance eq. 6.5 becomes

$$\frac{1}{sin\phi}\frac{d}{d\phi}(sin\phi\theta u_s^*) - \frac{1}{Pe_s^* sin\phi}\frac{d}{d\phi}\left(sin\phi\frac{d\theta}{d\phi}\right) = Bi_\beta^*(1-\theta) - Bi_\alpha^* e^{-\Lambda\theta}\theta \tag{6.8}$$

where $Bi_\beta^* = \frac{b\hat{\beta_0}C_s^{m+1}}{\Gamma_\infty U}$ and $Bi_\alpha^* = \frac{b\hat{\alpha_0}C_s^m}{\Gamma_\infty U}$ are the adsorption and desorption Biot numbers, and $Pe_s^* = \frac{bU}{D_s}$ is the surface Peclet number. Note that $\frac{Bi_\beta^*}{Bi_\alpha^*} = K_{eq}C_i$ where $K_{eq} = \frac{\beta_0}{\alpha_0}$ is the surface-bulk distribution coefficient from previous chapters. The time derivative in eq. 6.5 is eliminated in eq. 6.8 because we seek the steady state solution. The Biot numbers describe the relative importance of surface convection and adsorption or desorption and the surface Peclet number relates the importance of surface convection and surface diffusion. The quantities Bi_β^*, Bi_α^*, Pe_s^* and Ma^* will dictate the surface concentration profile and to what extent the surface velocity will be slowed.

Equations 6.7 and 6.8 are coupled by u_s^* and θ. An appropriate form for u_s^* comes from the analytical solution for a translating fluid sphere (108),

$$u_s^* = -2\sum_{n=2}^{\infty} B_n \frac{\mathcal{C}_n^{-\frac{1}{2}}(\eta)}{sin\phi} + \frac{1}{2} sin\phi \tag{6.9}$$

where $\mathcal{C}_n^{\frac{1}{2}}$ are Gegenbauer polynomials of order n and index $-\frac{1}{2}$, B_n are constants to be determined and $\eta = cos\phi$. The surface coverage θ is to be represented as a Fourier-Legendre series, $\Gamma = \sum_{m=0}^{\infty} A_m \mathcal{P}_m(\eta)$ where A_m are constants to be determined and $\mathcal{P}_m$ are Legendre polynomials of order m (36).

Taking the expressions for $u_s^*(\phi)$ and $\theta(\phi)$ above and inserting into eqs. 6.7 and 6.8 leads to two coupled infinite series equations. The surface mass balance becomes

$$\begin{aligned}
\sum_{m=0}^{\infty} \frac{A_m(m+1)}{sin\phi} \left[\mathcal{P}_{m+1}(\eta) - \eta\mathcal{P}_m(\eta)\right] \left[\frac{1}{2} sin\phi - 2\sum_{n=2}^{\infty} B_n \frac{\mathcal{C}_n^{-\frac{1}{2}}(\eta)}{sin\phi}\right] + ... \\
\sum_{m=0}^{\infty} A_m \mathcal{P}_m(\eta) \left[\eta - 2\sum_{n=2}^{\infty} B_n \mathcal{P}_{n-1}(\eta)\right] - ... \\
\frac{1}{Pe_s^* sin\phi} \left[\sum_{m=0}^{\infty} \frac{A_m(m+1)}{sin\phi} (\mathcal{P}_{m+1} - \eta\mathcal{P}_m)(\eta - 1)\right] + ... \\
\frac{1}{Pe_s^* sin\phi} \left[\sum_{m=0}^{\infty} A_m(m+1) \left(sin\phi\mathcal{P}_m - \frac{m+1}{sin\phi}(\eta\mathcal{P}_{m+1} - \mathcal{P}_m) + \frac{(m+1)\eta}{sin\phi}(\mathcal{P}_{m+1} - \eta\mathcal{P}_m)\right)\right] = ... \\
Bi_\beta^* \left(1 - \sum_{m=0}^{\infty} A_m \mathcal{P}_m(\eta)\right) - Bi_\alpha^* \sum_{m=0}^{\infty} A_m \mathcal{P}_m(\eta) \exp\left[-\Lambda \sum_{m=0}^{\infty} A_m \mathcal{P}_m(\eta)\right].
\end{aligned} \tag{6.10}$$

For the tangential stress balance, the $(1-\theta)^{-1}$ term in eq. 6.7 will approach infinity as $\theta \to 1$, making the equation stiff for some situations. Multiplying both sides by $(1-\theta)$ removes these large values from the right-hand side and makes values on the left-hand side smaller as $\theta \to 1$, relieving this issue. Thus the tangential stress balance becomes

$$\left(1-\sum_{m=0}^{\infty}A_m\mathcal{P}_m(\eta)\right)\left[-\frac{3}{2}\xi sin\phi+(1+\xi)\sum_{n=2}^{\infty}B_n(4n-2)\frac{\mathcal{C}_n^{-\frac{1}{2}}(\eta)}{sin\phi}\right]=...$$
$$nMa\left[1-\left(1-\sum_{m=0}^{\infty}A_m\mathcal{P}_m(\eta)\right)\Lambda\sum_{m=0}^{\infty}A_m\mathcal{P}_m(\eta)\right]\sum_{m=0}^{\infty}\frac{A_m(m+1)}{sin\phi}\left[\mathcal{P}_{m+1}(\eta)-\eta\mathcal{P}_m(\eta)\right].$$
(6.11)

The problem now becomes solving for the constants A_m and B_n in eqs. 6.10 and 6.11. If the infinite series are truncated so that we consider M values of A_m and N values of B_n, eqs. 6.10 and 6.11 can be solved numerically with a collocation method (36). With $M+N$ unknowns and two equations we need to solve eqs. 6.10 and 6.11 at $I=\frac{1}{2}(M+N)$ equally spaced collocation points ϕ_i about the drop surface from $0<\phi_i<\pi$. The resulting system of equations is solved with a Newton-Raphson solver:

$$\begin{bmatrix}A_m\\B_n\end{bmatrix}_{new}=\begin{bmatrix}A_m\\B_n\end{bmatrix}-\left(\frac{\partial[G_{m,n,i},H_{m,n,i}]}{\partial[A_m,B_n]}\right)^{-1}\begin{bmatrix}G_{m,n,i}\\H_{m,n,i}\end{bmatrix},\tag{6.12}$$

where G and H represent the residuals of the mass balance and tangential stress balance, respectively. Residual here is defined by taking all terms in eqs. 6.10 and 6.11 and moving them to the left-hand side, and calling the right-hand side the residual which will approach zero while converging to a solution. The Newton-Raphson solver requires derivatives or both eq. 6.10 and 6.11 with respect to A_m and B_n.

In the absence of a previous set of A_m and B_n, an initial guess is made by taking $Ma^*\to 0$ and using a single collocation point at $\phi_1=\frac{1}{2}\pi$. This gives $A_0=0$ and $B_2=\frac{\xi}{2(1+\xi)}$. Then a large but finite Ma^* is chosen, a new collocation point is added where $A_M=A_{M-1}$ and $B_N=B_{N-1}$, and new A_m and B_n are determined with the Newton-Raphson solver. Additional collocation points are added until three convergence criteria are met. First convergence of B_2 is checked:

$$\frac{|B_2(I) - B_2(I-1)|}{B_2(I-1)} < 10^{-6}. \tag{6.13}$$

If this is satisfied then profiles of $u_s^*(\phi)$ and $\theta(\phi)$ are generated for J points ϕ_j along the drop surface. The maximum change in $u_{s,j}^*(I)$ and $u_{s,j}^*(I-1)$, and in $\theta_j(I)$ and $\theta_j(I-1)$ is checked:

$$\max\left[\frac{|u_{s,j}^*(I) - u_{s,j}^*(I-1)|}{u_{s,j}^*(I-1)}\right] < 10^{-6}, \tag{6.14}$$

$$\max\left[\frac{|\theta_j(I) - \theta_j(I-1)|}{\theta_j(I-1)}\right] < 10^{-6}. \tag{6.15}$$

If the above three criteria are met then a solution is reached. With the constants now determined, the drag force experienced by the drop can be expressed $F_d = 4\pi\mu_o bU(1+B_2)$. This is compared to the drag experienced by a surfactant-free drop $F_d = 2\pi\mu_o bU_{HR}\frac{2+3\xi}{1+\xi}$. For both a clean drop and a surfactant-laden drop of equal size, density and viscosity falling through the same continuous phase, their drag must be equal. Thus equating the two drag expressions the ratio of velocities can be determined,

$$\frac{U}{U_{HR}} = \left(\frac{1}{1+B_2}\right)\frac{1+\frac{3}{2}\xi}{1+\xi}. \tag{6.16}$$

As mentioned earlier this analytical approach will become stiff for small Bi_α^*, small $K_{eq}C_i$ and large Pe_s^*. This situation corresponds to the stagnant cap regime where sharp gradients in Γ develop. Because Γ is represented as an infinite series of Legendre polynomials, the increasingly sharp gradient in Γ requires more terms in the series before being truncated to satisfactorily represent the surfactant concentration profile. This results in a need for an increasing number of collocation points and increasingly better initial guesses for A_m and B_n. Because of the matrix inversion in the Newton-Raphson method this causes the analytical

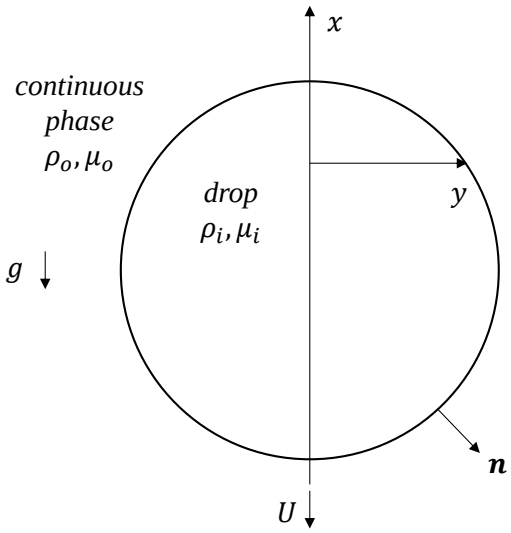

Figure 6.2 *The coordinate system used in the boundary element approach.*

approach to become very computationally expensive, and so for cases where Bi^*_α and $K_{eq}C_i$ are small and Pe^*_s is large a boundary element approach will be used as described in the next subsection.

6.2.4 *Boundary element approach*

As stated above the analytical approach becomes mathematically stiff for small Bi^*_α and $K_{eq}C_i$ and large Pe^*_s. In an alternative approach to solving the coupled mass transfer and fluid dynamics problem we will use the boundary element method. The coordinate system used here will be cylindrical-polar as in Fig. 6.2. The x-coordinate is now the vertical coordinate and the y-coordinate is the perpendicular distance from the drop axis of symmetry to the drop surface. Applied to Stokes flow, this method considers a singularly forced flow like

$$\boldsymbol{\nabla} p = \mu \nabla^2 \boldsymbol{u} + \boldsymbol{b}\delta(\boldsymbol{x} - \boldsymbol{x}_o) \tag{6.17}$$

where $\boldsymbol{b}$ is the arbitrary magnitude of the force applied at the point $\boldsymbol{x}_o = (y_o, x_o)$. The resulting velocity and stress fields at the point $\boldsymbol{x} = (y, x)$ are

$$u_i(\boldsymbol{x}) = \frac{1}{8\pi\mu}\boldsymbol{G}_{ij}(\boldsymbol{x}, \boldsymbol{x}_o)b_j \tag{6.18}$$

and

$$\sigma_{ik}(\boldsymbol{x}) = \frac{1}{8\pi}\boldsymbol{T}_{ijk}(\boldsymbol{x}, \boldsymbol{x}_o)b_j \tag{6.19}$$

where $\boldsymbol{G}_{ij}$ and $\boldsymbol{T}_{ijk}$ are velocity and stress Green's functions, respectively (107). The Green's functions depend on the flow domain and for a number of special cases the correct forms can be found in the literature (107). Green's functions for an axisymmetric body in an unbounded domain can be found in the appendix.

The boundary element method uses the above singularly forced flow along with the Lorentz reciprocal relation $\nabla \cdot (\boldsymbol{u}^{(1)} \cdot \boldsymbol{\sigma}^{(2)} - \boldsymbol{u}^{(2)} \cdot \boldsymbol{\sigma}^{(1)}) = 0$ where the flow (1) is the singularly forced flow and flow (2) is an unrelated Newtonian Stokes flow. After some rearranging (107), the boundary integral equation describing the axisymmetric surfactant-laden buoyancy-driven drop is

$$\begin{aligned}\boldsymbol{u}(\boldsymbol{x}_o) = &-\frac{1}{4\pi\mu_o(1-\xi)}\int_C \boldsymbol{G}(\boldsymbol{x}, \boldsymbol{x}_o)\Delta\boldsymbol{f}(\boldsymbol{x})d\ell(\boldsymbol{x}) + ... \\ &\frac{1-\xi}{4\pi(1+\xi)}\left[\int_C^{PV}\left[\boldsymbol{u}(\boldsymbol{x}) - \boldsymbol{u}(\boldsymbol{x}_o)\right]\boldsymbol{T}(\boldsymbol{x}, \boldsymbol{x}_o)\boldsymbol{n}d\ell(\boldsymbol{x}) - 4\pi\boldsymbol{u}(\boldsymbol{x}_o)\right]\end{aligned} \tag{6.20}$$

where $\Delta\boldsymbol{f}$ is the jump in traction across the surface and C is the drop surface. The "PV" in the second integral indicates the principal value. The jump in traction comes from eq. 6.3. The integral equation contains two integrals. The first integral on the right-hand side is commonly called the single layer potential and represents a distribution of point forces

associated with the velocity Green's function distributed about the drop surface. The second integral is called the double layer potential and represents a distribution of point source and point force dipoles (107).

In contrast to the analytical approach, the velocity for the boundary element approach is scaled like $\boldsymbol{u}' = \boldsymbol{u}\frac{\mu_o}{\Delta\rho g b^2}$ where the apostrophe is used to differentiate it from the analytical dimensionless velocity. Note that the dimensionless terminal velocity $U' = \frac{Ca^*}{Bo^*}$ where $Ca^* = \frac{\mu_o U}{\gamma}$ and $Bo^* = \frac{\Delta\rho g b^2}{\gamma}$. Correspondingly the time is scaled like $t' = t\frac{\Delta\rho g b}{\mu_o}$. Otherwise the length scale is the radius b and the concentration scale is the maximum surface concentration Γ_∞.

The jump in traction is determined from both the normal and tangential components of the interfacial stress equation. When non-dimensionalized this becomes

$$\Delta\boldsymbol{f}^* = ... \\ nMa^*U' \left[\left(\frac{1}{1-\theta} - \Lambda\theta\right)\boldsymbol{\nabla}_s^*\theta + 2\kappa^*\left(\frac{E_0^*}{n} + \ln(1-\theta) + \frac{1}{2}\Lambda\theta^2\right)\boldsymbol{n} + \frac{1}{nMa^*U'}x^*\boldsymbol{n}\right] \tag{6.21}$$

where Ma^* is the Marangoni number as defined in the analytical approach and $E_0^* = \frac{\gamma_0}{\hat{R}T\Gamma_\infty}$ is the zero-coverage elasticity number. Aside from the additional U' multiplying Ma^* due to the difference in scaling, the major difference between the boundary element and analytical approaches is the boundary element approach allows the drop to deform. The incorporation of normal stresses results in the new parameter E_0^*.

The first integral on the right-hand side of eq. 6.21 unfortunately exhibits a singularity of the form $-2\ln|\boldsymbol{x} - \boldsymbol{x}_o|$ and thus requires some manipulation prior to integration (107). The singularity is typically handled by subtracting it from the original integral and then integrating the singularity separately. Details about how the singularity is handled can be found in the appendix. The second integral is weakly singular but the singularity can be removed by writing

$$\int_C^{PV} T_{ijk}(\boldsymbol{x},\boldsymbol{x}_o)u_j(\boldsymbol{x})n_k(\boldsymbol{x})d\ell(\boldsymbol{x}) = ...$$

$$\int_C^{PV} \Big[T_{ixk}(\boldsymbol{x},\boldsymbol{x}_o)\left[u_x(\boldsymbol{x})-u_x(\boldsymbol{x}_o)\right] + T_{iyk}(\boldsymbol{x},\boldsymbol{x}_o)u_y(\boldsymbol{x}) - ... \tag{6.22}$$

$$P_{ik}(\boldsymbol{x},\boldsymbol{x}_o)u_y(\boldsymbol{x}_o)\Big]n_k(\boldsymbol{x})d\ell(\boldsymbol{x}) - 4\pi\delta_{ix}u_x(\boldsymbol{x}_o) - 4\pi\delta_{iy}u_y(\boldsymbol{x}_o)$$

where $\boldsymbol{P}$ is a new tensor detailed in the appendix (107).

The solution method for the boundary element approach begins with first discretizing the drop into I boundary elements and $I+1$ nodes. The elements are defined by periodic cubic splines which is detailed in the appendix. As a natural result of the cubic splines first order accurate approximations of the surface normals and second order accurate approximations of the surface curvature are found. However it is assumed that the drops will remain spherical so exact values for the curvature and normals are used.

The solution is initialized by using θ_{eq} as prescribed by the Frumkin isotherm and u_s^* from the analytical Hadamard-Rybczynski solution. Then the jump in traction $\Delta\boldsymbol{f}$ is determined at each node. The jump in traction in the single layer potential integral is decoupled from the velocity Green's function as described in the appendix and integrated separately. The jump in traction is integrated over each cubic spline boundary element using Gauss-Legendre quadrature.

The velocity Green's functions are then integrated over each cubic spline element while handling the singularity as discussed in the appendix. Since the velocity Green's functions only require information about the geometry and we assuming the drop will remain a sphere, these only need to be calculated once and are saved for future iterations. This is likewise true of the stress Green's functions and additional tensor $\boldsymbol{P}$. The double layer potential integral is then integrated over each element using the initial guess of u_s^*. The result is a new surface velocity profile $\boldsymbol{u}(\boldsymbol{x}_o)$ at each node on the drop. The method of successive substitutions is

thus used to converge on the final surface velocity profile dictated by the jump in traction over the drop surface (109).

Following a converged solution for the velocity profile over the drop surface, the surface convection-diffusion equation eq. 6.5 is integrated over a single time step $\Delta t^{'}$ to update the surface concentration profile. This time does not have a physical meaning since the analysis is not equipped to handle transient solutions. This integration in time is needed only to develop the surface concentration and velocity profiles until a converged solution is found. The time derivative is approximated using a fourth-order Runge-Kutta-Merson scheme. Then the kinematic condition is used to advance the nodes defining the drop surface: $d\boldsymbol{x}_o^*/dt^* = \boldsymbol{u}^*(\boldsymbol{x}_o^*)$. This time derivative is also approximated using a fourth-order Runge-Kutta-Merson scheme. Because the drop is assumed to remain a sphere, this step only serves to determine the translational velocity of the drop $U^{'}$. The distance between the centroids of the original and advanced drop profile after $\Delta t^{'}$ is used to determine the translational velocity. The advanced drop profile is then disregarded and the original spherical profile is retained for future iterations.

With the new surface concentration profile the jump in traction is updated and the processes continues until an equilibrium is reached. An equilibrium is determined when two criteria are met:

$$\frac{1}{\Delta t^{'}(I+1)}\left[\sum(\theta_{i,n}-\theta_{i,n-1})^2\right]^{\frac{1}{2}} < 10^{-6} \tag{6.23}$$

and

$$\frac{1}{\Delta t^{'}(I+1)}\left[\sum(u^*_{s_{i,n}}-u^*_{s_{i,n-1}})^2\right]^{\frac{1}{2}} < 10^{-6} \tag{6.24}$$

where n is the current solution and $n-1$ is the previous solution. Due to the scaling for the boundary element approach, the dimensional terminal velocity scaled by the Hadamard-Rybczynski solution is given by

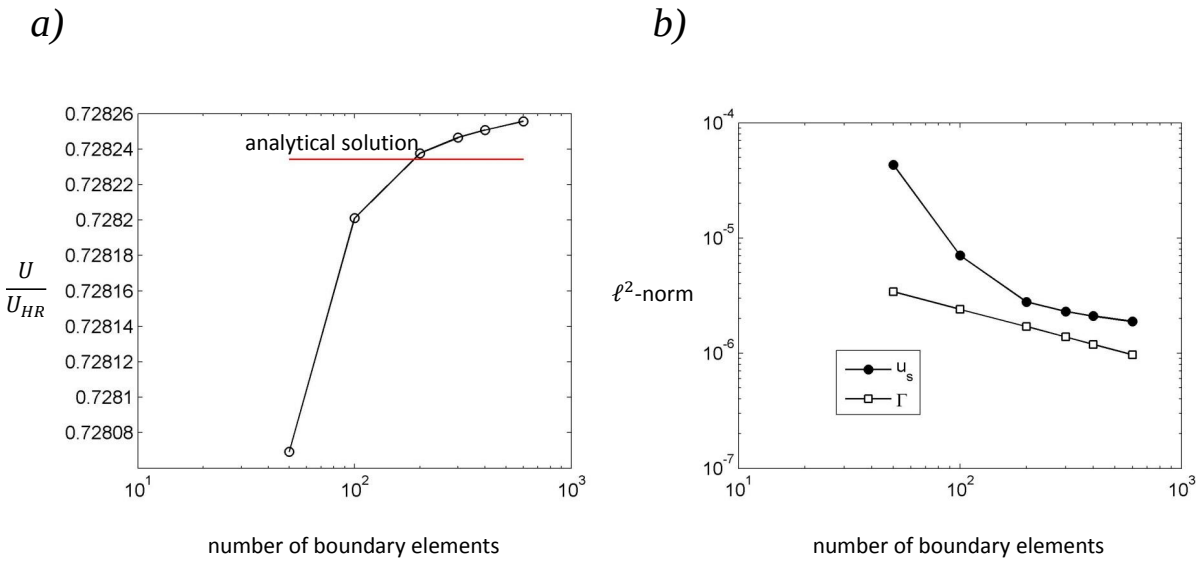

Figure 6.3 *Comparisons between the a) translational velocities and b) surface velocity and surface concentration profiles between the analytical and boundary element method for* $Bi^*_\beta = 1$, $Bi^*_\alpha = 1$, $Pe^*_s \to \infty$, $Ma^* = 10$ *and* $\xi = 0.1$.

$$\frac{U}{U_{HR}} = U' \frac{3}{2} \left(\frac{2 + 3\xi}{1 + \xi} \right). \tag{6.25}$$

Before continuing the boundary element approach should be validated. To do this the case where $Bi^*_\beta = 1$, $Bi^*_\alpha = 1$, $Pe^*_s \to \infty$, $Ma^* = 10$ and $\xi = 0.1$ is considered. This case would not result in appreciable deformation in the boundary element method. In Fig. 6.3(a) the terminal velocity normalized by the Hadamard-Rybczynski solution using the boundary element method is plotted versus the number of boundary elements. The analytical solution

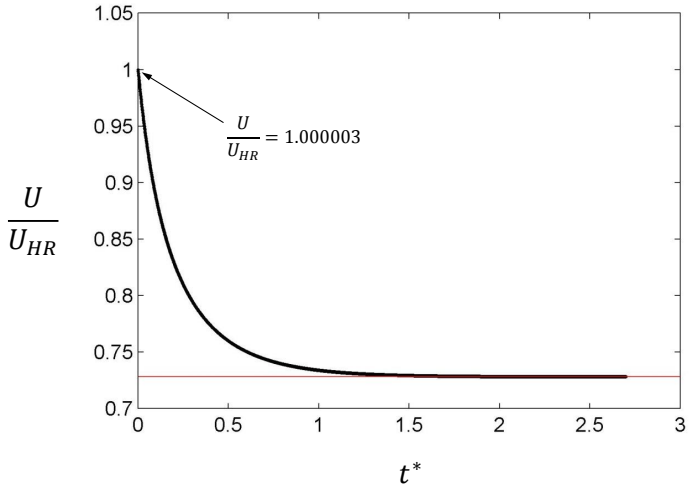

Figure 6.4 *Comparing the translational velocities when initializing with θ_{eq} as prescribed by the Frumkin isotherm (thin line) and when initializing with $\theta = 0$ (thick line) for $Bi^*_\beta = 1$, $Bi^*_\alpha = 1$, $Pe^*_s \to \infty$, $Ma^* = 10$ and $\xi = 0.1$.*

is also shown as the horizontal line. In Fig. 6.3(b) the ℓ^2-norm between the resulting surface velocity and surface concentration profiles is also shown. Agreement between the two methods is excellent, and increasing the number of elements improves the agreement. The small differences in terminal velocity at a high number of boundary elements may be due to the presence of an albeit very small normal velocity in the boundary element method. The number of boundary elements is fixed to $I = 200$ for the solutions later in this chapter.

To determine if the initial condition has an effect on the final solution, this same case is initialized two ways using the boundary element method. The first method is the same as described above where θ_{eq} according to the Frumkin isotherm is the initial surface concentration. In the second method the surface initially has no surfactant i.e. $\theta = 0$. Figure 6.4 compares the two. The thin horizontal line in Fig. 6.4 is the final solution when initializing with θ_{eq} and the thick black line shows the velocity initialized with $\theta = 0$ versus $t^{'}$. When initialized with $\theta = 0$ the drop velocity begins at $0.000003U_{HR}$ showing good agreement with

the Hadamard-Rybczynski solution which is valid for $\theta = 0$. Eventually an equilibrium is found which is identical to the case when initializing with θ_{eq}.

6.2.5 *Theoretical results - Surface diffusion effects on terminal velocities*

There has been a lot of theoretical work on the surfactant-laden buoyancy-driven drop problem. In ref. (35) the effects of surface diffusion (finite Pe_s^*) and surface convection were considered but without sorption kinetics, while in ref. (36) sorption kinetics and surface convection were considered but surface diffusion was neglected ($Pe_s^* \to \infty$). Here we will consider how finite Pe_s^* can impact the drag a surfactant-laden drop experiences without neglecting surface convection of sorption kinetics.

When considering surface diffusion, surface convection and sorption kinetics the problem has four independent parameters that will affect the drag and terminal velocity: Ma^*, Bi_α^*, Pe_s^* and the quantity $K_{eq}C_i$. Note that $K_{eq}C_i = Bi_\beta^*/Bi_\alpha^*$. Figure 6.5 shows how combinations of these four parameters affect drop velocities. All of the results in Fig. 6.5 were generated using the analytical approach and $\xi = 0.001$. The figure is composed of 9 individual plots. Each individual plot has Pe_s^* on the horizontal axis and Bi_α^* on the vertical. The individual plots themselves are contour plots of the drop velocity normalized by the Hadamard-Rybczynski velocity U_{HR}. The isolines represent the values annotated on each plot and range from 0.7 to 0.95. Then each row of individual plots has a constant Ma^* indicated on the far left of the figure, and each column of individual plots has a constant $K_{eq}C_i$ indicated at the very top of the figure. The $K_{eq}C_i$ values of 0.1, 1.0 and 10 correspond to SDS concentrations of 0.065, 0.65 and 6.5 mM, respectively, when using the K_{eq} for SDS in 1000 cSt Si oil from chapter 4. When using the K_{eq} for SDS in heavy mineral oil, $K_{eq}C_i$ values of 0.1, 1.0 and 10 correspond to 0.014, 0.14 and 1.4 mM, respectively.

Figure 6.5 clearly shows that Pe_s^* can affect drop velocities depending on the values of the other three parameters. To aid in the discussion of Fig. 6.5 the contour plot corresponding to $Ma^* = 10$ and $K_{eq}C_i = 10$ (top right) has been annotated. Four regions have

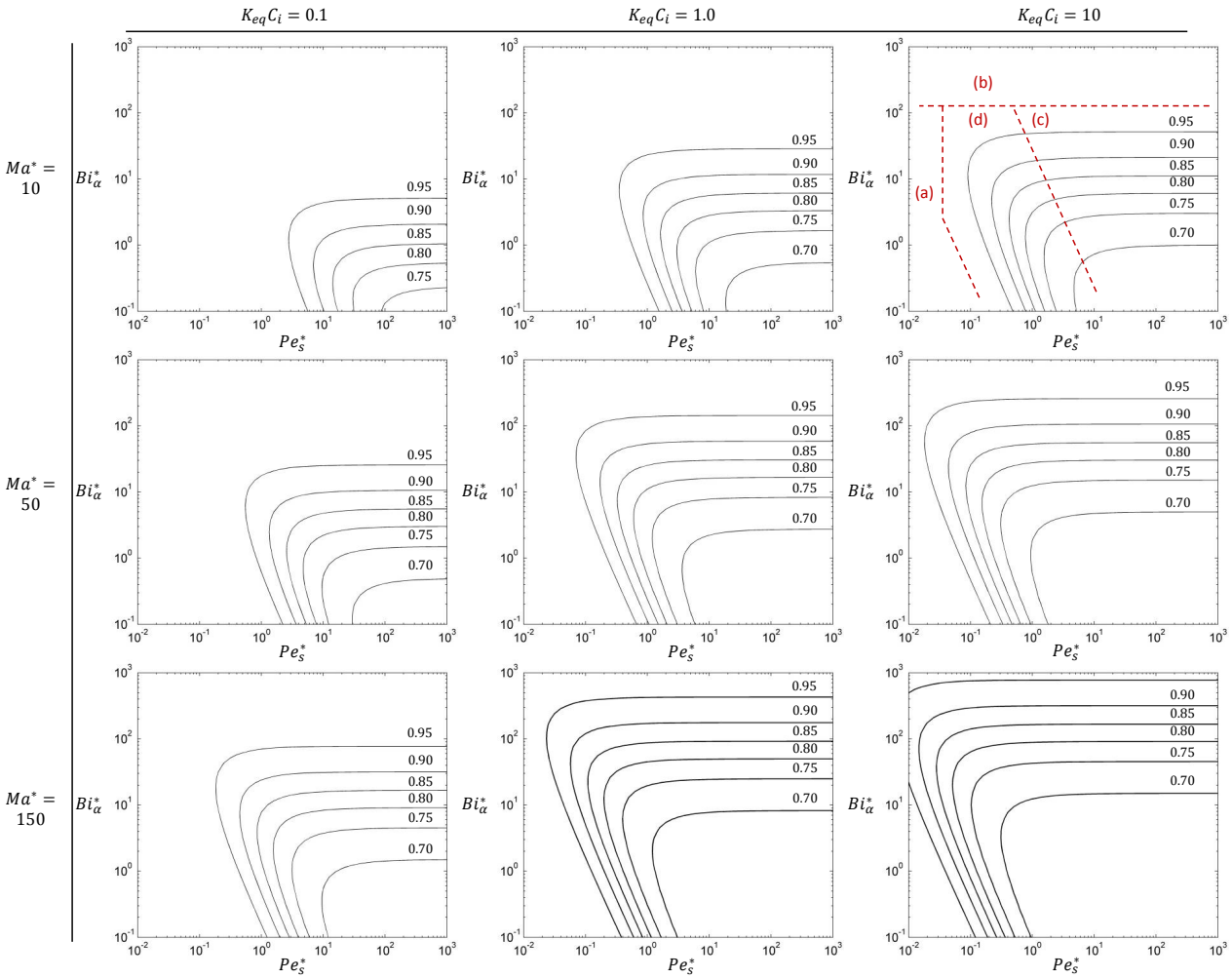

Figure 6.5 *Contour plots of U/U_{HR} are shown where the level of each isoline is annotated on each plot. For each of the nine contour plots the horizontal axis is the surface Peclet number Pe^*_s and the vertical axis is the desorption Biot number Bi^*_α. Each row of contour plots has a constant Ma^* indicated on the left-hand side of the figure and each column of contour plots has a constant $K_{eq}C_i$ indicated on the top of the figure. The viscosity ratio is fixed at $\xi = 0.001$. For the contour plot corresponding to $Ma^* = 10$ and $K_{eq}C_i = 10$ four regions are roughly defined by dotted lines. These regions are discussed in the text.*

been roughly defined by the dashed lines and are labeled (a)-(d). In regions (a) and (b) the velocity of the drop is nearly unaffected by the presence of surfactants in the system where velocities are between $0.95U_{HR}$ and $1.0U_{HR}$. In region (a) the primary reason for the negligible impact of surfactants is the low Pe_s^*. Here surface diffusion is so dominant that surface surfactant concentration gradients, and therefore surface tension gradients, cannot develop. In region (b) the primary reason for the negligible impact of surfactants is the large Bi_α^* where desorption rates are so relatively large that surfactant is not able to remain on the surface in order to develop concentration gradients. For the range of Ma^* and $K_{eq}C_i$ shown the leftmost boundary between regions (a) and (d) occurs when Pe_s^* is between O(0.001) and O(1). Note that the contour plot for $Ma^* = 150$ and $K_{eq}C_i = 10$ is cut off on the left side. The lower boundary of region (b) begins when Bi_α^* are between O(10) and O(1000) and larger.

The other two regions in the annotated plot in Fig. 6.5 include reductions in the drop velocity relative to U_{HR}. In region (c) the drop velocities can fall between about $0.67U_{HR}$ and $0.95U_{HR}$ due to the development of surfactant concentration and surface tension gradients on the drop surface. The relative velocities in this region, though, are roughly unaffected by changing Pe_s^*. The isolines in this region are essentially horizontal lines and the relative velocities change only when Ma^*, $K_{eq}C_i$ or Bi_α^* change. Therefore when combinations of Ma^*, $K_{eq}C_i$ and Bi_α^* fall within region (c) surface diffusion effects on the terminal velocity of the drop can be neglected. The left boundary of this region is diagonal as shown in the figure. For the range of Ma^* and $K_{eq}C_i$ shown the top left corner of region (c) begins at the boundary of region (b) and Pe_s^* between O(0.1) and O(10). The boundary of region (c) then follows a diagonal down and to the right.

Region (d) in Fig. 6.5 is the most complicated region and does indicate that changes in Pe_s^* will impact the terminal velocity of the drop. This region is bounded by regions (a), (b) and (c) and follows diagonally down and to the right between regions (a) and (c). In this region surface diffusion is strong enough to reduce surfactant and surface tension

gradients, but large enough surface tension gradients exist to impact the drop velocity. What is particularly interesting about this region is that, for a roughly fixed Pe_s^*, Ma^* and K_{eq}, moving vertically upward in the region beginning with a low Bi_α^* can result in relative velocities that decrease and then increase. This is in contrast to region (c) where, for a roughly fixed Pe_s^*, Ma^* and K_{eq}, moving vertically upward will always increase the relative velocity.

In the next section the experimental materials and procedure will be discussed followed by some experimental results, some of which fit within region (d) in Fig. 6.5. Afterward predicted drag coefficients using the sorption kinetics from chapter 4 will be generated using either the analytical or boundary element approach followed by a comparison with the experimental drag coefficients.

6.3 Experimental section

6.3.1 *Experimental materials and procedure*

Choosing appropriate liquids and materials for an experimental buoyancy-driven surfactant-laden drop analysis is not trivial. Based on the analysis presented in the previous sections the experiments must follow certain rules. First the ability to observe drops translating at low Re^* is important so that Stokes flow can be assumed. Second the drop phase and continuous phases should be immiscible so that a discernible surface forms between the two fluids and no mass from either phase gets lost to the other by diffusion or convection. Next because the adsorption model to be used assumes only one surfactant is present and it is only soluble in one phase the experimental materials should be chosen accordingly. The drop phase is chosen to be aqueous and will contain the surfactant, so that means the surfactant should be insoluble in the continuous phase and also the continuous phase should not contain any additional surfactants. For example this excludes vegetable oils such as castor oil which contain long-chain fatty acids which are surface-active.

Table 6.1 *Experimental liquid properties.*

	water	heavy mineral oil	1000 cSt Si oil
ρ [g cm^{-3}]	1.00	0.900	0.980
μ [mPa· s]	1.0	171	990

The surfactant chosen for the aqueous (deionized water (Fisher)) drop phase had to be done carefully. In the above analysis C_s was assumed constant and thus $C_s = C_i$. This means depletion in the bulk as discussed in chapter 3 could not occur. This excluded the use of tetraethylene glycol monododecyl ether ($C_{12}E_4$) and similar surfactants in experiments. Additionally hexadecyltrimethylammonium bromide (CTAB) was shown to have very slow sorption kinetics in chapter 4 where equilibrium surface tension values could take over 16 hours to reach. This may require long experimental times (long settling distances) for a balance between surface convection and adsorption to be reached. Therefore CTAB was excluded as well. Finally it was found that sodium oleate (SO) had a strong tendency to form different phases in solution after aging for relatively short amounts of time. While the exact cause for this is unknown, it made the use of SO difficult in practice for experiments as sensitive as these. The chosen surfactant for these experiments is >99% sodium dodecyl sulphate (SDS) (Fisher). Based on the analyses in chapters 2, 3 and 4, this surfactant would not result in depletion in the drop phase and the adsorption and desorption rates were satisfactorily estimated. The surfactant concentrations will be as high as the critical micelle concentration (CMC) for SDS which is about 8 mM (57).

The chosen continuous phases required some trial and error. Initially light mineral oil (Fisher) was chosen, but the viscosity was too low to keep Re^* small for a sufficient range of drop volumes. Instead two other continuous phase liquids were chosen: heavy mineral oil (paraffin oil) (Fisher) and 1000 cSt silicone (Si) oil (Clearco). The important properties of each continuous phase liquid as well as the properties of water are summarized in table 6.1.

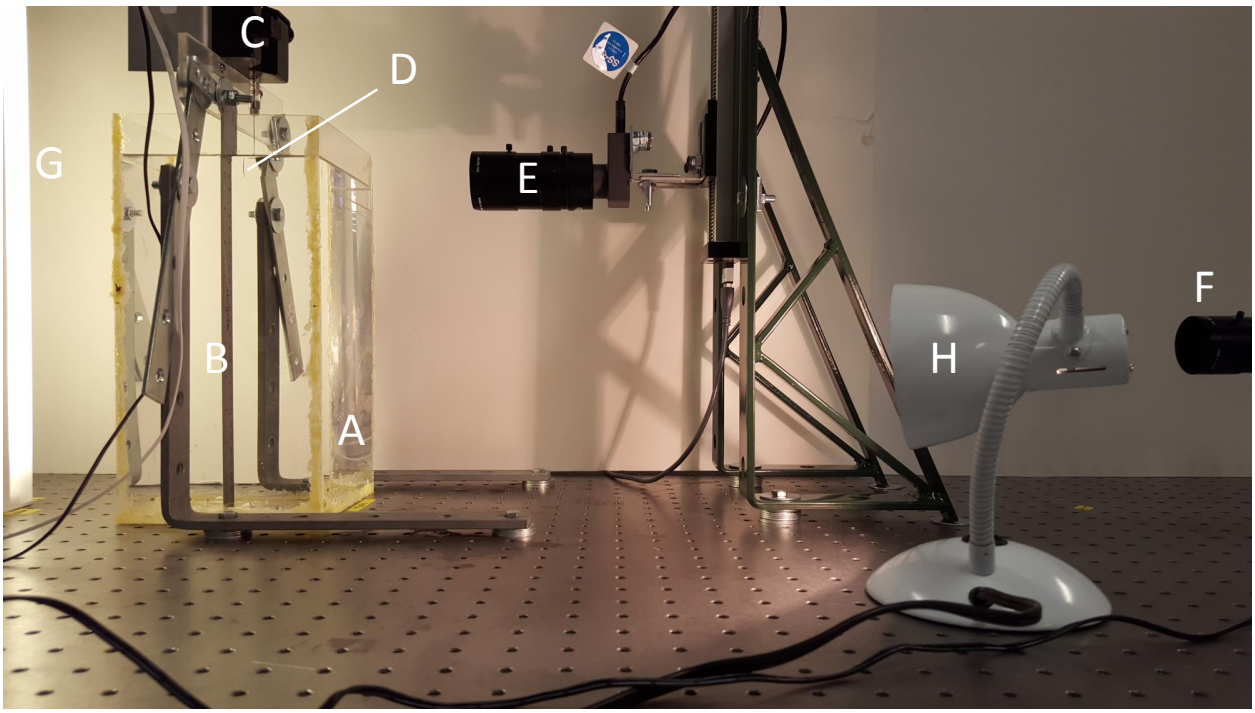

Figure 6.6 *The setup for settling drop experiments consisting of a) the acrylic tank, b) a ruler, c) a syringe pump with a loaded syringe, d) the drop, e) a CCD camera, f) another CCD camera, g) a lamp to illuminate experiments, and h) a lamp to illuminate the ruler.*

As will be evident in the results section, it is suspected that something in the mineral oil is slightly surface active.

Also an issue with the 1000 cSt Si oil was encountered after performing experiments over several days. After several days of aqueous drops containing SDS falling in the Si oil it was observed that the oil started to become slightly cloudy. While it is unclear what the cause was, one possible explanation is that over time very fine droplets (micro-emulsion) have accumulated in the tank which could diffuse throughout. No drop breakup or deformation was observed while drops settled but these droplets could be too small to observe without a microscope. Experiments of 300 μl drops falling in 1000 cSt Si oil were performed just as the cloudiness started to be apparent. These were therefore the last set of experiments performed since it would be unclear what effect the cloudiness would have on experiments. In Fig. 6.7 for two of these 300 μl drops particulates can be seen streaming from the rear of both a 0.01 and 8 mM SDS drop. The fact that the tail appears for 0.01 mM SDS drops where the surface tension does not decrease much at the rear would likely rule out any breakup from the drop itself. Regardless these observations limited the number of experiments performed and further demonstrates the difficulty in performing these experiments.

A photo of the experimental setup is shown in Fig. 6.6. The settling drop experiments were performed using an acrylic tank with a 145×145 mm base and 275 mm height which was filled with oil. These dimensions should prevent any wall effects (110). The acrylic contained an antistatic coating to limit any potential triboelectric effects, and the top was covered with another acrylic piece with a small access hole to limit dust and other contaminants from falling in. A ruler was placed along the inside wall of the tank to determine the length scale in experimental images. A syringe pump (New Era Pump Systems) was fixed above the tank. Two CCD cameras (Pixelink) were used. The camera labeled "E" in Fig. 6.6 was used for close-up images of drops where resolutions were between 10 and 50 μm per pixel width. This camera was responsible for determining drop volumes in all experiments and for determining drop velocities in experiments using 1000 cSt Si oil. The other camera labeled

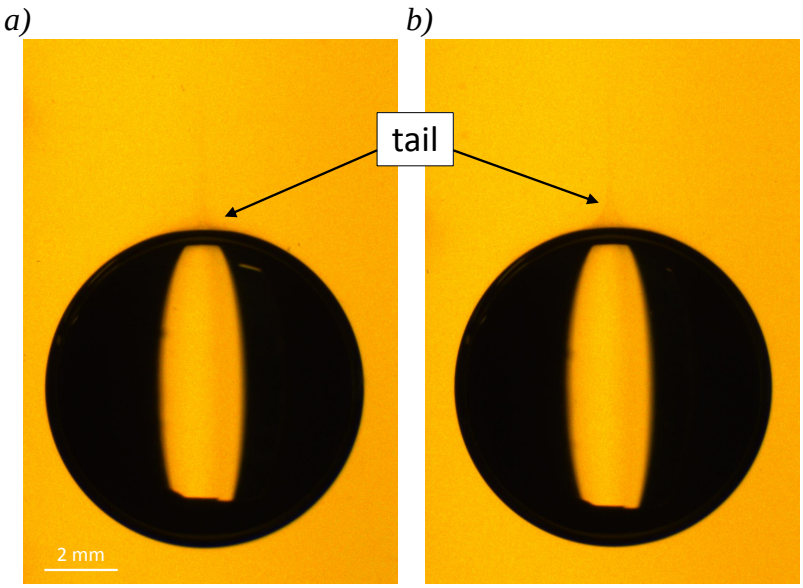

Figure 6.7 *Experimental images of 300 µl drops containing a) 0.01 mM SDS and b) 8 mM SDS falling in 1000 cSt Si oil. The images show particles streaming from the rear of each drop.*

"F" in Fig. 6.6 was used for determining settling drop velocities in experiments using heavy mineral oil. A vertical lamp illuminated drops from behind, and a small lamp labeled with "H" in Fig. 6.6 was used to illuminate the ruler inside the tank.

Placing drops in the tank had to be done mindfully. This was done using one of two methods. In the first the syringe pump was used to dispense a pendant drop from a 100 μl glass syringe (Hamilton) with a certain volume. The pendant drop was left suspended on the syringe needle for 10 minutes, allowing the surface tension to reach an equilibrium according to the experiments from chapter 4. After the 10 minutes the drop was gently detached by tapping the needle. This method was only suitable if drop volumes were not too large and surface tensions were not too low as to cause the drop to detach before 10 minutes.

In the second and more often used method, drops of a desired volume were pipetted into a weighing dish that was filled with either heavy mineral oil or 1000 cSt Si oil as shown in Fig. 6.8(a). Again the drops were left untouched for 10 minutes to allow surfactant adsorption

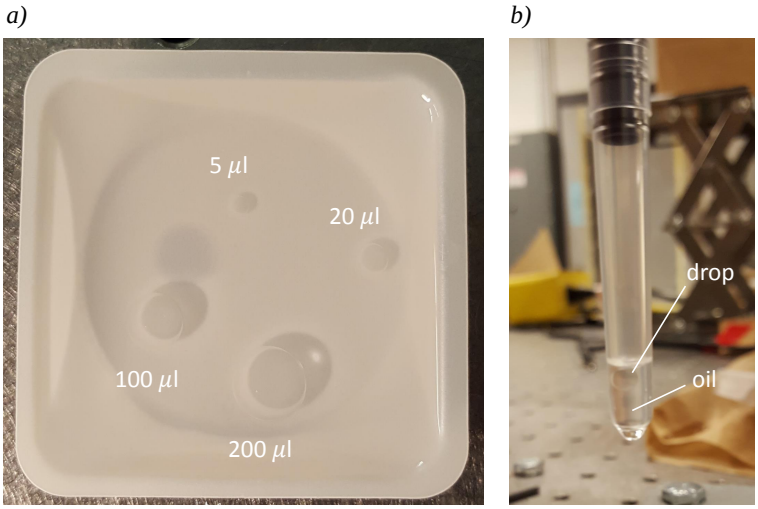

Figure 6.8 *In (a) 4 different sized aqueous drops with 8 mM SDS are submerged in 1000 cSt Si oil. In (b) a 100 μl drop is transported to the tank using a pipette.*

to reach an equilibrium. After 10 minutes a single drop was aspirated along with a small amount of the oil as shown in Fig. 6.8(b). The drop was then dispensed in the acrylic tank.

As the drop began falling in the oil-filled acrylic tank, the close-up camera took several images of the drop to determine the volume and drop radius. Drop volumes ranged from 0.5 to 300 μl in the heavy mineral oil and 5 to 300 μl in the 1000 cSt Si oil. For the 1000 cSt Si oil experiments the close-up camera also was responsible for determining the drop velocity by capturing its position versus time. Drops falling in heavy mineral oil had faster terminal velocities and so the camera situated further from the tank was used to determine the drop velocity. At least 10 sequential images of the drop falling were used to determine its position versus time and thus its velocity. Time intervals between images were then between 1 and 10 seconds depending on the oil and drop volume. A linear best fit of the position versus time data was used to determine the velocity. Terminal velocities were between 0.5 and 35 mm s^{-1} for experiments in heavy mineral oil and between 0.05 and 1 mm s^{-1} in the 1000 cSt Si oil.

6.3.2 *Experimental results*

In Fig. 6.9(a) an example close-up image of a 100 μl drop of 7 mM SDS settling in heavy mineral oil is shown. The exposure time of the camera needed to be long enough to collect enough light to observe the drop. However the drop passed in and out of the frame quickly due to a combination of the drop velocity and zoom of the camera, leaving the top and bottom a little blurry. The distance from the left edge to the right edge of the drop is therefore used to estimate the drop diameter and then volume. In Fig. 6.9(b) a sequence of images of the same drop taken at 1 s intervals using the farther away camera are shown. Each experiment in heavy mineral oil consisted of a collection of images like those in Fig. 6.9. Due to the increased viscosity and density of the Si oil, only one camera was needed to both measure the drop size and drop velocity. In Fig. 6.10 several example experimental images of a 20 μl 8 mM SDS drop settling in 1000 cSt Si oil are shown where the time interval between images is 5 s. The entire sequence of images is not shown. Each 1000 cSt Si oil experiment contained a sequence of images like those shown in Fig. 6.10.

In the analysis section the drag coefficients for a clean drop $C^*_{d,HR}$ and a solid sphere $C^*_{d,St}$ were defined. In the case of a surfactant-laden drop the drag coefficient is not assumed to be known *a priori*. In assigning a drag coefficient to experiments $C^*_{d,exp}$ where surfactant-laden drops translate steadily due to buoyancy the drag force it experiences is still equal to the buoyant force. It follows that the drag coefficient for the experiments can be defined as

$$C^*_{d,exp} = \frac{8}{3}\frac{\Delta\rho g b}{\rho_o U^2}. \tag{6.26}$$

When comparing the experimental drag coefficient $C^*_{d,exp}$ to the Hadamard-Rybczynski drag coefficient $C^*_{d,HR}$, if $C^*_{d,HR}$ is determined using the Re^* from the experiment that produced $C^*_{d,exp}$, then $C^*_{d,HR}/C^*_{d,exp} = U/U_{HR}$ where U is the experimentally measured terminal velocity of the drop. Therefore all $C^*_{d,HR}$ and $C^*_{d,St}$ appearing below are determined using the Re^* from experiments.

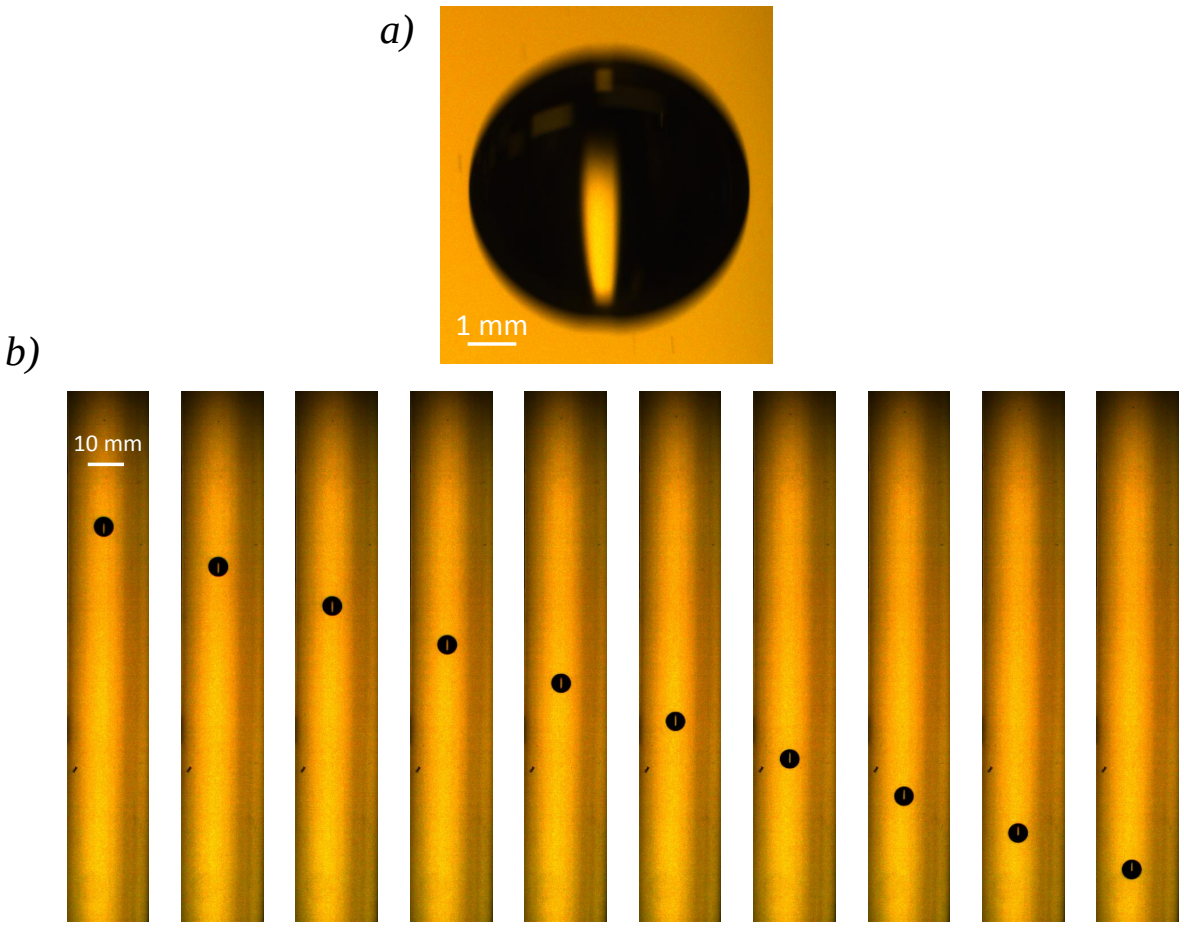

Figure 6.9 *In (a) the close-up view of a 100 µl 8 mM SDS drop falling in heavy mineral oil that is used to determine the drop volume is shown. In (b) an example sequence of images showing the same 100 µl drop settling over time is shown.*

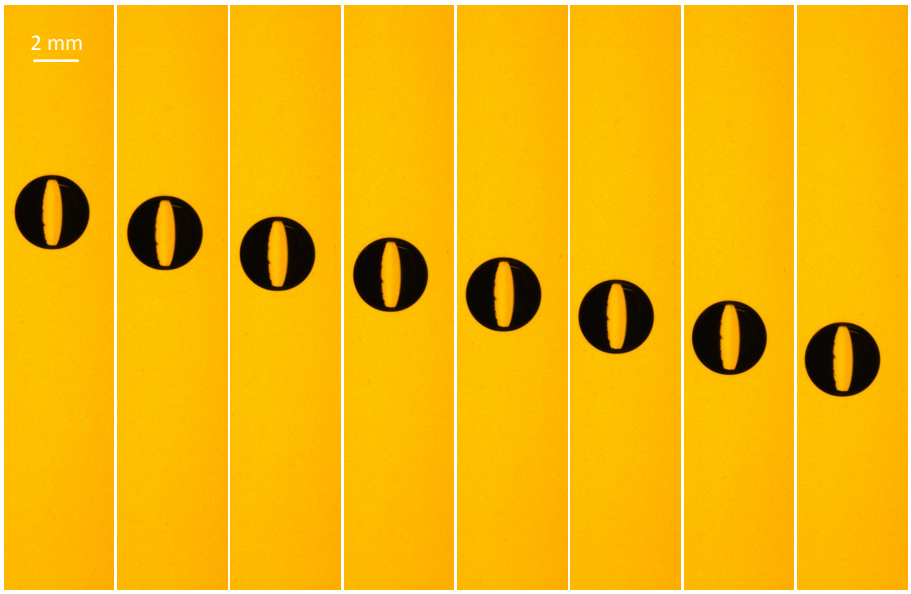

Figure 6.10 *An example sequence of images showing a 20 µl 8 mM drop settling in 1000 cSt Si oil is shown.*

Figure 6.11(a) shows the experimental drag coefficient for drops of water and drops of 8 mM SDS falling in heavy mineral oil. For the 8 mM SDS drops shown, Marangoni numbers, Ma^*, ranged from 112 for the smallest drop (lowest Re^*) to 1.5 for the largest drop. The horizontal axis is the Reynolds number, and the Hadamard-Rybczynski ($C^*_{d,HR}$) and Stokes ($C^*_{d,St}$) drag laws are also shown and the straight solid and dotted lines, respectively. The drag coefficients $C^*_{d,HR}$ and $C^*_{d,St}$ are calculated using the experimental Re^*. This will be true here and elsewhere in the presentation of the results. Figure 6.11(b) contains the same data as in Fig. 6.11(a) but here the drag coefficients are normalized by $C^*_{d,HR}$. Note that $C^*_{d,HR}$ is in the numerator. As $Re^* \to 1$ both the water and 8 mM SDS drops follow $C^*_{d,HR}$. However as Re^* decreases the drag coefficients increase relative to $C^*_{d,HR}$, approaching $C^*_{d,St}$ and indicating solid sphere behavior. This may be expected in the 8 mM SDS drops where the surfactant should introduce Marangoni stress and slow the drop down relative to an

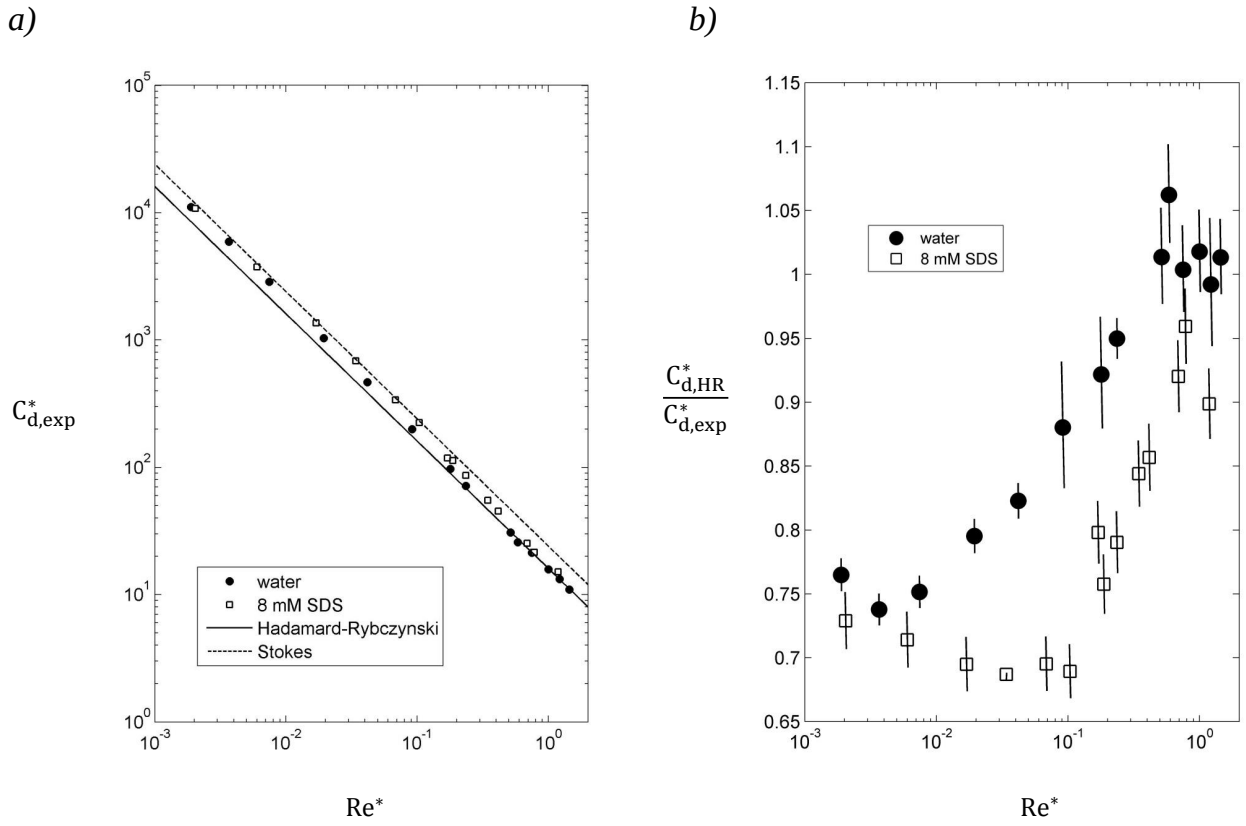

Figure 6.11 *In (a) the drag coefficients for different sized aqueous drops with either no SDS or 8 mM SDS are plotted versus Re*. The upper dashed line represents the Stokes drag coefficient and the lower solid line represents the Hadamard-Rybczynski drag coefficient. In (b) the experimental drag coefficients from (a) are normalized by the Hadamard-Rybczynski drag coefficient to show the transition from the solid sphere regime to the fluid sphere regime. The vertical lines are error bars representing the uncertainty in drop velocity and radius measurements.*

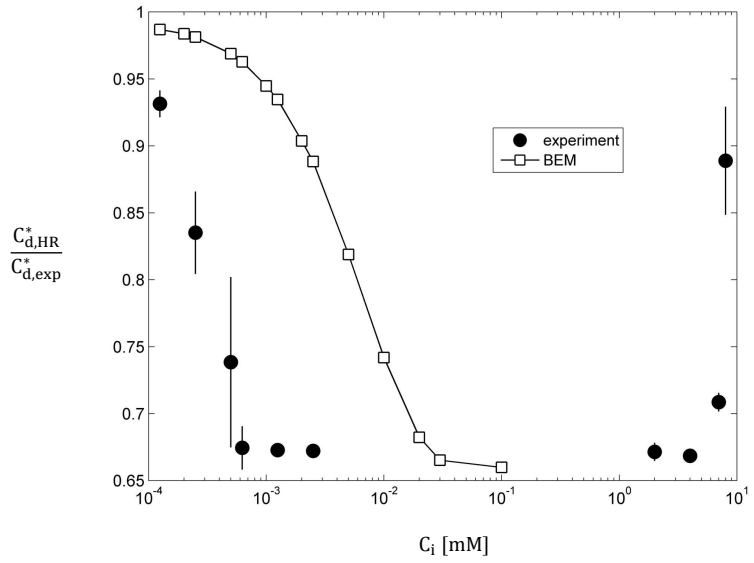

Figure 6.12 *The experimental drag coefficients for 100 μl aqueous drops are plotted versus C_i. The vertical lines are error bars representing uncertainty in drop velocity and size. The predicted drag coefficients using $SDS_{(aq)}$ - heavy mineral oil sorption kinetics and the boundary element method are also shown.*

ideal fluid sphere. The small Ma^* at higher Re^* could explain the remobilization of the drop surface. But this is not expected in the clean water drops. Because the water drops show signs of additional drag at the lower Re^*, it is reasonable to suggest that the heavy mineral oil contains some surface-active components.

Since it is unknown what exactly is causing the increase in drag for smaller clean water drops, those experiments cannot be analyzed using the tools described earlier in this chapter. Additionally as $Re^* \to 1$ and higher the assumption of Stokes flow necessary for the analysis begins to break down. Going forward it was decided to perform additional experiments using 100 μl drops ($Re^* \sim 0.5$) and varying concentrations of SDS since this was the smallest volume at which the Hadamard-Rybczynski velocity was observed for the clean water drops.

In Fig. 6.12 the normalized drag coefficients for 100 μl drops settling in heavy mineral oil are plotted versus the bulk concentration of SDS. Using the adsorption kinetics from

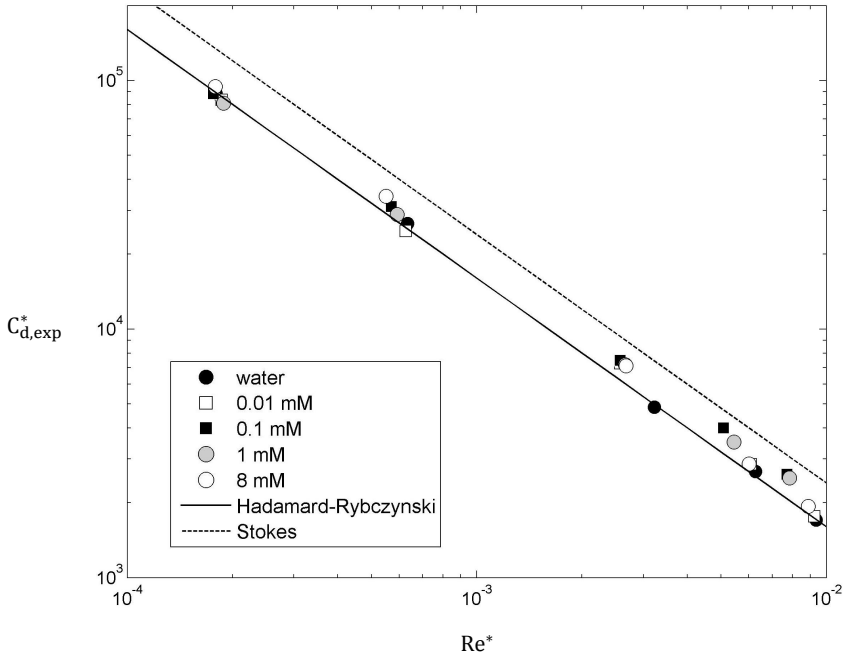

Figure 6.13 *The drag coefficients for different sized aqueous drops with either no SDS, 0.01, 0.1, 1 or 8 mM SDS are plotted versus Re^*. The upper dashed line represents the Stokes drag coefficient for solid sphere and the lower solid line represents the Hadamard-Rybczynski drag coefficient for fluid sphere without surfactant.*

chapter 4, the desorption Biot numbers, Bi^*_α, range from 0.5 at 0.125 μM SDS to 1×10^{-4} at 8 mM SDS. Experimental drag coefficients and other dimensionless operating parameters are tabulated in Table 6.3 later in this chapter. For concentrations between 1 μM and 4 mM the drops fell according to Stokes law i.e. like solid spheres. Below 1 μM the drag coefficients began decreasing and approached $C^*_{d,HR}$. Interestingly the drag coefficients also decreased relative to $C^*_{d,HR}$ as the CMC was approached. Behavior like this at high surfactant concentrations has been observed before and could be explained by the onset of micelle formation (111). Because the drop sizes and velocities are fairly large it is not expected that low Pe^*_s are observed and thus surface diffusion would not be the culprit.

Figure 6.13 is similar to Fig. 6.11(a) where experimental drag coefficients are plotted versus Re^* for experiments in 1000 cSt Si oil. The experimental drag coefficients and other

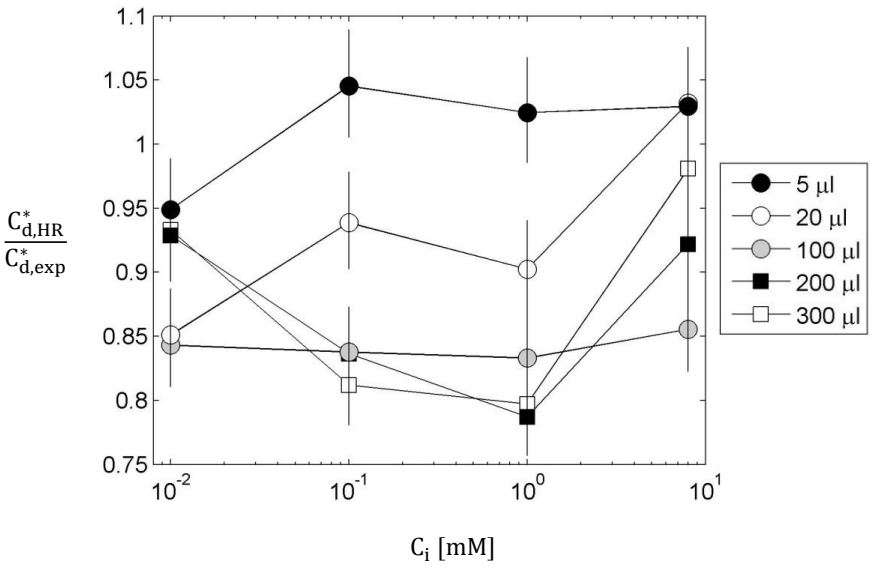

Figure 6.14 *The experimental drag coefficients from Fig. 6.13 are normalized by $C^*_{d,HR}$ and plotted versus C_i for several drop volumes. The vertical lines are error bars representing the uncertainty in drop velocity and radius measurements.*

dimensionless operating parameters are tabulated in Table 6.2 later in this chapter. In Fig. 6.13 the upper and lower lines again represent $C^*_{d,St}$ and $C^*_{d,HR}$, respectively. Marangoni numbers fell between 5 at the highest Re^* and 65 at the lowest Re^*. At the smallest Re^* all drops fell approximately according to the Hadamard-Rybczynski drag law. The clean water drops fell approximately according to the Hadamard-Rybczynski drag law for all Re^* within 5% which can be attributed to experimental error. The drag coefficients of drops containing surfactant however began deviating from $C^*_{d,HR}$ as Re^* increased.

The drag coefficients from Fig. 6.13 excluding those for water are normalized by $^*_{c,HR}$ and plotted in Fig. 6.14 versus bulk surfactant concentration C_i. This highlights some interesting trends that set the 1000 cSt Si experiments apart from the heavy mineral oil experiments. First no drop had drag coefficients equal to $C^*_{d,St}$ (the lower horizontal line indicated in Fig. 6.14), and larger bulk concentrations of SDS were required to affect drop velocities compared

to the heavy mineral oil experiments. Next the 5 μl drops were essentially unaffected by the presence of surfactant, and larger drops were affected most with 200 and 300 μl drops seeing the largest relative reduction in drag at 1 mM SDS. This may at first be counterintuitive since small drops with large Ma^* would be expected to be more affected by Marangoni stress than larger drops with small Ma^*. This was in fact the case in the heavy mineral experiments seen in Fig. 6.11(b). But one must keep in mind that drop velocities are orders of magnitude smaller in the 1000 cSt Si oil. This results in larger Bi_α^* and smaller Pe_s^* which can make surface diffusion relevant. Using the sorption kinetics models from chapter 4, for the 5 μl drops $0.005< Bi_\alpha^* <20$, for 20 μl drops $0.004< Bi_\alpha^* <13$, and for 100 μl drops $0.0025< Bi_\alpha^* <8$, all of which are much larger than the Bi_α^* observed in the heavy mineral oil experiments. The 200 and 300 μl drops had smaller Bi_α^* that ranged from 0.002 at 8 mM SDS to 5 at 0.01 mM SDS. While a surface diffusion coefficient D_s is unknown, the smaller velocities and in some cases smaller drop volumes will also result in much smaller Pe_s^* than in the heavy mineral oil experiments. Therefore surface diffusion is likely reducing surface concentration gradients and Marangoni stress in the smaller drops.

6.3.3 *Theoretical results using experimental sorption kinetics*

In the experimental results some fundamental differences between experiments in heavy mineral and experiments in 1000 cSt Si oil were found. Specifically in the 1000 cSt Si oil it was found that the terminal velocity of larger drops were generally more affected by the addition of surfactant than smaller drops relative to the Hadamard-Rybczynski velocity for clean drops. Surface diffusion could explain some of this behavior.

In generating theoretical drag coefficients for experiments in 1000 cSt Si oil the sorption kinetics for SDS in 1000 cSt Si oil in chapter 4 are used. In the experiments performed in 1000 cSt Si oil the Bi_α^*, Ma^* and $K_{eq}C_i$ values are relatively large so the analytical approach is used to predict drag coefficients to compare to experiments in 1000 cSt Si oil. Additionally since surface diffusion will not be neglected here the addition of surface diffusion

further reduces the magnitude of surface concentration gradients. This helps in having the analytical solution converge on a solution since the surface concentration is represented by a truncated series of Legendre polynomials. The smoother concentration profiles require less terms in the Fourier-Legendre series.

In contrast to experiments performed in 1000 cSt Si oil, the experiments in heavy mineral oil had small values for Bi^*_α, Ma^* and $K_{eq}C_i$. This meant the analytical approach becomes quite stiff and difficult to converge. Instead the boundary element approach was used to compare to experiments in heavy mineral oil. The sorption kinetics for SDS in heavy mineral oil from chapter 4 are used.

If surface diffusion were neglected it would be impossible to have smaller drops be less affected by Marangoni stress than larger drops with the same bulk concentration as observed in experiments in 1000 cSt Si oil from Fig. 6.14. As discussed earlier surface diffusion may be able to help explain some of the differences between the 1000 cSt Si oil experiments and the heavy mineral oil experiments. By incorporating surface diffusion, a new unknown must be determined which is the surface diffusion coefficient D_s. The surface diffusion coefficient is difficult to determine and is not known for these experiments, so D_s is treated as a fitting parameter.

Through some trial and error, it was found that a surface diffusion coefficient of $D_s = 4 \times 10^{-7}$ m^2 s^{-1} provided good agreement with experimental drag coefficients while still using the sorption kinetics from chapter 4. This value is quite large compared to diffusion coefficients in the literature, but again the surface diffusion coefficient here is treated as a fitting parameter. A potential physical explanation for such a large surface diffusion coefficient could be that it incorporates some additional non-ideal repulsive interactions between adsorbed surfactant molecules similar to the interaction parameter in eq. 6.6.

Carrying on with this value for D_s, the analytical approach was solved for varying drop sizes and bulk concentrations to be compared to the experiments. In Fig. 6.15 the normalized analytical drag coefficients for the four bulk concentrations used in experiments are

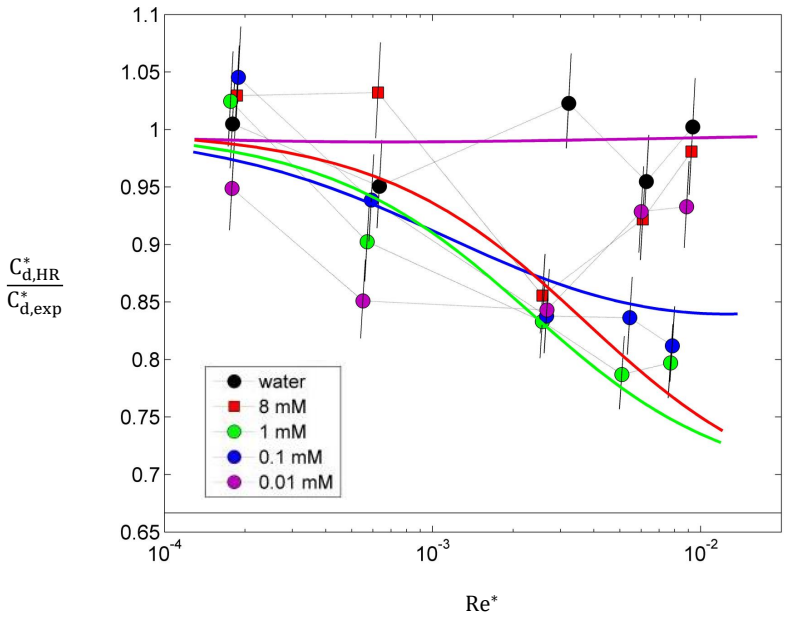

Figure 6.15 *The drag coefficients using $SDS_{(aq)}$ - 1000 cSt Si oil sorption kinetics from chapter 4 and $D_s = 4\times10^{-7}$ m^2 s^{-1} predicted by the analytical approach are normalized by $C^*_{d,HR}$ and plotted versus Re^* as solid lines. The normalized experimental drag coefficients from Fig. 6.14 are also plotted versus Re^* as the markers indicated in the legend. The colors of the analytical solution curves correspond to the experimental marker colors. The black horizontal line at the bottom of the plot represents $C^*_{d,HR}/C^*_{d,St}$.*

plotted versus Re^* as solid and dashed lines. Re^* primarily indicates changes in drop size here. The experimental normalized drag coefficients from Fig. 6.14 are also plotted here for comparison. Using $D_s = 4 \times 10^{-7}$ m^2 s^{-1} the result of smaller drops (smaller Re^*) being less affected by Marangoni stress than larger drops is observed which agrees qualitatively with the experiments. The experimental results suggested the 8 mM drops fell faster relative to an ideal clean drop than 0.1 and 1 mM drops at lower Re^* and this is also seen in Fig. 6.15. Also at higher Re^* the experiments showed 1 mM drops falling slower relative to a clean drop followed by 0.1 mM and then 8 and 0.01 mM drops. This result is seen in the analytical solutions.

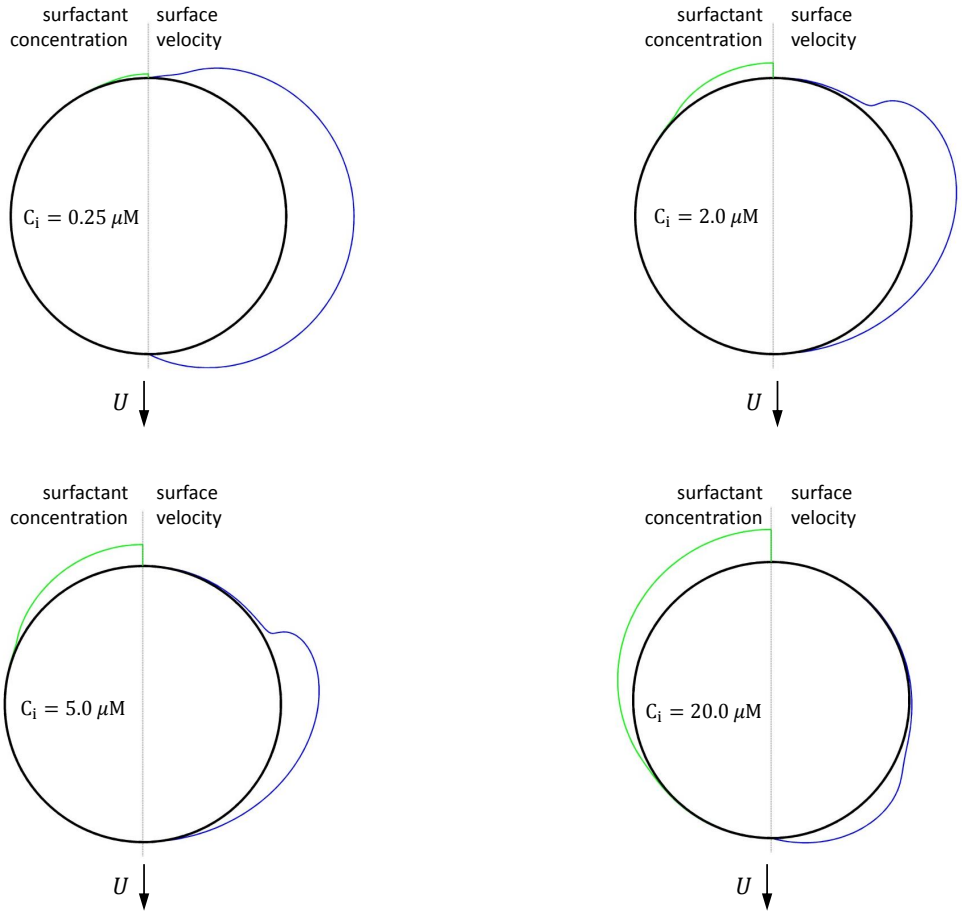

Figure 6.16 *The surface surfactant concentration and surface velocity is visualized for several 100 µl drops with different C_i in heavy mineral oil as predicted by the boundary element method. The left half of each drop shows the surfactant concentration and the right half shows the surface velocity.*

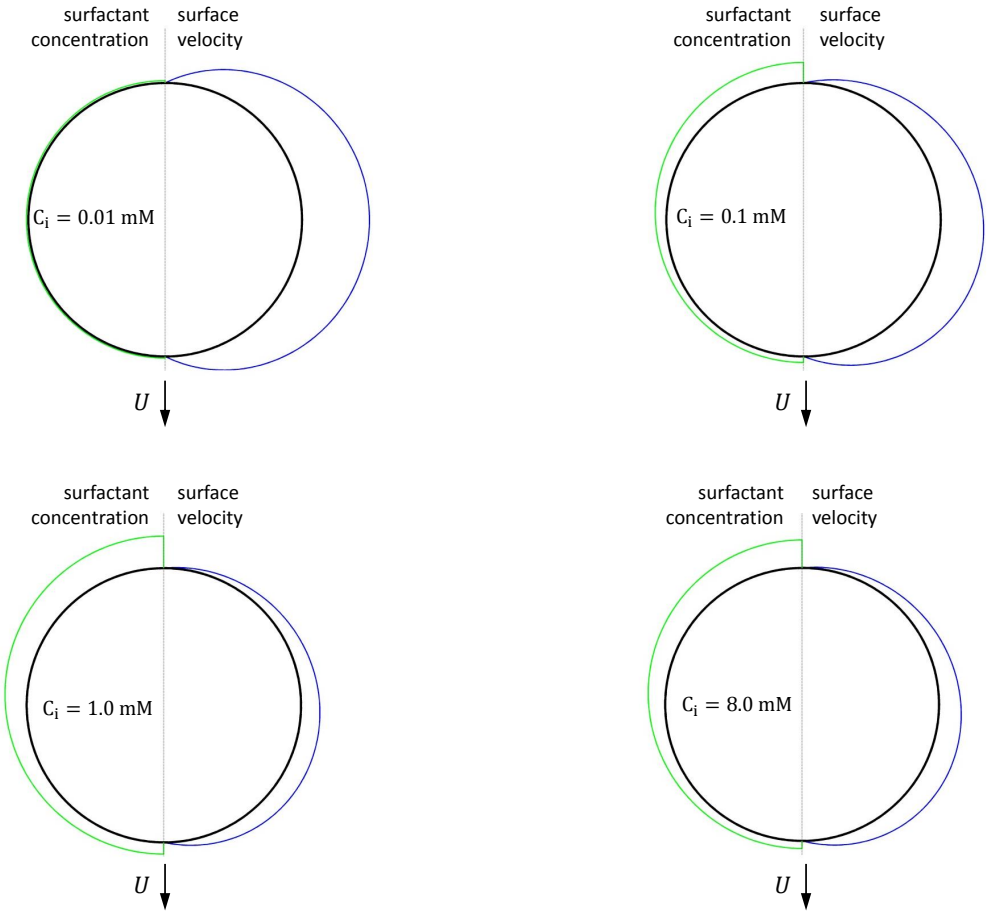

Figure 6.17 *The surface surfactant concentration and surface velocity is visualized for several 300 µl drops with different C_i in 1000 cSt Si oil as predicted by the analytical approach using $SDS_{(aq)}$ - 1000 cSt Si oil sorption kinetics and $D_s = 4 \times 10^{-7}\ m^2\ s^{-1}$. The left half of each drop shows the surfactant concentration and the right half shows the surface velocity.*

Figures 6.16 and 6.17 show qualitatively the predicted surface surfactant concentration profiles and surface velocity profiles plotted in polar coordinates for 100 μl drops falling in heavy mineral oil and 300 μl drops falling in 1000 cSt Si oil, respectively. The solid black circle is the drop surface, the left half shows the surface concentration profile, and the right half shows the velocity profile. The profiles shown in Fig. 6.16 for 100 μl drops falling in heavy mineral oil were determined using the boundary element method, and those in Fig. 6.17 were determined using the analytical approach. The bulk surfactant concentrations for each simulation are annotated on each drop.

In Fig. 6.16 at the smallest concentration $C_i = 0.25$ μM a very small amount of surfactant accumulates at the rear, making a very small impact on the surface velocity at the rear. Otherwise the surface is almost completely mobile and the drop falls only slightly slower than a drop without any surfactant. At 2 μM the boundary element method predicts the drag coefficient to be about 10% higher than a clean drop. A noticeable increase in surfactant is shown in the rear and a clear stagnant cap region emerges. The stagnant cap grows at $C_i = 5$ μM. By 20 μM surfactant covers a majority of the surface with now an even greater amount accumulating at the rear. This causes the surface velocity to decrease to zero at the back half of the drop and the drag coefficient as predicted by the boundary element method has approached $C^*_{d,St}$.

The profiles in Fig. 6.17 of drops falling in 1000 cSt Si oil are fundamentally different from those in heavy mineral oil. At 0.01 mM some surfactant adsorbs to the surface but the profile is nearly uniform. The lack of strong surfactant and surface tension gradients results in almost no effect on the surface velocity. At 0.1 mM more surfactant adsorbs but the gradient in surfactant concentration is gradual from the front to the rear. The gradient is enough to affect the surface velocity, but no stagnant cap develops and only about a 15% reduction in the drag coefficient relative to $C^*_{d,HR}$ is predicted. The 1 and 8 mM results are slightly amplified versions of the 0.1 mM result. The 8 mM result actually predicts that there will be slightly less surfactant on the surface than 1 mM. This is due to the way the

poles are handled in the analytical approach. The boundary condition at the poles is only a symmetry condition, and so surfactant that reaches either pole is allowed to reenter the drop bulk. Diffusion becomes so dominant in the 8 mM solution that surfactant reenters the drop bulk at the poles.

6.3.4 *Comparisons between experimental and predicted drag coefficients*

Table 6.2 shows experimental drag coefficients for drops falling in 1000 cSt Si oil as well as those predicted by the analytical approach. The percent difference included in the table is defined by $\%\text{error} = 100 \times |C^*_{d,exp} - C^*_{d,pred}|/C^*_{d,exp}$. The experimental drag coefficients are the same as those in Fig. 6.13. Also included in Table 6.2 are values for Re^*, Ma^*, Bi^*_α and $K_{eq}C_i$. For the chosen value of $D_s = 4 \times 10^{-7}$ m^2 s^{-1} the corresponding Pe^*_s are also shown. The Re^* are orders of magnitude smaller than the experiments in heavy mineral oil. Due to the much slower terminal velocities, Ma^* and Bi^*_α are also considerably larger. The estimated Pe^* are between O(0.1) and O(10). Based on the results of Fig. 6.5 these low Pe^*_s in combination with the Ma^*, $K_{eq}C_i$ and Bi^*_α would suggest that surface diffusion is significant.

When comparing the predicted and experimental drag coefficients it is important to keep in mind that a single set of five constants were used to model the adsorption and desorption processes: Γ_∞, Λ, $\hat{\beta}_0$, $\hat{\alpha}_0$ and the exponent m. The bulk concentration C_i and drop radius b were determined by the experiments, and the surface diffusion coefficient was treated as a fitting parameter and fixed to $D_s = 4 \times 10^{-7}$ m^2 s^{-1}. With this in mind the predicted drag coefficients were within about 15% of the experimental values save for a few cases as seen in Table 6.2. This is over a range of drag coefficients that spans two orders of magnitude. Considerably better agreement was found for $C_i = 0.1$ and $C_i = 1$ mM where the percent error was between 0.1% and 16.2%. The worst agreement was seen for drops with 8 mM SDS. In the heavy mineral oil experiments, as the CMC was approached the drag coefficients decreased significantly. As mentioned earlier this behavior has been observed before (111)

Table 6.2 *Experimental and predicted drag coefficients for aqueous drops containing different concentrations of SDS falling in 1000 cSt Si oil. The experimental Re^*, Ma^* and Bi^*_α are also shown. Estimates for Pe^*_s using $D_s = 4 \times 10^{-7}$ m^2 s^{-1} are shown as well. The quantity $K_{eq}C_i$ is determined using the K_{eq} from Table 4.1.*

V [μl]	C_i [mM]	Re^* –	Ma^* –	Bi^*_α –	$K_{eq}C_i$ –	Pe^*_s –	$C^*_{d,exp}$ –	$C^*_{d,pred}$ –	% error –
5	0.01	0.000179	64.5	19.7	0.0153	0.226	94400	91200	3.4
5	0.1	0.000189	60.2	1.12	0.153	0.238	81100	94300	16.2
5	1	0.000177	63.4	0.0713	1.53	0.223	88500	93000	5.1
5	8	0.000186	61.1	0.00564	12.2	0.235	83400	91800	10.0
20	0.01	0.000550	31.6	14.5	0.0153	0.695	34200	25900	24.3
20	0.1	0.000591	29.2	0.820	0.153	0.747	28800	29000	0.7
20	1	0.000570	30.3	0.0525	1.53	0.720	31100	28600	8.0
20	8	0.000627	27.2	0.00376	12.2	0.791	24800	27600	11.3
100	0.01	0.00267	11.1	8.64	0.0153	3.37	7110	5280	25.8
100	0.1	0.00266	11.1	0.536	0.153	3.36	7180	6860	4.5
100	1	0.00257	11.4	0.0335	1.53	3.25	7480	7490	0.2
100	8	0.00257	11.3	0.00266	12.2	3.25	7270	6950	4.4
200	0.01	0.00601	6.24	6.18	0.0153	7.58	2870	2520	12.3
200	0.1	0.00544	6.90	0.422	0.153	6.87	3520	3440	2.1
200	1	0.00508	7.37	0.0280	1.53	6.42	4000	4110	2.8
200	8	0.00609	6.20	0.00190	12.2	7.69	2850	3850	34.9
300	0.01	0.00887	4.80	5.41	0.0153	11.2	1930	1700	11.9
300	0.1	0.00784	5.46	0.382	0.153	9.90	2510	2360	6.0
300	1	0.00772	5.55	0.0239	1.53	9.75	2600	2960	13.9
300	8	0.00925	4.59	0.00159	12.2	11.7	1970	2810	42.6

Table 6.3 *Experimental and predicted drag coefficients for aqueous drops containing different concentrations of SDS falling in heavy mineral oil. The experimental Re^*, Ma^* and Bi^*_α are also shown. The quantity $K_{eq}C_i$ is determined using the K_{eq} from Table 4.1.*

C_i [mM]	Re^*	Ma^*	Bi^*_α	$K_{eq}C_i$	$C^*_{d,exp}$	$C^*_{d,pred}$	% error
0.000125	0.447	2.84	0.527	0.000906	38.6	33.7	12.7
0.00025	0.400	3.17	0.345	0.00181	48.0	34.1	29.0
0.0005	0.354	3.59	0.229	0.00363	61.0	34.9	42.8
0.000625	0.323	3.93	0.2111	0.00453	73.6	35.4	51.9
0.00125	0.323	3.93	0.124	0.00906	73.9	37.5	49.3
0.0025	0.322	3.94	0.073	0.0181	74.1	41.5	44.0
2	0.322	3.94	0.000424	14.5	74.2	–	–
4	0.321	3.96	0.000250	29.0	74.9	–	–
7	0.340	3.74	0.000153	50.8	66.6	–	–
8	0.426	2.98	0.000110	58.0	42.4	–	–

and the theoretical analysis presented in this chapter is not equipped to explain it. It is possible that the mechanism causing the decrease in drag near the CMC in heavy mineral experiments is having the same effect in the 1000 cSt Si oil experiments.

The open squares in Fig. 6.12 represent solutions of the boundary element method using the sorption kinetics from chapter 4 and a non-deforming drop. The experimental and predicted drag coefficients along with the dimensionless operating parameters are tabulated in Table 6.3. It is assumed Pe^*_s are large enough that surface diffusion can be neglected. While similar trends are seen in Fig. 6.12 with regards to how C^*_d changes with C_i, the numerical results are shifted right by about one order of magnitude in C_i. The percent error between the experimental and predicted drag coefficients are fairly large as seen in Table 6.3. Again this shift could potentially be explained by the presence of some unknown surface-active component in the heavy mineral oil as deduced from Fig. 6.11. Also the fact that the boundary element results *underestimate* the impact of adding surfactant suggests that surface diffusion is not a factor in these experiments; incorporating surface diffusion would cause the drag to be reduced even more in the simulations. Finally it should be noted that

$Re^* \sim 0.4$ for these experiments could also be limiting the ability to use theory based on a Stokes flow assumption.

6.4 Discussion and conclusions

In this chapter the terminal velocities of aqueous drops settling under gravity in heavy mineral oil or 1000 cSt Si oil were measured. The varying surfactant concentrations in the drop phase were used as well as varying drop volumes. Then using sorption kinetics determined experimentally in chapter 4, theoretical predictions of the drop drag coefficients were made using either an analytical or boundary element approach. Qualitative agreement for drag coefficients was found between the theoretical predictions and the heavy mineral oil experiments while both qualitative and some quantitative agreement was found in the 1000 cSt Si oil system.

Based on experimental observations in the heavy mineral oil system, it is possible that the heavy mineral oil itself contains some surface-active components. Evidence for this was presented in Fig. 6.11 where drops of deionized water had drag coefficients greater than those predicted by the Hadamard-Rybczynski drag law when volumes were less than 100 μl. Since the 100 μl clean water drops were the smallest drops to follow $C^*_{d,HR}$ and larger drops had $Re^* \to 1$ which could make the Stokes assumption less valid, the 100 μl volume in heavy mineral oil was chosen to observe how changes in surfactant concentrations in the bulk affected drop velocities. When using the sorption kinetics from chapter 4 qualitative agreement was found between theory and experiment as far as how the drag coefficient normalized by $C^*_{d,HR}$ varied with C_i in Fig. 6.12. The theoretical curve however was shifted right by an order of magnitude in Fig. 6.12. This provides additional evidence that surface-active components could be present in the heavy mineral oil.

The experiments in 1000 cSt Si oil exhibited behavior that was fundamentally different from the heavy mineral oil experiments. Whereas decreasing the drop volume increased the relative impact of Marangoni stress in the heavy mineral oil experiments, in the Si oil

experiments the smallest drops were least affected by the addition of surfactant. In fact the 5 μl drops falling in 1000 cSt Si oil were essentially unaffected by the addition of surfactant. The drops most affected by the addition of surfactant were the largest at 200 and 300 μl, and no drop fell according the the Stokes drag law i.e. like a solid sphere. The most likely explanation for this behavior is that surface diffusion has become important in contrast to the experiments in the less dense and less viscous heavy mineral oil. The drop velocities were orders of magnitude smaller in the Si oil, causing Bi_α^* to be orders of magnitude larger and Pe_s^* to be orders of magnitude smaller.

Since surface diffusion coefficients are unknown for the systems studied, the surface diffusion coefficient D_s was treated as a fitting parameter. After trial and error a value of $D_s = 4 \times 10^{-7}$ m^2 s^{-1} was determined to best fit all of the 1000 cSt Si oil data. While this is a large value, its magnitude could possibly be explained by its accounting for potential net repulsive interactions between adsorbed surfactant molecule. Net repulsive interactions between SDS surfactant molecules was determined from fits of the Frumkin isotherm and equation of state to equilibrium surface tension data. Using this D_s and the sorption kinetics model from chapter 4, good agreement between experimental drag coefficients and predicted drag coefficients using the analytical approach was found in Table 6.2 for a good portion of the experimental cases. This was particularly true for the 0.1 and 1 mM SDS experiments where the theoretical predictions agreed within 10% for all but two cases. It should be emphasized that these predictions were all made using one set of constants with the bulk surfactant concentration of SDS and the drop volume being the only variables.

In the future it would be beneficial to perform experiments with other surfactants that fit the assumptions made in the theory. However prevention of contamination and degradation of the experimental materials has been found to be difficult. Future theoretical work would benefit from the inclusion of bulk mass transfer phenomena including convection and diffusion. Additionally the boundary element method is well suited to model multiple drops and their interactions (112; 113). As this chapter has demonstrated the ability to use experimen-

tally determined sorption kinetics to predict the velocities of single surfactant-laden drops, the same sorption models may be able to predict experiments involving multiple drops.

CHAPTER 7. SUMMARY AND CONCLUSIONS

In this thesis the main goal was to use experimentally determined surfactant sorption models to predict and explain behavior observed in interfacial fluid dynamics problems. The first fluid dynamics problem involved a single aqueous surfactant-laden drop in a partially oil-filled rotating horizontal cylindrical tank. The second problem involved a single aqueous surfactant-laden drop settling in an oil under gravity. However prior to studying the fluid dynamics problems the surfactant systems had to be characterized.

Characterizing the surfactant systems began with measuring surface tension in chapter 2. In that chapter the pendant drop method was used which has become a relatively common and robust measurement technique. However a novel use of the non-gradient-based pattern search minimization algorithm was used to fit drop profiles prescribed by the Young-Laplace equation to experimental drop profiles. The pattern search method used here has been mathematically proven to be capable of consistently converging to a local minimum (52; 53). The algorithm is fast, easy to implement and robust in terms of sensitivity to initial guesses in contrast to gradient-based solvers like the Newton-Raphson method (16).

In addition the pattern search algorithm was used to fit the Frumkin isotherm and equation of state to surface tension data to estimate equilibrium surfactant sorption parameters. The convergence criteria was analyzed for the equation and the upper bound limit for the molecular interaction parameter Λ was extended using a Taylor series expansion of the Frumkin isotherm equation for small fractional surface coverage. The curve fits from the pattern search method and stability criteria determined from linearization of the Frumkin isotherm fit the data fairly well.

The analysis from chapter 2 was extended in chapter 3 to include the effects of depletion of surfactant in the bulk. Three pendant drop/bubble variations were used to measure γ_{eq} for nonionic $C_{12}E_4$ at an air-water interface. The pendant bubble experiments were not affected by depletion, but the pendant drops were. Regardless fits of the Frumkin equation of state with the modified Frumkin isotherm presented in chapter 3 were used to determine equilibrium surfactant sorption parameters for each case, and the parameter values were all in excellent agreement. The modified isotherm presented in 3 gives more flexibility in designing pendant drop experiments, and the resulting analysis allows for an accurate prediction for when depletion will be significant. This would be helpful when designing small-scale interfacial experiments such as in microfluidic devices where surface area to volume ratios can become quite large.

Chapter 4 continued the characterization of the surfactant systems by determining the adsorption and desorption rates necessary in modeling interfacial fluid dynamics problems. The systems for which models were developed involved surfactant that was soluble in one phase and insoluble in the other. Using the analysis in chapter 3 depletion effects in the bulk were neglected. Additionally a diffusion length scale for the case when surfactant resides inside a sphere was developed and used to predict when bulk diffusion would be important.

Afterward transient surface tension data was fit to an adsorption-desorption model both with and without accounting for diffusion. The adsorption-desorption models were fit again using the pattern search algorithm. For certain systems the sorption rates when accounting for diffusion and when neglecting diffusion did not differ much, suggesting bulk diffusion could be neglected. For the systems where both depletion and bulk diffusion could be neglected, it was found that sorption rate constants varied with the bulk surfactant concentration to some exponent m. The adsorption-desorption model was then modified to reflect this concentration dependence, and a single set of five constants could then be used to characterize a surfactant system.

The first of two fluid dynamics problems studied was presented in chapter 5. There a single aqueous drop with or without surfactant was placed in a horizontal cylindrical rotating tank half-filled with light mineral oil. As the tank rotated, the drop reached an equilibrium position in the tank where a thin film of oil separated the drop from the tank wall. Focusing on the thin film, the analysis treated the drop-containing flow as a thin film problem. The experiments themselves were unique and provide a new experiment approach to studying thin films.

The aqueous drop contained either sodium oleate (SO) or sodium dodecyl sulfate (SDS). Both of these surfactants were similar physically, being anionic and containing a long hydrocarbon tail. But as seen in chapter 2 the two surfactants have roughly equal and opposite Frumkin interaction parameters Λ, where the SO experiences net attraction between surfactants and the SDS experiences net repulsion. This had a significant impact on drop deformation and the onset of tail streaming at higher capillary numbers.

Since it is well known that surfactant and surface tension gradients will develop on the drop surfaces, assigning a capillary number to each experiments is difficult. Using numerical integration of the thin film equations incorporating the sorption kinetics determined in earlier chapters, predictions for the film thickness as a function of the capillary number based on the *clean* (no surfactant) surface tension were made. These predictions were in good agreement with experimental observations, so the numerically generated surface surfactant concentration profiles were further used to characterize the experiments by making better predictions for the capillary number. These updated capillary numbers used the minimum surface tension predicted over the drop surface, and relationships between drop stretching relative to a drop without surfactant and the new capillary number were shown. The transition from little drop stretching to significant drop stretching occurred when the new estimated capillary numbers were between 0.1 and 1. This range agrees with other experimental observations involving drop deformation and breakup (10).

The numerical results provided some additional explanations for differences between drops with SO and with SDS. First due to the differences in Λ the SO is predicted to be able to reach surface surfactant concentrations approaching Γ_∞ well before the bulk critical micellar concentration is reached, while this is not the case for SDS. This is a result that could only be accounted for using the Frumkin isotherm and equation of state, highlighting the importance of using a proper equation of state. The lower surface coverages in SDS drops explains why those drops appeared to be less affected by adding surfactant in experiments. Next a flow reversal was observed at the rear of the 2 mM SO drops in simulations using the stationary wall frame of reference, providing a possible explanation for the onset of tail streaming observed in experiments. However since the experiments include three-dimensional effects it is not conclusive that this flow reversal observed in solutions of the two-dimensional thin film equations is responsible for tail-streaming. Still the numerical results incorporating experimentally determined sorption kinetics provided interesting insight into not only how gradients in surface tension affect the flow but how different surfactants can have a significant impact on deformation and breakup.

The sorption models developed in chapter 4 were again used in chapter 6. In that chapter the terminal velocity of a single surfactant-laden drop was measured as it settled in another viscous fluid under gravity. By incorporating the sorption models into the analysis, qualitative agreement was found between the theoretical predictions and experiments performed in heavy mineral oil while both qualitative and some quantitative agreement was found in experiments performed in the 1000 cSt silicone (Si) oil system. Discrepancies in the experiments performed in heavy mineral oil were thought to be due to the potential presence of surface-acting components in the mineral oil.

Settling drop experiments performed in 1000 cSt Si oil fell much slower due to the increased viscosity and density of the oil, and so surface diffusion became more important. Treating the surface diffusion coefficient as a fitting parameter, good agreement between theory and experiments for the majority of cases was found by using one set of sorption

model constants and a single surface diffusion coefficient even as bulk concentrations and drop volumes varied. The results both show to potential to use real surfactant transport parameters to predict the velocities of these drops, although much more work needs to be done.

This thesis succeeds in using experimentally determined surfactant sorption kinetics to analyze, explain and predict some experimental observations in two interfacial fluid dynamics problems. Direct comparisons between experiments and theory in these types of problems is not common in the literature, but they are necessary if the theoretical tools at our disposal are to be used in real engineering applications. The ability to make such comparisons has been demonstrated here, but still much work needs to be done.

In the future it would be interesting to focus on the tail streaming in the horizontal rotating tank problem from chapter 5. The very simple apparatus could provide a cheap and easy method for creating emulsions and even encapsulating particles or cells. By robustly characterizing the rate of drop production and size of drops produced in tail streaming, for example, a cell concentration in the aqueous drop could be chosen to encapsulate roughly a single cell in each broken-off droplet. Currently microfluidics are often used to encapsulate cells for applications such as genome sequencing (114), and this could be a cheap alternative.

In the buoyancy-driven drop problem presented in this thesis it will be insightful to include bulk diffusion and convection effects in side the drop. Constructing a larger experimental tank for longer observation times and travel distances could also allow for observing the effects of surfactants with very slow sorption kinetics. Using the boundary element method with the experimentally determined sorption kinetics could also provide interesting insight into flows containing multiple drops.

APPENDIX ADDITIONAL INFORMATION FOR THE BOUNDARY ELEMENT APPROACH

Cubic spline interpolation

For the boundary element method, cubic spline interpolation is used to determine the coordinates along the ith boundary element between nodes i and $i+1$. The x and y coordinates have the form

$$x(s) = P_{x,i}(s) = A_{x,i}(s - s_i)^3 + B_{x,i}(s - s_i)^2 + C_{x,i} + x_i \tag{7.1}$$

and

$$y(s) = P_{y,i}(s) = A_{y,i}(s - s_i)^3 + B_{y,i}(s - s_i)^2 + C_{y,i} + y_i \tag{7.2}$$

where $s_i \leq s \leq s_{i+1}$ and the coefficients are to be determined. Three conditions are satisfied everywhere: $x(s_{i+1}) = x_{i+1}$ and $y(s_{i+1}) = y_{i+1}$, the first derivatives match at each node approaching from either side, and the second derivatives match at each node approaching from either side. For the x coordinates for example, this requires the following expressions to be upheld:

$$x_{i+1} = x_i + A_{x,i}h_i^3 + B_{x,i}h_i^2 + C_{x,i}h_i, \tag{7.3}$$

$$C_{x,i+1} = C_{x,i} + 3A_{x,i}h_i^2 + 2B_{x,i}h_i, \tag{7.4}$$

and

$$B_{x,i+1} = B_{x,i} + 3A_{x,i}h_i, \tag{7.5}$$

where $h_i = (s_{i+1} - s_i)$. This is likewise for y coordinates. To complete the interpolation, a periodic boundary condition is imposed so that, for x coordinates,

$$C_{x,1} = 3A_{x,N}h_N^2 + 2B_{x,N}h_N + C_{x,N} \tag{7.6}$$

and

$$B_{x,1} = B_{x,N+1}, \tag{7.7}$$

where N is the number of nodes. Again the same is true for y coordinates. The above equations result in a periodic tridiagonal matrix system of equations that can be solved using the process outlined in *A Practical Guide to Boundary Element Methods* (107) to determine the coefficients in eqs. 7.1 and 7.2.

Integrating the singular single layer potential

The boundary integral equation in chapter 4 consists of two integrals. The first integral is the single layer potential and has a singularity that goes like $-2\ln|\boldsymbol{x} - \boldsymbol{x}_o|$. Integrating the integral as is with standard Gauss-Legendre quadrature would result in considerable errors. Instead the integral will be modified by subtracting the singularity and then integrating the singularity separately. First we will rewrite the single layer potential integral using a trapezoidal-like approximation to isolate the integration of the velocity Green's functions $\boldsymbol{G}$ (113),

$$\int_C \boldsymbol{G}(\boldsymbol{x}, \boldsymbol{x}_o)\Delta\boldsymbol{f}(\boldsymbol{x})d\ell(\boldsymbol{x}) \approx \frac{1}{S}\int_C \Delta\boldsymbol{f}(\boldsymbol{x})d\ell(\boldsymbol{x}) \int_C \boldsymbol{G}(\boldsymbol{x}, \boldsymbol{x}_o)d\ell(\boldsymbol{x}), \tag{7.8}$$

where S is the total arc length. Now focusing on the integration of $\boldsymbol{G}$ we subtract the singularity and add it back separately:

$$\int_C \boldsymbol{G}(\boldsymbol{x},\boldsymbol{x}_o)d\ell(\boldsymbol{x}) = \int_C \left[\boldsymbol{G}(\boldsymbol{x},\boldsymbol{x}_o) + 2\ln|\boldsymbol{x}-\boldsymbol{x}_o|\right] d\ell(\boldsymbol{x}) - 2\int_C \ln|\boldsymbol{x}-\boldsymbol{x}_o| d\ell(\boldsymbol{x}). \tag{7.9}$$

The problem now is solving the second integral on the right-hand side above. This is done following the process in *A Practical Guide to Boundary Element Methods* (107). Consider the integration of the singular integral over the ith boundary element. It then becomes

$$-2\int_{C_i} \ln|\boldsymbol{s}-\boldsymbol{s}_o| d\ell(\boldsymbol{x}) = -2\int_{s_i}^{s_{i+1}} \ln\frac{|\boldsymbol{x}(s)-\boldsymbol{x}(s_o)|}{s-s_o} h_i(s)ds - 2\int_{s_i}^{s_{i+1}} \ln|s-s_o| h_i(s)ds \tag{7.10}$$

where $\boldsymbol{x}_o = \boldsymbol{x}(s_o)$. The metric coefficients $h_i(s)$ are in terms of the cubic spline interpolation coefficients,

$$h_i(s) = \sqrt{\left[3A_{x,i}(s-s_i)^2 + 2B_{x,i}(s-s_i) + C_{x,i}\right]^2 + \left[3A_{y,i}(s-s_i)^2 + 2B_{y,i}(s-s_i) + C_{y,i}\right]^2}, \tag{7.11}$$

and $s = \frac{1}{2}(s_i + s_{i+1}) + \frac{1}{2}(s_{i+1} - s_i)\xi$ where ξ are the Gauss-Legendre quadrature abscissas. The first integral on the right-hand side of eq. 7.10 is not singular but the second integral is. This second integral is further modified:

$$-2\int_{s_i}^{s_{i+1}} \ln|s-s_o| h_i(s)ds = -2\int_{s_i}^{s_{i+1}} \ln|s-s_o|[h_i(s)-h_i(s_o)]ds - 2h_i(s_o)\int_{s_i}^{s_{i+1}} \ln|s-s_o| ds. \tag{7.12}$$

Finally the first integral on the right-hand side of eq. 7.12 can be integrated with Gauss-Legendre quadrature and the second integral can be integrated analytically.

Green's functions

For an axisymmetric body in an unbounded domain, the velocity Green's functions are (109)

$$\begin{aligned} G_{xx} &= yI_{10} + (x - x_o)^2 I_{30} \\ G_{xy} &= (x - x_o)(y^2 I_{30} - yy_o I_{31}) \\ G_{yx} &= (x - x_o)(y^2 I_{31} - yy_o I_{30}) \\ G_{yy} &= yI_{11} + (y^3 + yy_o^2) I_{31} - y^2 y_o (I_{30} + I_{32}). \end{aligned} \tag{7.13}$$

The stress Green's functions are (109)

$$\begin{aligned} T_{xxx} &= -6y(x - x_o)^3 I_{50} \\ T_{xxy} &= -6(x - x_o)^2 (y^2 I_{50} - yy_o I_{51} \\ T_{xyx} &= T_{xxy} \\ T_{xyy} &= -6(x - x_o)(yy_o^2 I_{52} + y^3 I_{50} - 2y^2 y_o I_{51}) \\ T_{yxx} &= -6(x - x_o)^2 (y^2 I_{51} - -yy_o I_{50}) \\ T_{yxy} &= -6(x - x_o)[(y^3 + yy_o^2) I_{51} - y^2 y_o (I_{50} + I_{52})] \\ T_{yyx} &= T_{yxy} \\ T_{yyy} &= -6[y^4 I_{51} - y^3 y_o (I_{50} + 2I_{52}) + y^2 y_o^2 (I_{53} + 2I_{51}) - y_o^3 I_{52}]. \end{aligned} \tag{7.14}$$

The stress Green's functions contain the integrals $I_{mn}(x - x_o, y, y_o)$ which are defined as

$$I_{mn} = \frac{4k^m}{(4yy_o)^{m/2}} \int_0^{\pi/2} \frac{(2cos^2\omega - 1)^n}{(1 - k^2 cos^2\omega)^{m/2}} d\omega \tag{7.15}$$

where $k^2 = (4yy_o)/[(x - x_o)^2 + (y + y_o)^2]$ (109). To compute I_{mn} the numerator in the above integral is expanded resulting in an expression composed of complete elliptic integrals of the first and second kind which have solutions tabulated in ref. (115).

When de-singularizing the double layer potential for axisymmetric Stokes flow, a second tensor is used, $\boldsymbol{P}$ (109; 107). This tensor is defined as

$$\begin{aligned} P_{xx} &= T_{yxx} \\ P_{xy} &= T_{yxy} \\ P_{yx} &= -6(x - x_o)(y^3 I_{52} + y y_o^2 I_{50} - 2y^2 y_o I_{51} \\ P_{yy} &= -6[y^4 I_{52} - y y_o^3 I_{51} - y^3 y_o (I_{53} + 2I_{51}) + y^2 y_o^2 (I_{50} + 2I_{52})] \end{aligned} \tag{7.16}$$

BIBLIOGRAPHY

[1] T. Sale, K. Pionek, M. Pitts. Chemically enhanced in situ washing. *Proceedings of the 1989 NWWA/API Conference on Petroleum Hydrocarbons and Organic Chemicals in Ground Water - Prevention, Detection and Restoration* (1989) pp. 487-503.

[2] C.N. Mulligan, R.N. Yong, B.F. Gibbs. Surfactant-enhanced remediation of contaminated soil: a review. *Eng. Geol.* **60** (2001) pp. 371-380.

[3] L.E. Scriven. Physics and applications of dip coating and spin coating. *Mat. Res. Soc. Symp. Proc.* **121** (1988) pp. 717-729.

[4] T.G. Myers. Thin films with high surface tension. *SIAM Rev.* **40** (1998) pp. 441-462.

[5] K. Landfester, N. Bechthold, F. Tiarks, M. Antonietti. Formation and stability mechanisms of polymerizable miniemulsions. *Macromolecules* **32** (1999) pp. 5222-5228.

[6] K.A. Subramanian. A comparison of water-diesel emulsions and timed injection of water into the intake manifold of a diesel engine for simultaneous control of NO and smoke emissions. *Energy Convers. Manage.* **52** (2011) pp. 849-857.

[7] N. Garti. Double emulsions - Scope, limitations and new achievements. *Colloids Surf. A* **123** (1997) pp. 233-246.

[8] N. Garti. Progress in stabilization and transport phenomena of double emulsions in food applications. *Food Sci. Technol.* **30** (1997) pp. 222-235.

[9] S.L. Anna, H.C. Mayer. Microscale tipstreaming in a microfluidic flow focusing device. *Phys. Fluids* **18** (2006) pp. 121512.

[10] H.A. Stone. Dynamics of drop deformation and breakup in viscous fluids. *Annu. Rev. Fluid Mech.* **26** (1994) pp. 65-102.

[11] R.A. De Bruijn. Tipstreaming of drops in simple shear flows. *Chem. Eng. Sci.* **48** (1993) pp. 277-284.

[12] C.D. Eggleton, T.-M. Tsai, K.J. Stebe. Tip streaming from a drop in the presence of surfactants. *Phys. Rev. Letters* **87** (2001) 048302.

[13] G. Kumar, N. Prabhu. Review of non-reactive and reactive wetting of liquids on surfaces. *Adv. Colloid Interface Sci.* **133** (2007) pp. 61-89.

[14] V.G. Levich, V.S. Krylov. Surface-tension-driven phenomena. *Annu. Rev. Fluid Mech.* **1** (1969) pp. 293-316.

[15] W.M. Deen. *Analysis of Transport Phenomena*. Oxford University Press: New York, NY (2012).

[16] Y. Rotenberg, L. Boruvka, A.W. Neumann. Determination of surface tension and contact angle from shapes of axisymmetric fluid interfaces. *J. Colloid Interface Sci.* **93** (1983) pp. 169-183.

[17] C. Huh, L.E. Scriven. Shapes of axisymmetric fluid interfaces of unbounded extent. *J. Colloid Interface Sci.* **30** (1969) pp. 323-337.

[18] W.N. Bond, D.A. Newton. Bubble, drops, and Stokes' law. *Phil. Mag. Ser. 7* **5** (1928) pp. 794-800.

[19] J. Hadamard. Mouvement permanent lent d'une sphère liquide et visqueuse dans un liquid visqueux. *Compt. Rend. Acad. Sci. (Paris)* **152** (1911).

[20] W. Rybczynski. Über die fortschreitende bewegung einer flüssigen kugel in einem zähen medium. *Bull. Acad. Sci. Cracovie* ser **A** (1911).

[21] G.G. Stokes. On the effect of the internal friction of fluids on the motion of pendulums. *Trans. Camb. Phil. Soc.* **9** (1851).

[22] V.G. Levich. *Physicochemical Hydrodynamics*. Prentice Hall: Englewood Cliffs, NJ (1962).

[23] L. Landau, B. Levich. Dragging of a liquid by a moving plate. *Acta Physicochim. (USSR)* **17** (1942) pp. 42-54.

[24] D.A. White, J.A. Tallmadge. Theory of drag out of liquids on flat plates. *Chem. Eng. Sci.* **20** (1965) pp. 33-37.

[25] F.P. Bretherton. The motion of long bubbles in tubes. *J. Fluid Mech.* **10** (1961) pp. 166-188.

[26] Y.-L. Wang, A.R. White, T. Ward. Pressure-driven microfluidic flow-focusing of air through a surfactant-doped dilute polymer liquid. *Microfluid Nanofluid* **18** (2015) pp. 343-356.

[27] R. Krechetnikov, G.M. Homsy. Surfactant effects in the Landau-Levich problem. *J. Fluid Mech.* **559** (2006) pp. 429-450.

[28] P. Groenveld. Low capillary number withdrawal *Chem. Eng. Sci.* **25** (1970) pp. 1259-1266.

[29] P. Savic. Circulation and distortion of liquid drops falling through a viscous medium. *National Research Laboratories Division of Mechanical Engineering (Canada) Report MT-22* (1953).

[30] R.H. Magarvey, J. Kalejs. Internal circulation within liquid drops *Nature* **198** (1963) pp. 377-378.

[31] T.J. Horton, T.R. Fritsch, R.C. Kintner. Experimental determination of circulation velocities inside drops. *Can. J. Chem. Eng.* **43** (1965) pp. 143-146.

[32] R.F. Davis, A. Arcrivos. The influence of surfactants on the creeping motion of bubbles. *Chem. Eng. Sci.* **21** (1966) pp. 681-685.

[33] Z. He, C. Maldarelli, Z. Dagan. The size of stagnant caps of bulk soluble surfactant on the itnerfaces of translating fluid droplets. *J. Colloid Interface Sci.* **146** (1991) pp. 442-451.

[34] J.A. Holbrook, M.D. LeVan. Retardation of droplet motion by surfactant. Part 1. Theoretical development and asymptotic solutions. *Chem. Eng. Commun.* **20** (1983) pp. 191-207.

[35] J.A. Holbrook, M.D. LeVan. Retardation of droplet motion by surfactant. Part 2. Numerical solutions for exterior diffusion, surface diffusion, and adosprtion kinetics. *Chem. Eng. Commun.* **20** (1983) pp. 273-290.

[36] J. Chen, K.J. Stebe. Marangoni retardation of the terminal velocity of a settling droplet: the role of surfactant phyico-chemistry. *J. Colloid Interface Sci.* **178** (1996) pp. 144-155.

[37] G.M. Ginley, C.J. Radke. Influence of soluble surfactants on the flow of long bubbles through a cylindrical capillary. *ACS Symp. Series* **396** (1989) pp. 480-501.

[38] J. Ratulowski, H.-C. Chang. Marangoni effects of trace impurities on the motion of long gas bubbles in capillaries. *J. Fluid Mech.* **210** (1990) pp. 303-328.

[39] F. Wassmuth, W.G. Laidlaw, D.A. Coombe. Calculation of interfacial flows and surfactant redistribution as a gas/liquid interface moves between two parallel plates. *Phys. Fluids* **5** (1993) pp. 1533-1548.

[40] S.N. Ghadiali, D.P. Gaver III. The influence of non-equilibrium surfactant dynamics on the flow of a semi-infinite bubble in a rigid cylindrical capillary tube. *J. Fluid Mech.* **478** (2003) pp. 165-196.

[41] H. Fujioka, J.B. Grotberg. The steady propogation of a surfactant-laden liquid plug in a two-dimensional channel. *Phys. Fluids* **17** (2005) 082102.

[42] A.H.P. Skelland, S. Woo, G.G. Ramsay. Effects of surface-active agents on drop size, terminal velocity, and droplet oscillation in liquid-liquid systems. *Ind. Eng. Chem. Res.* **26** (1987) pp. 907-911.

[43] K. Malysa, M. Krasowska, M. Krzan. Influence of surface active substances on bubble motion and collision with various interfaces. *Adv. Colloid Interface Sci.* **114-115** (2005) pp. 205-225.

[44] N. Paul, J.M. Schulz, M. Kraume. Fluid dynamics of droplets as a useful tool to determine coverage and adsorption kinetics of surfactants. *Chem. Eng. Tech.* **38** (2015) pp. 1979-1984.

[45] S.-Y. Lin, K. McKeigue, C. Maldarelli. Diffusion-controlled surfactant adsorption studied by pendant drop digitization. *AIChE J.* **36** (1990) pp. 1785-1795.

[46] V.B. Fainerman, S.V. Lylyk, E.V. Aksenenko, A.V. Makievski, J.T. Petkov, J. Yorke, R. Miller. Adsorption layer characteristics of Triton surfactants 1. Surface tension and adsorption isotherms. *Colloids Surf. A* **334** (2009) pp. 1-7.

[47] T. Maxworthy, C. Gnann, M. Kürten, F. Durst. Experiments on the rise of air bubbles in clean viscous liquids. *J. Fluid Mech.* **321** (1996) pp. 421-441.

[48] R. Palaparthi, D.T. Papageorgiou, C. Maldarelli. Theory and experiments on the stagnant cap regime in the motion of spherical surfactant-laden bubbles. *J. Fluid Mech.* **559** (2001) pp. 1-44.

[49] J.A. Nelder, R. Mead. A simplex method for function minimization. *Comput. J.* **7** (1965) pp. 308-313.

[50] T.G. Kolda, R.M. Lewis, V. Torczon. Optimization by direct search: new perspectives on some classical and modern methods. *SIAM Rev.* **(45** (2003) pp. 385-482.

[51] N.J. Alvarez, L.M. Walker, S.L. Anna. A non-gradient based algorithm for the determination of surface tension from a pendant drop: Application to low Bond number drop shapes. *J. Colloid Interface Sci.* **333** (2009) pp. 557-562.

[52] W. Yu. Positive basis and a class of direct search techniques. *Scientia Sinica, Special Issue of Math* **1** (1979) 5367.

[53] V. Torczon. On the convergence of pattern search algorithms. *SIAM J. Optim.* **7** (1997) pp. 1-25.

[54] A. Kalantarian, S.M.I. Saad, A.W. Neumann. Accuracy of surface tension measurement from drop shapes: The role of image analysis. *Adv. Colloid Interface Sci.* **199-200** (2013) pp. 15-22.

[55] N. Otsu. A threshold selection method from gray-level histograms. *IEEE Trans. Syst., Man, Cybern., Syst.* **9** (1979) pp. 62-66.

[56] F. Bashforth, J.C. Adams. *An attempt to test the theories of capillary action.* Cambridge University Press, London, (1883).

[57] W.M. Haynes, T.J. Bruno, D.R. Lide. *CRC Handbook of Chrmistry and Physics, 95th ed.*. CRC Press: Boaca Raton, FL (2015).

[58] B. von Szyszkowski. Experimental studies of the capillary properties of aqueous solutions of fatty acids. *Z. Phys. Chem.* **64** (1908) pp. 385-414.

[59] I. Langmuir. The consitution and fundamental properties of solids and liquids. II. Liquids. *J. Am. Chem. Soc.* **39** (1917) pp. 1848-1905.

[60] C.-H. Change, E.I. Franses. Adsorption dynamics of surfactants at the air/water interface: a critical review of mathematical models, data, and mechanisms. *Colloids Surf. A* **100** (1995) pp. 1-45.

[61] E.H. Lucassen-Reynders. Surface equation of state for ionized surfactants. *J. Phys. Chem.* **70** (1966) pp. 1777-1785.

[62] A.J. Prosser, E.I. Franses. Adsorption and surface tension of ionic surfactants at the air-water interface: review and evaluation of equilibrium models. *Colloids Surf. A* **178** (2001) pp. 1-40.

[63] J. Eastoe, S. Nave, A. Downer, A. Paul, A. Rankin, K. Tribe, J. Penfold. Adsorption of ionic surfactants at the air-solution interface. *Langmuir* **16** (2000) pp. 4511-4518.

[64] C.-T. Hsu, M.-J. Shao, S.-Y. Lin. Adsorption kinetics of $C_{12}E_4$ at the air-water interface: adsorption onto a fresh interface. *Langmuir* **16** (2000) pp. 3187-3194.

[65] C.H. Chang, E.I. Franses. Modified Langmuir-Hinshelwood kinetics for dynamic adsorption of surfactants at the air/water interface. *Colloids Surf.* **69** (1992) pp. 189-201.

[66] K. Lunkenheimer, G. Czichocki, R. Hirte, W. Barzyk. Novel results on the adsorption of ionic surfactants at the air/water interface - sodium-n-alkyl sulphates. *Colloids Surf. A* **101** (1995) pp. 187-197.

[67] A.V. Makievski, G. Loglio, J. Krägel, R. Miller, V.B. Fainerman, A.W. Neumann. Adsorption of protein layers at the water/air interface as studied by axisymmetric drop and bubble shape analysis. *J. Phys. Chem.* **103** (1999) pp. 9557-9561.

[68] K.J. Mysels. Surface tension of solutions of pure sodium dodecyl sulfate. *Langmuir* **2** (1986) pp. 423-428.

[69] P. Warszyński, W. Barzyk, K. Lunkenheimer, H. Fruhner. Surface tension and surface potential of Na *n*-dodecyl sulfate at the air-solution interface: model and experiment. *J. Phys. Chem. B* **102** (1998) pp. 10948-10957.

[70] R. Miller, V.B. Fainerman, A.V. Makievski, M. Leser, M. Michel, E.V. Aksenenko. Determination of protein adsorption by comparative drop and bubble profile analysis tensiometry. *Colloids Surf. B* **36** (2004) pp. 123-126.

[71] V.B. Fainerman, S.V. Lylyk, A.V. Makievski, R. Miller. Interfacial tensiometry as a novel methodology for the determination of surfactant adsorption at a liquid surface. *J. Colloid Interface. Sci.* **275** (2004) pp. 305-308.

[72] V.B. Fainerman, S.A. Zholob, J.T. Petkov, R. Miller. $C_{14}EO_8$ adsorption characteristics studied by drop and bubble profile tensiometry. *Colloids Surf. A* **323** (2008) pp. 56-62.

[73] N.J. Alvarez, L.M. Walker, S.L. Anna. A criterion to assess the impact of confined volumes on surfactant transport to liquid-fluid interfaces. *Soft Matter* **8** (2012) pp. 8917-8925.

[74] V.B. Fainerman, E.V. Aksenenko, J. Krägel, R. Miller. Viscoelasticity moduli of aqueous $C_{12}EO_8$ solutions as studied by drop and bubble profile methods. *Langmuir* **27** (2011) pp. 13975-13977.

[75] S.M.I. Saad, Z. Policova, E.J. Acosta, A.W. Neumann. Range of validity of drop shape techniques for surface tension measurement. *Langmuir* **26** (2010) pp. 14004-14013.

[76] S.-Y. Lin, K. McKeigue, C. Maldarelli. Effect of cohesive energies between adsorbed molecules on surfactant exchange processes: Shifting from diffusion control for adsorption to kinetic-diffusive control for re-equilibrium. *Langmuir* **10** (1994) pp. 3442-3448.

[77] S.-H. Lin, T.-L. Lu, W.-B. Hwang. Adsorption kinetics of decanol at the air-water interface. *Langmuir* **11** (1995) pp. 555-562.

[78] S.-Y. Lin, R.-Y. Tsay, L.-W. Lin, S.-I. Chen. Adsorption kinetics of $C_{12}E_8$ at the air-water interface: adsorption onto a clean interface. *Langmuir* **12** (1996) pp. 6530-6536.

[79] R. Pan, J. Green, C. Maldarelli. Theory and experiment on the measurement of kinetic rate constants for surfactant exchange at an air/water interface. *J. Colloid Interface Sci.* **205** (1998) pp. 213-230.

[80] N.J. Alvarez, L.M. Walker, S.L. Anna. Diffusion-limited adsorption to a spherical geometry: the impact of curvature and competitive time scales. *Phys. Rev. E* **82** (2010) 011604.

[81] D.R. Unger, F.J. Muzzio, J.G. Aunins, R. Singhvi. Computation and experimental investigation of flow and fluid mixing in the roller bottle bioreactor. *Biotechnol. Bioeng.* **70** (2000) pp. 117-130.

[82] A. Oron, S.H. Davis, S.G. Banknoff. Long-scale evolutino of thin liquid films. *Rev. Mod. Phys.* **69** (1997) pp. 931-980.

[83] R.S. Laugesen, M.C. Pugh. Properties of steady states for thin film equations. *Euro. J. Apply. Math.* **11** (2000) pp. 293-351.

[84] M. Heil. Finite Reynolds number effects in the Bretherton problem. *Phys. Fluids* **13** (2001) pp. 2517-2521.

[85] R.V. Craster, O.K. Matar. Dynamics and stability of thin liquid films. *Rev. Mod. Phys.* **81** (2009) pp. 1131-1198.

[86] E. Klaseboer, R. Gupta, R. Manica. An extended Bretherton model for long Taylor bubbles at moderate capillary numbers. *Phys. Fluids* **26** (2014) 032107.

[87] H.A. Stone. A simple derivation of the time-dependent convective-diffusion equation for surfactant transport along a deforming interface. *Phys. Fluids A* **2** (1990) pp. 111-112.

[88] O.E. Jensen, J.B. Grotberg. Insoluble surfactant spreading on a thin viscous film: shock evolution and film rupture. *J. Fluid Mech.* **240** (1992) pp. 259-288.

[89] W.J. Milliken, L.G. Leal. The influence of surfactant on the deformation and breakup of a viscous drop: The effect of surfactant solubility. *J. Colloid Interface Sci.* **166** (1994) pp. 275-285.

[90] D. Halpern, Y.-C. Li, H.-H. Wei. Slip-induced suppresion of Marangoni film thickening in surfactant-retarded Landau-Levich-Bretherton flows. *J. Fluid Mech.* **781** (2015) pp. 578-594.

[91] H.A. Stone, L.G. Leal. The effects of surfactants on drop deformation and breakup. *J. Fluid Mech.* **210** (1990) pp. 161-186.

[92] R.A. Johnson, A. Borhan. Effects of insoluble surfactants on the pressure-driven motion of a drop in a tube in the limit of high surface coverage. *J. Colloid Interface Sci.* **218** (1999) pp. 184-200.

[93] P.M. Vlahovska, M. Loewenberg, J. Blawzdziewicz. Deformation of a surfactant-covered drop in a linear flow. *Phys. Fluids* **17** (2005) 103103.

[94] T. Ward, M. Faivre, H.A. Stone. Drop production and tip-streaming phenomenon in a microfluidic flow-focusing device via an interfacial chemical reaction. *Langmuir* **26** (2010) pp. 9233-9239.

[95] A. Provenzale. Transport by coherent barotropic vortices. *Annu. Rev. Fluid Mech.* **31** (1999) pp. 55-93.

[96] A. Borhan, J. Pallinti. Breakup of drops and bubbles translating through cylindrical capillaries. *Phys. Fluids* **11** (1999) pp. 2846-2855.

[97] J.H. Snoeijer, N. Le Grand-Piteira, L. Limat, H.A. Stone, J. Eggers. Cornered drops and rivulets. *Phys. Fluids* **19** (2007) 042104.

[98] J.H. Ferziger. *Numerical Methods for Engineering Application, 2nd Ed.*. Wiley: New York City, NY (1998).

[99] M.D. LeVan, J. Newman. The effect of surfactant on the terminal and interfacial velocities of a bubble or drop. *AIChE J.* **22** (1976) pp. 695-701.

[100] S.S. Sadhal, R.E. Johnson. Stokes flow past bubbles and drops partially coated with thin films. Part 1. Stagnant cap of surfactant film - exact solution. *J. Fluid Mech.* **126** (1983) pp. 237-250.

[101] H.A. Stone, L.G. Leal. The effects of surfactants on drop deformation and breakup. *J. Fluid Mech.* **220** (1990) pp. 161-186.

[102] A. Borhan, C.F. Mao. Effect of surfactants on the motion of drops through circular tubes. *Phys. Fluids A* **4** (1992) pp. 2628-2640.

[103] X. Li, C. Pozrikidis. The effect of surfactants on drop deformation and on the rheology of dilute emulsions in Stokes flow. *J. Fluid Mech.* **341** (1997) pp. 165-194.

[104] M.A. Rother, R.H. Davis. Buoyancy-driven breakup of an isolated drop with surfactant. *Phys. Rev. Letters* **101** (2008) 044501.

[105] M.A. Rother. The effect of surfactant redistribution on combined gravitational and thermocapillary interactions of deformable drops. *Acta Astron.* **91** (2013) pp. 55-68.

[106] R.A. Johnson, A. Borhan. Stability of the shape of a surfactant-laden drop translating at low Reynolds number. *Phys. Fluids* **12** (2000) pp. 773-784.

[107] C. Pozrikdis. *A Practical Guide to Boundary Element Methods with the Software Library BEMLIB*. CRC Press: Boca Raton, FL (2002).

[108] J. Happel, H. Brenner. *Low Reynolds Number Hydrodynamics*. Springer: New York City, NY (1963).

[109] C. Pozrikidis. The instability of a moving viscous drop. *J. Fluid Mech.* **210** (1990) pp. 1-21.

[110] R.P. Chhabra, J. Bangun. Wall effects on terminal velocity of small drops in Newtonian and non-Newtonian fluids. *Can. J. Chem. Eng.* **75** (1997) pp. 817-822.

[111] Y. Wang, D.T. Papageorgiou, C. Maldaralli. Increased mobility of a surfactant-retarded bubble at high bulk concentrations. *J. Fluid Mech.* **390** (1999) pp.251-270.

[112] M.A. Rother, A.Z. Zinchenko, R.H. Davis. Surfactant effects on buoyancy-driven viscous interactions of deformable drops. *Colloids Surf. A* **282-283** (2006) pp. 50-60.

[113] C. Pozrikdis. Interfacial dynamics for Stokes flow. *J. Comput. Phys.* **169** (2001) pp. 250-301.

[114] Haplotyping germine and cancer genomes with high-throughput lined-read sequencing. *Nature Biotechnol.* **34** (2016) pp. 303-311.

[115] I.S. Gradshteyn, I.M. Ryzhik. *Table of Integrals, Series and Products*. Academic Press: San Diego, CA (1980).

ACKNOWLEDGEMENTS

I would like to express my sincerest gratitude to my adviser Dr. Thomas Ward for many years of guidance, encouragement and mentorship dating back to my first undergraduate research projects. I have been very fortunate to have him as a mentor. I would like to thank my program of study committee Dr. Hui Hu, Dr. James Michael, Dr. Jonathan Regele and Dr. Richard Wlezien for their assistance and helpful discussions in completing this thesis. I would also like to thank undergraduate researchers Hyaquino Hyacinthe, Azeez Odesanya and Caroline Pereira for the assistance they have provided me in the lab over the years. Finally if it were not for my loving family and countless friends this would never have been possible.

The work appearing in this thesis was partially supported by NSF grant no. CBET-1262718 and NSF grant no. HRD-1102461.